

**LASER SYSTEM FOR PRECISION SPECTROSCOPY OF THE GROUND
STATE HYPERFINE SPLITTING IN MUONIC HYDROGEN**

Dissertation submitted
for the award of the title
"Doctor of Natural Sciences"
to the Faculty of Physics, Mathematics, and Computer Science
of Johannes Gutenberg University Mainz
by

Siddharth Rajamohan

JOHANNES GUTENBERG
UNIVERSITÄT MAINZ



Johannes Gutenberg-Universität Mainz
Deutschland

1st Examiner: Prof. Dr. Randolph Pohl
2nd Examiner: Prof. Dr. Aldo Sady Antognini
3rd Examiner: Prof. Dr. Marc Vanderhaeghen
4th Examiner: Prof. Dr. Niklaus Berger

Supervisor : Prof. Dr. Randolph Pohl
Date of doctoral examination : 16.07.2025

CONTENTS

1	Introduction	9
1.1	Hyperfine structure in hydrogen	9
1.2	Muonic Atom Spectroscopy	9
1.3	The hyperfine splitting in muonic hydrogen	11
1.4	HyperMu Experiment	14
2	HyperMu Laser System Design	19
2.1	Laser Physics and Pulse Generation	19
2.2	Nonlinear Optics	22
2.2.1	Linear response - Refractive index and birefringence	23
2.2.2	Three-wave mixing	24
2.2.3	Phase matching	29
2.3	General Layout	33
2.3.1	Two-step DFG stage and choice of wavelengths	34
2.3.2	1030 nm Thin Disk Oscillator-Amplifier	39
2.3.3	3.1 μm -MOPA branch	41
2.3.4	Control system for spectroscopy and frequency calibration	43
2.4	Conclusion	44
3	2.1 μm-Variable Finesse Optical Parametric Oscillator	47
3.1	Technical Implementation	47
3.2	Variable finesse singly-resonant cavity design	49
3.2.1	Injection-seeding and cavity layout	49
3.2.2	Variable-finesse cavity	51
3.2.3	Jones matrices	52
3.2.4	Intracavity spectral profile and finesse	55
3.2.5	Pound-Drever-Hall stabilization	59
3.3	Characterization of the OPO	62
3.3.1	Characterization scheme	62
3.4	Conclusion	68
4	Optical Parametric Amplifier	69
4.0.1	Technical Implementation	69
4.0.2	Characterization	70
4.0.3	Preliminary tests with thin-disk amplifier	74
4.1	Conclusion	75
5	ZGP-mediated Difference Frequency Generation	79
5.0.1	Phase matching in ZGP	79
5.1	Technical Implementation	80

5.2	Characterization	81
5.2.1	Phase matching bandwidth	81
5.2.2	Energy characterization and conversion efficiency	83
5.2.3	Spatial and temporal profile characterization	86
5.3	Conclusion	90
6	Frequency calibration and Laser bandwidth	93
6.1	Frequency calibration using known molecular transitions in Mid-infrared regime	95
6.1.1	Molecular spectrum in the MIR	95
6.2	Absorption spectroscopy of H ₂ O	97
6.2.1	Preliminary measurement on atmospheric H ₂ O	97
6.2.2	Absorption spectroscopy in a H ₂ O-vapor cell	99
6.2.3	Analysis	102
6.2.4	Conclusion on the laser bandwidth	105
A	Line-broadening effects	111

LIST OF FIGURES

1.1	Probability density when the lepton is in the ground state of the lepton-proton bound system	10
1.2	Energy level diagram of 1S HFS in μH	11
1.3	Feynman diagrams of elastic and inelastic two-photon exchange contribution	12
1.4	Literature values for the polarizability correction in μH Δ_{pol} and Zemach radius of the proton	13
1.5	Principle of HyperMu experiment	15
2.1	Spatial profile of an ideal Gaussian beam	20
2.2	Temporal and spectral profile of an ideal Gaussian beam	20
2.3	Illustration of birefringence for direction of propagation (a) along the optic axis (b) normal to the optic axis	24
2.4	Possible three-wave mixing in nonlinear materials with non-vanishing second-order susceptibility	25
2.5	Relative variation in the intensities of the pump (blue), signal (green) and idler(red) fields for different ratios of incident signal to pump intensities	27
2.6	Illustration of the walk-off effect due to optical anisotropy	31
2.7	Illustration of the arrangement of ferroelectric domains in a periodically-poled crystal	32
2.8	Layout of laser system for HyperMu experiment	34
2.9	Absorption spectrum of a ZGP crystal of length 1 cm	36
2.10	SNLO simulations variation of output energy of 6.8 μm pulses with the input energy of 2.1 μm pulses.	37
2.11	Optical and electronic layout of the thin-disk oscillator	40
2.12	Optical and electronic layout of the 3.1 μm -MOPA.	42
2.13	Frequency control and monitoring system of laser system for spectroscopy	43
3.1	Optical and electronic layout of the singly resonant injection-seeded PDH-locked OPO Cavity	48
3.2	Simulation of variation of beam waist of injected CW-1978nm along the cavity axis	49
3.3	Comparison between a (a)doubly-resonant OPO (b)singly-resonant OPO (c) singly-resonant OPO with injection seeding at ω_s^{inj}	50
3.4	Intracavity Polarization variation in the OPO cavity	52
3.5	Variation of the cavity finesse with the angle of the QWP	57
3.6	Trace of Cavity transmission and the PDH-error signal in the oscilloscope	58
3.7	Intracavity profile and error signal of PDH locking for different modulation parameters	61
3.8	Scheme used for energy and beam quality characterization of the output of the OPO	63

3.9	Variation of conversion efficiency of the OPO with the temperature of the crystal	64
3.10	Output energy of signal photons produced in OPO as a function of input pump photon energy for different cavity finesse	65
3.11	Average output energy of 2.1 μm pulses and the RMS of 100 pulses for conditions of Pound-Drever-Hall locking and Injection Seeding	66
3.12	Beam quality characterization of OPO Output	67
4.1	Optical layout of the 2.1 μm -OPA	70
4.2	Variation of conversion efficiency of the 2.1 μm -OPA with temperature of the crystal	71
4.3	Energy of the amplified 2.1 μm pulses vs Input 1030 nm pulse energy . . .	72
4.4	Output vs seed	73
4.5	Beam quality characterization of OPA Output	74
4.6	Variation of output energy of 2.1 μm pulses with input energy of 1030 nm pulses from the TDA.	76
5.1	Idler and signal wavelength as a function of the phase matching angle simulated with SNLO for fixed pump wavelength of $\lambda_p = 2149 \text{ nm}$ for Type I and Type II phase matching in ZGP	80
5.2	Optical layout for DFG scheme where 2.1 μm and 3.1 μm generate 6.8 μm pulses	81
5.3	Variation of the normalized conversion efficiency of the 6.8 μm -DFG stage with respect to the crystal orientation for various wavelengths	82
5.4	Measured optimum phase matching angle versus wavelength	83
5.5	Normalized conversion efficiency of the 6.8 μm -DFG stage with respect to the crystal orientation for two crystal temperatures	84
5.6	Optimal orientation of the ZGP crystal for phase matching at different temperatures	84
5.7	Variation of the energy of generated 6.8 μm pulses with respect to energy of 2.1 μm pump pulses	85
5.8	dfg output vs seed	86
5.9	Conversion efficiency of the 6.8 μm -DFG stage versus the energy of 2.1 μm pump pulses for two input signal energy at 3.1 μm wavelength	87
5.10	M^2 measurement of the 6.8 μm beam from the 6.8 μm -DFG stage	88
5.11	Spatial profile of the DFG pulse	88
5.12	Pointing stability measurement of the 6.8 μm pulses	89
5.13	Waveform of all pulses	90
5.14	Pulse duration at different stages of Laser system	91
6.1	Schematic of frequency calibration methods	94
6.2	Absorption spectra of reference gases listed in HITRAN	96
6.3	Transmission of ν_{67xx} -photons by H_2O molecules in the path of propagation of length 1 m in the optical table	98
6.4	Layout of the scheme used for spectroscopy of H_2O	101
6.5	Measured energy for spectroscopy of H_2O	103
6.6	Sample absorption spectrum of H_2O	104
6.7	Measured absorption profile of H_2O molecules for the 6.8 μm pulses at various pressures for the same transition frequency	106
6.8	Resonance frequencies determined from fit for transitions in H_2O	107

6.9	FWHM determined from fit for transitions in H ₂ O	108
6.10	Fourier transform of the measured temporal profile of the 6.8 μm pulse.	109
6.11	Comparison of FWHM from fit, Doppler-broadening and laser spectrum .	110

ACKNOWLEDGMENTS

First and foremost, I would like to express my deepest gratitude to all those who have supported and inspired me throughout this journey.

Thank you, Randolph, for giving me the opportunity to undertake this doctoral project and to be part of the HyperMu collaboration. Thank you, Aldo, for your unwavering commitment to your students. I am especially grateful to both of you for your invaluable guidance, patience, and support throughout these years.

Special thanks to Lukas Affolter, Muharreem, Ahmed, Elmer, Oguzhan, Karsten, Weiling, Mirek, Pauline Yzombard, François Nez and Manuel – your insights, collaboration, and support have been invaluable. It has been a pleasure working with you guys on the experiment!

I would also like to thank Katharina, Asia, Patrick, Jonas Nuber, Giovanni, Giuseppe, Aziza, Lukas Gerritzen, Miguel, Andrej Marraffio, and Ivan – each of you contributed to this work in your own unique way, and I am sincerely grateful for your friendship and presence. I am especially thankful to Elmer, Asia, Katharina, and Giuseppe for your criticism, encouragement and motivation during the writing and final stages of my thesis.

To Anita and Steffi Wortmann, thank you for your consistent support and for helping me navigate the maze of logistics and endless paperwork.

Thanks to the entire Mainz/AG Pohl team – Franziska Hagelstein, Frederik Wauters, Marcel Willig, Gregor, Hendrik, Merten, and Hannah – for your support and collaboration.

Finally, to my wife Anagha, my family, and my friends – your love, patience, and unwavering belief in me have been my foundation throughout this journey. I could not have done this without you.

ABSTRACT

This thesis describes the laser system for the spectroscopy of the 1S HFS ($1S_{1/2}^{F=1}-1S_{1/2}^{F=0}$) in muonic hydrogen (μH), pursued by the CREMA collaboration with its current experiment *HyperMu*.

Muonic hydrogen is an atomic system formed by a muon (μ^-), a negatively charged unstable lepton with a lifetime of $\sim 2.2 \mu\text{s}$, and a proton (p), much like the hydrogen atom ($e\text{H}$). As the muon is ~ 207 times more massive than the electron, the wavefunction of the muon has a larger overlap with that of the nucleus, making its bound-state energy levels characteristically perturbed by nuclear structure effects. A measurement of the 1S HFS to about 1 ppm in μH allows the determination of the nuclear structure contribution to about 200 ppm. In a second step from this contribution, the Zemach radius and the polarizability contribution can be deduced, assuming polarizability from theory or the Zemach radius from ep scattering of $e\text{H}$.

The experiment is to be conducted at the Paul Scherrer Institute (PSI), Switzerland, where a high-intensity continuous muon beam is available. The muons from the $\Pi\text{E}5$ beamline are stopped within a H_2 target (22 K temperature, 0.5 bar pressure) to form μH . After thermalization, these atoms are excited by the laser pulses that undergo multiple reflections in a toroidal enhancement cell, placed in the H_2 target, to increase the $1S_{1/2}^{F=0}-1S_{1/2}^{F=1}$ transition probability. The lifetime of the $1S_{1/2}^{F=1}$ state is longer than that of the muons, which makes the fluorescence from the deexcitation not a viable indicator of laser excitation. An indirect detection scheme is designed based on diffusion of μH through the H_2 and the production of X-rays at its arrival at the target walls. The laser-excited μH undergoing a collision with H_2 molecules acquires a kinetic energy of 0.1 eV and diffuses efficiently to the target walls coated with gold. The transfer of μ^- from the μH to the Au atom creates μAu in an excited state. The deexcitation of μAu generates characteristic X-rays that are detected by X-ray detectors to indicate laser excitation. The resonance curve of the HFS transition is obtained by plotting the number of μAu events versus the frequency of the laser.

Simulations indicate that the laser pulses for the spectroscopy must have an energy of 3 mJ with 100 MHz frequency bandwidth at the predicted transition wavelength of $6.8 \mu\text{m}$. Moreover, as the muons arrive stochastically within the target, the laser system must be stochastically triggerable with an average repetition rate of $>100 \text{s}^{-1}$. The muon lifetime constrains the maximum pulse build-up time to be $\sim 1 \mu\text{s}$. Generating such high-energy pulses in the mid-infrared in such a short time and with adequate frequency control is technologically challenging. We pursue a two-stage design that begins with the generation of NIR 1030 nm pulses, followed by a second stage that downconverts the 1030 nm pulses into the required $6.8 \mu\text{m}$ pulses via nonlinear difference frequency generation (DFG).

Pulses of 1030 nm of 50 ns duration and energy 30 mJ are generated in a thin-disk oscillator by the method of cavity dumping within $<1 \mu\text{s}$. These pulses are amplified to the energy of 300 mJ by a thin-disk multipass amplifier (TDA). These 1030 nm pulses are used for pumping two optical parametric oscillators (OPO) operating at 2.1 μm and 3.1 μm wavelengths. The 2.1 μm -OPO converts the 1030 nm pulse into pulses of wavelength 2.1 μm and 1.9 μm while the 3.1 μm -OPO converts the 1030 nm pulse into pulses of wavelength 3.1 μm and 1.5 μm . In a similar process, the 2.1 μm and 3.1 μm pulses

are amplified by 1030 nm pulses to energies of 25 mJ and 3 mJ, respectively, in their respective optical parametric amplifiers. The 6.8 μm pulses are eventually obtained by difference frequency generation of the 2.1 μm pulse and the 3.1 μm pulse. The TDO and the two OPOs are injection-seeded and Pound-Drever-Hall (PDH) stabilized to ensure single-frequency operation. While the wavelength of the 1030 nm and 2.1 μm pulses are fixed, the wavelength of the 3.1 μm pulses can be varied by changing the frequency of the seed-laser. This allows the 6.8 μm pulses to be scanned across the search range of 6798 nm - 6785 nm of the 1S HFS in μH .

This thesis deals with the development of the 2.1 μm -OPO, the 2.1 μm -OPA, the 6.8 μm -DFG stage and the frequency calibration of the 6.8 μm pulses.

Chapter 1 of the thesis elaborates on the motivation of the experiment along with a summary of the theoretical efforts parallel to the experiment. Details of the experimental scheme are given, focusing on the aspects that constrain the requirements of the laser system.

Chapter 2 of the thesis discusses the layout of the laser system under development, designed to satisfy these requirements. A brief review of laser physics and nonlinear optics, as well as the current status of the laser system, is provided.

Chapter 3 compiles the results on the 2.1 μm -OPO and the implications on its variable-finesse cavity layout. The effect of injection-seeding and PDH stabilization of the cavity on the energy and stability is studied. Generation of 2.1 μm pulses of energy 1 mJ of average beam quality $M^2 \sim 1.12$ with 5 mJ of input 1030 nm pulse energy is demonstrated.

Chapter 4 describes the amplification of the 2.1 μm pulses of 1 mJ energy by the 2.1 μm -OPA to ~ 5 mJ while providing a beam with average M^2 of 1.56, for input 1030 nm pulse energy of 25 mJ from the TDO. Preliminary tests of the 2.1 μm -OPA with 1030 nm pulses of energy 95 mJ are shown to amplify the 2.1 μm pulses to 22 mJ.

Chapter 5 focuses on the 6.8 μm -DFG stage that converts the 2.1 μm pulses into 6.8 μm pulses. 300 μJ of 6.8 μm is generated from 6 mJ of 2.1 μm and 300 μJ of 3.1 μm -seed pulses. The dependence of the nonlinear process on the orientation and temperature of the crystal, as well as the frequency of the 6.8 μm beam, is studied for optimum frequency and energy control during the μH spectroscopy campaign.

Chapter 6 reports on the frequency calibration of the 6.8 μm pulses. By absorption spectroscopy in a H_2O vapour cell, three resonances of H_2O are studied for various pressures between the range 0.1 mbar and 7 mbar. From a fit to the measured transition, the centroid position and linewidth of the transitions are obtained. The obtained centroid positions were all systematically deviating by 50 MHz from the HITRAN value, indicating the need to recheck the frequency calibration. From the linewidth, the upper limit of the laser bandwidth was determined to be 110 MHz. This fulfils the minimum requirement for the spectroscopy in μH .

In this thesis, we have demonstrated for the first time our ability to produce 6.8 μm pulses with the necessary frequency control. Energy scaling of the laser system will be needed to reach 3 mJ energy at the 6.8 μm wavelength, but the observed efficiency is promising.

ZUSAMMENFASSUNG

Muonischer Wasserstoff ist ein atomares System, das aus einem Myon (μ^-), einem negativ geladenen instabilen Lepton mit einer Lebensdauer von $\sim 2.2 \mu\text{s}$, und einem Proton (p) besteht, ähnlich wie das Wasserstoffatom (eH). Da das Myon etwa 207-mal schwerer ist als das Elektron, hat dessen Wellenfunktion einen grösseren Überlapp mit dem Atomkern, wodurch seine Energiezustände im gebundenen Zustand auf charakteristische Weise durch die Kernstruktur beeinflusst werden. Eine Messung der 1S-HFS auf etwa 1 ppm in μH ermöglicht die Bestimmung des Beitrags der Kernstruktur auf etwa 200 ppm. In einem zweiten Schritt lassen sich aus diesem Beitrag der Zemach-Radius und der Beitrag der Polarisierbarkeit ableiten, wobei die Polarisierbarkeit aus der Theorie und der Zemach-Radius aus der ep-Streuung von eH angenommen werden.

Das Experiment soll am Paul Scherrer Institut (PSI) in der Schweiz durchgeführt werden, wo ein hochintensiver kontinuierlicher Myonenstrahl zur Verfügung steht. Die Myonen aus der PE5-Strahllinie werden in einem H_2 -Target (22 K Temperatur, 0.5 bar Druck) gestoppt, um μH zu bilden. Nach der Thermalisierung werden diese Atome durch Laserimpulse angeregt, welche in einem toroidalen Resonator, der sich im H_2 -Target befindet, mehrfach reflektiert werden, um die $1S_{1/2}^{F=0} - 1S_{1/2}^{F=1}$ -Übergangswahrscheinlichkeit zu erhöhen. Die Lebensdauer des $1S_{1/2}^{F=1}$ -Zustands ist länger als die der Myonen, wodurch die Fluoreszenz aus der Abregung kein brauchbarer Indikator für die Laserexcitation ist. Ein indirektes Detektionsschema basiert auf der Diffusion von μH durch das H_2 und der Erzeugung von Röntgenstrahlen bei seiner Ankunft an den Kammerwänden. Das angeregte μH , das mit H_2 -Molekülen kollidiert, erhält eine kinetische Energie von 0.1 eV und diffundiert effizient zu den mit Gold beschichteten Zielwänden. Die Übertragung von μ^- vom μH zum Au-Atom erzeugt μAu in einem angeregten Zustand. Die Entregung von μAu erzeugt charakteristische Röntgenstrahlen, die von Röntgendetektoren erfasst werden, um die Laseranregung anzuzeigen. Die Resonanzkurve des HFS-Übergangs wird durch Auftragen der Anzahl der μAu -Ereignisse gegen die Frequenz des Lasers erhalten.

Simulationen zeigen, dass die Laserimpulse für die Spektroskopie eine Energie von 3 mJ mit einer Frequenzbandbreite von 100 MHz bei der vorhergesagten Übergangswellenlänge von $6.8 \mu\text{m}$ haben müssen. Da die Myonen stochastisch im Ziel ankommen, muss das Lasersystem außerdem stochastisch auslösbar sein, mit einer durchschnittlichen Wiederholungsrate von $>100 \text{s}^{-1}$. Die Lebensdauer der Myonen begrenzt die maximale Impulsaufbauzeit auf $\sim 1 \mu\text{s}$. Die Erzeugung solcher hochenergetischer Impulse im mittleren Infrarotbereich in so kurzer Zeit und mit ausreichender Frequenzsteuerung ist technologisch anspruchsvoll. Wir verfolgen ein zweistufiges Design, das mit der Erzeugung von NIR- 1030 nm-Impulsen beginnt, gefolgt von einer zweiten Stufe, in der die 1030 nm-Impulse durch nichtlineare Differenzfrequenzerzeugung (DFG) in die erforderlichen $6.8 \mu\text{m}$ -Impulse herunterkonvertiert werden.

Impulse von 1030 nm mit einer Dauer von 50 ns und einer Energie von 30 mJ werden in einem Dünnscheibenoszillator durch die Methode des Cavity Dumping innerhalb von $<1 \mu\text{s}$ erzeugt. Diese Impulse werden durch einen DünnscheibenMehrfachdurchlaufverstärker (TDA) auf eine Energie von 300 mJ verstärkt. Diese 1030 nm-Impulse werden zum Pumpen von zwei optischen parametrischen Oszillatoren (OPO) verwendet, die bei den Wellenlängen $2.1 \mu\text{m}$ und $3.1 \mu\text{m}$ arbeiten. Der $2.1 \mu\text{m}$ -OPO wandelt den 1030 nm-Impuls in Impulse der Wellenlänge $2.1 \mu\text{m}$ und $1.9 \mu\text{m}$ um, während der $3.1 \mu\text{m}$ -OPO den 1030 nm-Impuls in Impulse der Wellenlänge $3.1 \mu\text{m}$ und $1.5 \mu\text{m}$ umwandelt. In einem ähnlichen Prozess werden die $2.1 \mu\text{m}$ - und $3.1 \mu\text{m}$ -Impulse durch 1030 nm-Impulse

in ihren jeweiligen optischen parametrischen Verstärkern auf Energien von 25 mJ bzw. 3 mJ verstärkt. Die 6.8 μm -Impulse werden schließlich durch Differenzfrequenzerzeugung des 2.1 μm -Impulses und des 3.1 μm -Impulses erhalten. Der TDO und die beiden OPOs werden injiziert und mit einem Pound-Drever-Hall-Stabilisator (PDH) stabilisiert, um einen Einfrequenzbetrieb zu gewährleisten. Während die Wellenlänge der 1030 nm- und 2.1 μm -Impulse fest ist, kann die Wellenlänge der 3.1 μm -Impulse durch Änderung der Frequenz des Seed-Lasers variiert werden. Dadurch können die 6.8 μm -Impulse über den Suchbereich von 6798 nm - 6785 nm des 1S HFS in μH gescannt werden.

Diese Arbeit befasst sich mit der Entwicklung des 2.1 μm -OPO, des 2.1 μm -OPA, des 6.8 μm -DFG stage und der Frequenzkalibrierung der 6.8 μm -Impulse.

Kapitel 1 der Arbeit erläutert die Motivation für das Experiment und gibt einen Überblick über die theoretischen Arbeiten, die parallel zum Experiment durchgeführt wurden. Es werden Details des Versuchsaufbaus beschrieben, wobei der Schwerpunkt auf den Aspekten liegt, die die Anforderungen an das Lasersystem einschränken.

Kapitel 2 der Arbeit behandelt den Aufbau des in Entwicklung befindlichen Lasersystems, das diese Anforderungen erfüllen soll. Es wird ein kurzer Überblick über die Laserphysik und die nichtlineare Optik sowie über den aktuellen Stand des Lasersystems gegeben.

Kapitel 3 fasst die Ergebnisse zum 2.1 μm -OPO und die Auswirkungen auf dessen variablen Finesse-Hohlraumlayout zusammen. Die Auswirkungen der Injektions-Seeding- und PDH-Stabilisierung des Hohlraums auf die Energie und Stabilität werden untersucht. Die Erzeugung von 2.1 μm -Impulsen mit einer Energie von 1 mJ und einer durchschnittlichen Strahlqualität von $M^2 \sim 1,12$ bei einer Eingangsimpulsenergie von 5 mJ wird demonstriert.

Kapitel 4 beschreibt die Verstärkung der 2.1 μm -Impulse mit einer Energie von 1 mJ durch den 2.1 μm -OPA auf ~ 5 mJ, wobei ein Strahl mit einem durchschnittlichen M^2 von 1,56 bei einer Eingangsimpulsenergie von 25 mJ aus dem TDO bereitgestellt wird. Vorläufige Tests des 2.1 μm -OPA mit 1030 nm-Impulsen mit einer Energie von 95 mJ zeigen, dass die 2.1 μm -Impulse auf 22 mJ verstärkt werden.

Kapitel 5 konzentriert sich auf die 6.8 μm -DFG stage, die die 2.1 μm -Impulse in 6.8 μm -Impulse umwandelt. Aus 6 mJ 2.1 μm und 300 μJ 3.1 μm -Seed-Impulsen werden 300 μJ 6.8 μm erzeugt. Die Abhängigkeit des nichtlinearen Prozesses von der Ausrichtung und Temperatur des Kristalls sowie von der Frequenz des 6.8 μm -Strahls wird untersucht, um eine optimale Frequenz- und Energiekontrolle während der μH -Spektroskopie-Kampagne zu erreichen.

Kapitel 6 berichtet über die Frequenzkalibrierung der 6.8 μm -Impulse. mittels Absorptionsspektroskopie in einer Wasserdampfzelle werden drei Resonanzen von H_2O für verschiedene Drücke im Bereich von 0.1 mbar bis 7 mbar untersucht. Aus den gemessenen Resonanzkurven werden Resonanzfrequenzen und Breiten der gemessenen Übergänge ermittelt. Die erhaltenen Resonanzfrequenzen wichen alle systematisch um 50 MHz vom HITRAN-Wert ab, was darauf hindeutet, dass die Frequenzkalibrierung überprüft werden muss. Aus der Linienbreite wurde die Obergrenze der Laserbandbreite mit 110 MHz bestimmt. Dies erfüllt die Mindestanforderung für die Spektroskopie in μH .

In dieser Arbeit haben wir erstmals unsere Fähigkeit unter Beweis gestellt, 6.8 μm -Impulse mit der erforderlichen Frequenzsteuerung zu erzeugen. Um eine Energie von 3 mJ bei der 6.8 μm -Wellenlänge zu erreichen, ist eine Energieskalierung des Lasersystems erforderlich, aber die beobachtete Effizienz ist vielversprechend.

Muonischer Wasserstoff ist ein atomares System, das aus einem Myon (μ^-), einem negativ geladenen instabilen Lepton mit einer Lebensdauer von $\sim 2.2 \mu\text{s}$, und einem Proton (p) besteht, ähnlich wie das Wasserstoffatom (eH). Da das Myon etwa 207-mal schwerer ist als das Elektron, hat dessen Wellenfunktion einen grösseren Überlapp mit dem Atomkern, wodurch seine Energiezustände im gebundenen Zustand auf charakteristische Weise durch die Kernstruktur beeinflusst werden. Eine Messung der 1S-HFS auf etwa 1 ppm in μH ermöglicht die Bestimmung des Beitrags der Kernstruktur auf etwa 200 ppm. In einem zweiten Schritt lassen sich aus diesem Beitrag der Zemach-Radius und der Beitrag der Polarisierbarkeit ableiten, wobei die Polarisierbarkeit aus der Theorie und der Zemach-Radius aus der $e\text{p}$ -Streuung von eH angenommen werden.

Das Experiment soll am Paul Scherrer Institut (PSI) in der Schweiz durchgeführt werden, wo ein hochintensiver kontinuierlicher Myonenstrahl zur Verfügung steht. Die Myonen aus der PE5-Strahllinie werden in einem H_2 -Target (22 K Temperatur, 0.5 bar Druck) gestoppt, um μH zu bilden. Nach der Thermalisierung werden diese Atome durch Laserimpulse angeregt, welche in einem toroidalen Resonator, der sich im H_2 -Target befindet, mehrfach reflektiert werden, um die $1\text{S}_{1/2}^{F=0} - 1\text{S}_{1/2}^{F=1}$ -Übergangswahrscheinlichkeit zu erhöhen. Die Lebensdauer des $1\text{S}_{1/2}^{F=1}$ -Zustands ist länger als die der Myonen, wodurch die Fluoreszenz aus der Abregung kein brauchbarer Indikator für die Laserexcitation ist. Ein indirektes Detektionsschema basiert auf der Diffusion von μH durch das H_2 und der Erzeugung von Röntgenstrahlen bei seiner Ankunft an den Kammerwänden. Das angeregte μH , das mit H_2 -Molekülen kollidiert, erhält eine kinetische Energie von 0.1 eV und diffundiert effizient zu den mit Gold beschichteten Zielwänden. Die Übertragung von μ^- vom μH zum Au-Atom erzeugt μAu in einem angeregten Zustand. Die Entregung von μAu erzeugt charakteristische Röntgenstrahlen, die von Röntgendetektoren erfasst werden, um die Laseranregung anzuzeigen. Die Resonanzkurve des HFS-Übergangs wird durch Auftragen der Anzahl der μAu -Ereignisse gegen die Frequenz des Lasers erhalten.

Simulationen zeigen, dass die Laserimpulse für die Spektroskopie eine Energie von 3 mJ mit einer Frequenzbandbreite von 100 MHz bei der vorhergesagten Übergangswellenlänge von $6.8 \mu\text{m}$ haben müssen. Da die Myonen stochastisch im Ziel ankommen, muss das Lasersystem außerdem stochastisch auslösbar sein, mit einer durchschnittlichen Wiederholungsrate von $>100 \text{s}^{-1}$. Die Lebensdauer der Myonen begrenzt die maximale Impulsaufbauzeit auf $\sim 1 \mu\text{s}$. Die Erzeugung solcher hochenergetischer Impulse im mittleren Infrarotbereich in so kurzer Zeit und mit ausreichender Frequenzsteuerung ist technologisch anspruchsvoll. Wir verfolgen ein zweistufiges Design, das mit der Erzeugung von NIR- 1030 nm-Impulsen beginnt, gefolgt von einer zweiten Stufe, in der die 1030 nm-Impulse durch nichtlineare Differenzfrequenzerzeugung (DFG) in die erforderlichen $6.8 \mu\text{m}$ -Impulse herunterkonvertiert werden.

Impulse von 1030 nm mit einer Dauer von 50 ns und einer Energie von 30 mJ werden in einem Dünnscheibenoszillator durch die Methode des Cavity Dumping innerhalb von $<1 \mu\text{s}$ erzeugt. Diese Impulse werden durch einen DünnscheibenMehrfachdurchlaufverstärker (TDA) auf eine Energie von 300 mJ verstärkt. Diese 1030 nm-Impulse werden zum Pumpen von zwei optischen parametrischen Oszillatoren (OPO) verwendet, die bei den Wellenlängen $2.1 \mu\text{m}$ und $3.1 \mu\text{m}$ arbeiten. Der $2.1 \mu\text{m}$ -OPO wandelt den 1030 nm-Impuls in Impulse der Wellenlänge $2.1 \mu\text{m}$ und $1.9 \mu\text{m}$ um, während der $3.1 \mu\text{m}$ -OPO den 1030 nm-Impuls in Impulse der Wellenlänge $3.1 \mu\text{m}$ und $1.5 \mu\text{m}$ umwandelt. In einem ähnlichen Prozess werden die $2.1 \mu\text{m}$ - und $3.1 \mu\text{m}$ -Impulse durch 1030 nm-Impulse in ihren jeweiligen optischen parametrischen Verstärkern auf Energien von 25 mJ bzw. 3 mJ verstärkt. Die $6.8 \mu\text{m}$ -Impulse werden schließlich durch Differenzfrequenzerzeugung

gung des 2.1 μm -Impulses und des 3.1 μm -Impulses erhalten. Der TDO und die beiden OPOs werden injiziert und mit einem Pound-Drever-Hall-Stabilisator (PDH) stabilisiert, um einen Einfrequenzbetrieb zu gewährleisten. Während die Wellenlänge der 1030 nm- und 2.1 μm -Impulse fest ist, kann die Wellenlänge der 3.1 μm -Impulse durch Änderung der Frequenz des Seed-Lasers variiert werden. Dadurch können die 6.8 μm -Impulse über den Suchbereich von 6798 nm - 6785 nm des 1S HFS in μH gescannt werden.

Diese Arbeit befasst sich mit der Entwicklung des 2.1 μm -OPO, des 2.1 μm -OPA, des 6.8 μm -DFG stage und der Frequenzkalibrierung der 6.8 μm -Impulse.

Kapitel 1 der Arbeit erläutert die Motivation für das Experiment und gibt einen Überblick über die theoretischen Arbeiten, die parallel zum Experiment durchgeführt wurden. Es werden Details des Versuchsaufbaus beschrieben, wobei der Schwerpunkt auf den Aspekten liegt, die die Anforderungen an das Lasersystem einschränken.

Kapitel 2 der Arbeit behandelt den Aufbau des in Entwicklung befindlichen Lasersystems, das diese Anforderungen erfüllen soll. Es wird ein kurzer Überblick über die Laserphysik und die nichtlineare Optik sowie über den aktuellen Stand des Lasersystems gegeben.

Kapitel 3 fasst die Ergebnisse zum 2.1 μm -OPO und die Auswirkungen auf dessen variablen Finesse-Hohlraumlayout zusammen. Die Auswirkungen der Injektions-Seeding- und PDH-Stabilisierung des Hohlraums auf die Energie und Stabilität werden untersucht. Die Erzeugung von 2.1 μm -Impulsen mit einer Energie von 1 mJ und einer durchschnittlichen Strahlqualität von $M^2 \sim 1,12$ bei einer Eingangsimpulsenergie von 5 mJ wird demonstriert.

Kapitel 4 beschreibt die Verstärkung der 2.1 μm -Impulse mit einer Energie von 1 mJ durch den 2.1 μm -OPA auf ~ 5 mJ, wobei ein Strahl mit einem durchschnittlichen M^2 von 1,56 bei einer Eingangsimpulsenergie von 25 mJ aus dem TDO bereitgestellt wird. Vorläufige Tests des 2.1 μm -OPA mit 1030 nm-Impulsen mit einer Energie von 95 mJ zeigen, dass die 2.1 μm -Impulse auf 22 mJ verstärkt werden.

Kapitel 5 konzentriert sich auf die 6.8 μm -DFG stage, die die 2.1 μm -Impulse in 6.8 μm -Impulse umwandelt. Aus 6 mJ 2.1 μm und 300 μJ 3.1 μm -Seed-Impulsen werden 300 μJ 6.8 μm erzeugt. Die Abhängigkeit des nichtlinearen Prozesses von der Ausrichtung und Temperatur des Kristalls sowie von der Frequenz des 6.8 μm -Strahls wird untersucht, um eine optimale Frequenz- und Energiekontrolle während der μH -Spektroskopie-Kampagne zu erreichen.

Kapitel 6 berichtet über die Frequenzkalibrierung der 6.8 μm -Impulse. mittels Absorptionsspektroskopie in einer Wasserdampfzelle werden drei Resonanzen von H_2O für verschiedene Drücke im Bereich von 0.1 mbar bis 7 mbar untersucht. Aus den gemessenen Resonanzkurven werden Resonanzfrequenzen und Breiten der gemessenen Übergänge ermittelt. Die erhaltenen Resonanzfrequenzen wichen alle systematisch um 50 MHz vom HITRAN-Wert ab, was darauf hindeutet, dass die Frequenzkalibrierung überprüft werden muss. Aus der Linienbreite wurde die Obergrenze der Laserbandbreite mit 110 MHz bestimmt. Dies erfüllt die Mindestanforderung für die Spektroskopie in μH .

In dieser Arbeit haben wir erstmals unsere Fähigkeit unter Beweis gestellt, 6.8 μm -Impulse mit der erforderlichen Frequenzsteuerung zu erzeugen. Um eine Energie von 3 mJ bei der 6.8 μm -Wellenlänge zu erreichen, ist eine Energieskalierung des Lasersystems erforderlich, aber die beobachtete Effizienz ist vielversprechend.

INTRODUCTION

1.1 HYPERFINE STRUCTURE IN HYDROGEN

The resonance frequency of the ground-state hyperfine splitting (HFS) of hydrogen (eH), $1S_{1/2}^{F=0}-1S_{1/2}^{F=1}$, is one of the most precise measurements made in physics [1]

$$\nu_{\text{HFS}}^{\text{exp}}(\text{eH}, 1S) = 1\,420\,405\,751.766\,7(9)\text{ Hz} \quad (1.1)$$

This spin-flip transition, called the hydrogen line or 21 cm line, is one of the most abundantly found in the observable universe with broad relevance [2]. The most recent theoretical prediction [3] based on the Standard Model of particle physics gives a value

$$\nu_{\text{HFS}}^{\text{th}}(\text{eH}, 1S) = 1\,420\,452.04(2)\text{ kHz} \quad , \quad (1.2)$$

where the main uncertainty arises from nuclear structure contributions. The precision of the theoretical prediction is about 20 Hz, a rather large value compared to the 1 mHz precision of the experimental result. With the new experiment of the CREMA collaboration, we aim to measure the same transition in muonic hydrogen (μH) also to improve the understanding of nuclear structure contributions in electronic hydrogen (eH).

1.2 MUONIC ATOM SPECTROSCOPY

In 1936, the muon (μ^-) was discovered by Anderson and Neddermeyer, who were studying cosmic showers [4]. Since then, muons have been well studied. These particles have been found to have the same electric charge as the electron while being ~ 207 times more massive [5]. However, in contrast to the electron, they are short-lived unstable particles that decay into an electron, electron-anti-neutrino and muon-neutrinos,

$$\mu^- \rightarrow e^- + \nu_{\mu} + \bar{\nu}_e \quad (1.3)$$

with a lifetime of $2.2\ \mu\text{s}$ [6]. Fortunately, this lifetime is long enough to enable their use in various high-precision experiments (such as the muon $g-2$ experiment [7], muonium laser spectroscopy [8], charged lepton-flavour violating decay experiments [9, 10, 11] and muonic atoms spectroscopy [12, 13, 14] to probe the limitations of the Standard Model of Particle Physics. Additionally, these leptons are useful for practical applications, such as studying properties of materials via the muon spin resonance (μSR) technique [15].

Muonic atoms, bound systems of a negatively charged muon and a positively charged nucleus, have been particularly useful in testing theories of nuclear structure. As the energy in an atomic system scales linearly with the reduced mass of the system, muonic atoms are more strongly bound compared to their electronic counterparts. They are easily formed by the incidence of muons into atomic systems where electrons are bound to a positively charged nucleus. Hydrogen-like muonic atomic systems have been the subject of research for the last several decades, as the results of such studies are easily combined

with their electronic counterparts, leading to the most advanced test of bound-state QED in few-body systems and to constrain beyond the Standard Model physics [16].

Remembering that the normalized 1S wavefunction for a hydrogen-like system [17] is given by

$$\Psi_{1S}(r) = \frac{1}{\sqrt{\pi a^3}} e^{-r/a} \quad , \quad (1.4)$$

where the Bohr radius a is given by

$$a = \frac{4\pi\epsilon_0\hbar^2}{m_{p\ell}e^2} \quad (1.5)$$

and scales inversely with reduced mass of the proton-lepton bound system $m_{p\ell} = m_p m_\ell / (m_p + m_\ell)$. Here, m_ℓ refers to the mass of the lepton, $e = 1.602176634 \times 10^{-19}$ C the elementary charge, $\hbar = 6.582 119 569 \times 10^{-16}$ Js⁻¹ the reduced Planck constant and $\epsilon_0 = 8.8541878188(14) \times 10^{-12}$ Fm⁻¹ the electrical permittivity of vacuum. The corresponding probability density function of finding the lepton between r and $r+dr$ in the radial direction for muonic hydrogen (μ H) to that in electronic hydrogen (eH) in their respective ground state is plotted in Fig. 1.1. The inverse-scaling of Bohr radius with the reduced mass means $a_{\mu H} \approx a_{eH}/187$, making the overlap factor of the μ^- wavefunction with that of the proton, $|\Psi_{1S}(r=0)|^2$, larger by $(a_{eH}/a_{\mu H})^3 \approx 10^7$ than that of the electron in eH

$$\frac{\Psi_{1S}^{\mu H}(r=0)}{\Psi_{1S}^{eH}(r=0)} = \frac{a_{eH}^3}{a_{\mu H}^3} \approx 10^7 \quad . \quad (1.6)$$

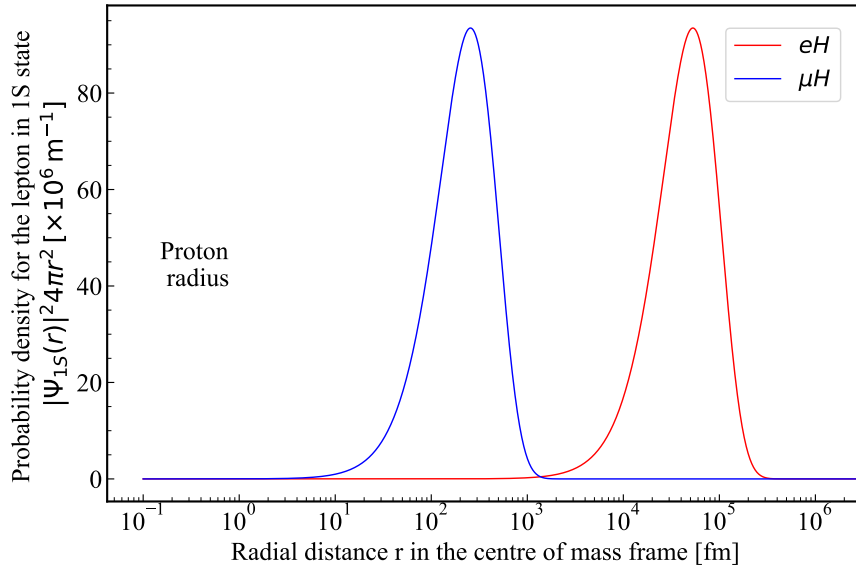


Figure 1.1: Probability density of finding a muon (blue) or electron (red) within the region r and $r+dr$ for the ground state of the lepton-proton bound system. The origin denotes the position of the proton. The spatial extent of the proton, of the order of 1 fm, is marked by the shaded region.

1.3 THE HYPERFINE SPLITTING IN MUONIC HYDROGEN

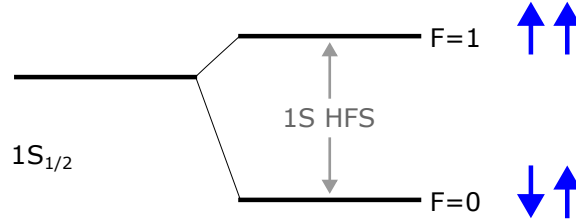


Figure 1.2: Energy level diagram of 1S HFS in μH showing the separation between the singlet ($F=0$) and triplet ($F=1$) states

The energy of the 1S hyperfine splitting in μH can be written as the sum of perturbative corrections as

$$E_{\text{HFS}}(1\text{S}, \mu\text{H}) = E_{\text{F}}^{\mu\text{H}} + \Delta_{\text{QED}+\text{weak}}^{\mu\text{H}} + \Delta_{\text{hVP}}^{\mu\text{H}} + \Delta_{\text{nucl.struct}}^{\mu\text{H}} \quad , \quad (1.7)$$

where

$$E_{\text{F}}^{\mu\text{H}} = \frac{8}{3} \alpha^4 \frac{m_{\text{p}\mu}^3}{m_{\text{p}} m_{\mu}} \frac{\mu_{\text{p}}}{\mu_{\text{N}}} = 182.443 \text{meV} \quad , \quad (1.8)$$

is the Fermi energy ¹. Here $\mu_{\text{p}} = 1.410\,606\,795\,45(60) \times 10^{-26} \text{JT}^{-1}$ is the anomalous magnetic moment of the proton, $\mu_{\text{N}} = 5.050\,783\,739\,3(16) \times 10^{-26} \text{JT}^{-1}$ the nuclear magneton and $m_{\mu} = 105.658\,375\,5(23) \text{MeV c}^{-2}$, $m_{\text{p}} = 938.272\,089\,43(29) \text{MeV c}^{-2}$, and $m_{\text{p}\mu} = 94.964\,471\,4(19) \text{MeV c}^{-2}$ denote the mass of the muon, the mass of the proton and the reduced mass of μH , respectively [18]. In comparison, the hyperfine splitting in eH [19] can be expressed as

$$E_{\text{HFS}}(1\text{S}, \text{eH}) = E_{\text{F}}^{\text{eH}} + \Delta_{\text{QED}+\text{weak}}^{\text{eH}} + \Delta_{\text{hVP}}^{\text{eH}} + \Delta_{\text{nucl.struct}}^{\text{eH}} \quad , \quad (1.9)$$

where the subscript denotes similar terms as in Eq:1.7.

The term $\Delta_{\text{QED}+\text{weak}}$ includes corrections from bound-state QED effects such as radiative, relativistic, binding and recoil corrections. Δ_{hVP} corresponds to corrections from the hadronic vacuum polarization. The remaining term, the nuclear structure contribution $\Delta_{\text{nucl.struct}}$, includes corrections related to the proton structure that, in leading order, is given by the two-photon contribution

$$\Delta_{\text{nucl.struct}} = \Delta_{2\text{PE}} + \Delta_{3\text{PE}} + \dots \quad , \quad (1.10)$$

where $\Delta_{2\text{PE}}$ refers to the corrections from the exchange of two virtual photons, $\Delta_{3\text{PE}}$ the corrections from the exchange of three virtual photons, and so on. The theoretical predictions of these corrections to HFS in μH and eH are curated in Table:1.1, along with relevant absolute uncertainties. Uncertainty on Δ_{hVP} is omitted as it is two orders of magnitude lower than the other terms. Extensive theoretical efforts in recent years have lowered the uncertainty in $\Delta_{2\text{PE}}$ to be nearly on par with that of $\Delta_{\text{QED}+\text{weak}}$. It is expected that the theoretical evaluations of $\Delta_{\text{QED}+\text{weak}}$ will become more precise in the coming years, leaving $\Delta_{2\text{PE}}$ once again the most uncertain of the corrections.

Conventionally, the two-photon exchange contribution is written as the sum of three

¹The uncertainty of the Fermi energy is dominated by the uncertainty of the muon mass and is omitted as it is comparatively lower than all the other relevant uncertainties

Correction term	μH [meV]	eH [neV]
ΔE_{HFS}^0	182.443	5867.851094(37)
$\Delta_{\text{QED+weak}}$	1.350(7)	6.670613(12)
Δ_{hVP}	0.004	0.0003
Δ_{TPE}	-1.161(2)	-0.1914(45)

Table 1.1: Perturbative corrections to 1S HFS in μH and eH.

contributions - the Zemach term Δ_Z , recoil term Δ_{rec} and the polarizability term Δ_{pol}

$$\Delta_{2\text{PE}} = E_F(\Delta_Z + \Delta_{\text{rec}} + \Delta_{\text{pol}}) \quad . \quad (1.11)$$

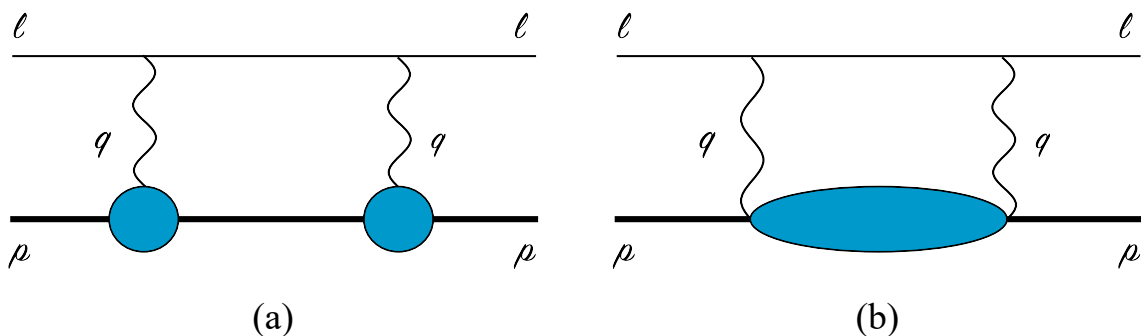


Figure 1.3: Feynman diagrams of (a) elastic and (b) inelastic two-photon exchange contribution. 'l', 'p' and 'q' refer to the lepton, proton and photon, respectively. The blue blob indicates the off-shell state of the proton.(reproduced from [19])

The corresponding Feynman diagram is shown in Fig.1.3. Of these, the Zemach term and the recoil term arise from elastic contributions (Fig.1.3 a) and can be expressed in terms of elastic form factors of the proton. In particular, the Zemach term can be expressed as [20, 21, 19]

$$\Delta_Z = \frac{8\alpha m_r}{\pi} \int_0^\infty \frac{dQ}{Q^2} \left[G_E(-Q^2) \frac{G_M(-Q^2)}{1 + \kappa_P} - 1 \right] \equiv -2\alpha m_r r_Z \quad , \quad (1.12)$$

where G_E and G_M are electric and magnetic form factors of the proton. Here

$$r_Z \equiv \frac{4}{\pi} \int_0^\infty \frac{dQ}{Q^2} \left[1 - G_E(-Q^2) \frac{G_M(-Q^2)}{1 + \kappa_P} \right] \quad (1.13)$$

has dimensions of length and is called the Zemach radius. In the non-relativistic limit, r_Z is related to the electric $\rho_E(r)$ and magnetic $\rho_M(r)$ spatial distributions of the proton [20]

$$r_Z^{\text{NR}} = \int r d^3r \int \rho_E(|\vec{r} - \vec{r}'|) \rho_M(r') d^3\vec{r}' \quad . \quad (1.14)$$

In essence, the Zemach radius encodes the magnetic finite size effect of the proton as a convolution of the electric and magnetic charge distributions. The polarizability term arises from inelastic contributions (Fig. 1.3 b) and is conventionally expressed using spin-

dependent inelastic structure functions as

$$\Delta_{\text{pol}} = \Delta_1 + \Delta_2 \equiv \frac{Z\alpha m_\mu}{2\pi(1 + \kappa_N) m_p} (\delta_1 + \delta_2), \quad (1.15)$$

where

$$\begin{aligned} \delta_1 &= 18 \int_0^\infty \frac{dQ}{Q} \kappa_0(Q^2) \left(\frac{2m_p^2}{Q^2} \int_0^{x_0} dx g_1(x, Q^2) + \frac{1}{4} F_2^2(Q^2) \right) \\ &\quad + 16m_p^4 \int_0^\infty \frac{dQ}{Q^3} \int_0^{x_0} dx \kappa_1(x, Q^2) g_1(x, Q^2), \\ \delta_2 &= 96m_p^2 \int_0^\infty \frac{dQ}{Q^3} \int_0^{x_0} dx \kappa_2(x, Q^2) g_2(x, Q^2), \end{aligned} \quad (1.16)$$

with x_0 the inelastic threshold, κ_i kinematic functions, g_1 and g_2 the structure functions and F_2 the Pauli form factor. The recoil correction is well-known and calculated to be $\Delta_{\text{rec}} = 846(6)$ ppm [22, 23] from measured form factors. It is noteworthy that these elastic corrections Δ_Z and Δ_{rec} can be obtained by scaling the values of their counterparts in eH. However, the dominant source of uncertainty in the two-photon exchange correction remains to be Δ_Z and Δ_{pol} .

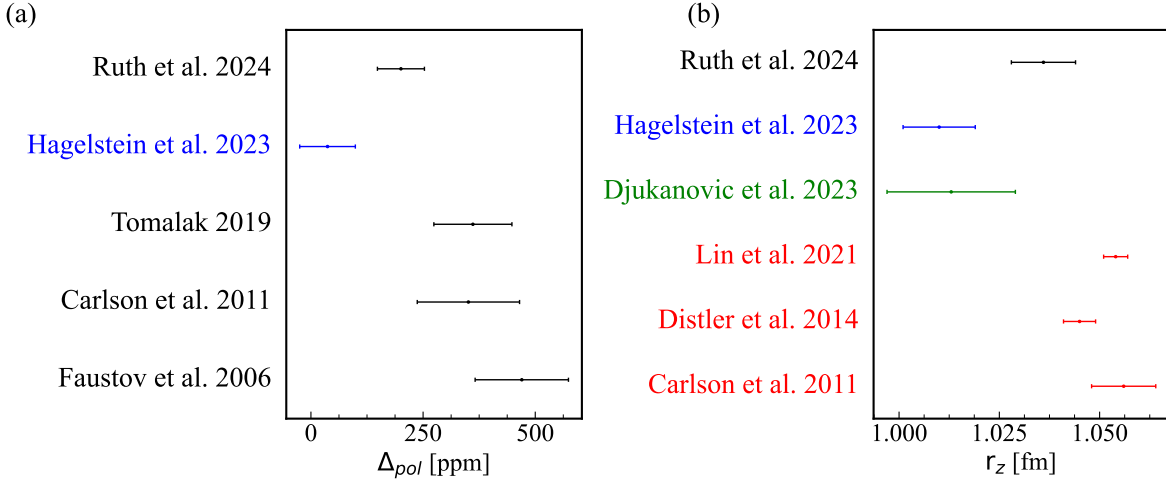


Figure 1.4: (a) Literature values for the polarizability correction Δ_{pol} in μH . The evaluations based on dispersive calculations and measured structure functions are given in black. In blue is given the value from $B\chi\text{PT}$. (b) Literature values of the Zemach radius. In red are given the values obtained from measured form factors. Green denotes the result from lattice QCD. Ruth et al. and Hagelstein et al. uses the corresponding values in the left panel of Δ_{pol} data in combination with data from eH.

The prior determinations of the Zemach radius and the polarizability contribution in μH are shown in Fig.1.4. The majority of these corrections (Ruth et al.[24], Tomalak [22], Carlson et al.[23],Faustov et al.[25]) calculate the polarizability correction in μH using dispersion relations, and spin-dependent structure functions obtained from polarized electron-proton scattering [26, 27, 28, 25, 29, 30, 31, 32]. The most recent results [33, 24] by Ruth et al. gives a comparatively lower value than prior evaluations due to the availability of data for the g_2 structure functions for the first time. In contrast to using ep scattering data, Hagelstein et al. [34] pursue an ab initio method using baryon chiral

perturbation theory (B χ PT) and obtains an even smaller value for Δ_{pol} , relative to Ruth et al, but compatible with it. The ep scattering experiments [35, 36, 37, 38, 39] of the past decades readily determines the elastic form factors G_E and G_M . These form factors are used to calculate both the recoil and the Zemach contribution.

The same form factors and structure functions can be used to calculate the polarizability and recoil correction in eH. This allows extraction of the Zemach radius r_Z of the proton from the measurement of 1S HFS in eH (Eq.1.1) and the appropriate corrections given in Eq.1.9 and Table 1.1. The value of r_Z shown in Fig.1.4-(b) by Ruth et al. and Hagelstein et al.[34] has been obtained in this way. Ab initio calculations of Djukanovic et al.[40] from Lattice QCD provide another value for r_Z . Lin et al.[41] and Distler et al. [36] give a value from model fits of the form factor via Eq. 1.13.

Currently, the relative uncertainty of the polarizability term is of the order of ~ 0.1 , larger by two orders of magnitude than the relative uncertainties in the Zemach radius and the recoil correction, both of which are ~ 0.001 .

The measurement of HFS in μH with about 1 ppm relative accuracy, as aimed by the CREMA collaboration, thus will result in a determination of the nuclear structure correction on the 2×10^{-4} level. From this determination, it is then possible to determine new values of the Zeemach radius when assuming Δ_{pol} from theory. Conversely, we can obtain Δ_{pol} when assuming values of r_Z from eH or ep scattering [19]. This value of the Zemach radius can be compared against those obtained from eH, ep scattering or ab initio methods, constituting another test of the Standard Model and nuclear structure.

Including all these contributions, the HFS transition energy is given by

$$E_{\text{HFS}}(1\text{S}, \mu\text{H}) = \underbrace{182.443}_{\text{Fermi energy}} \underbrace{-1.30653(17) \left(\frac{r_Z}{\text{fm}}\right) + E_F (1.01656(4) \Delta_{\text{recoil}} + 1.00402 \Delta_{\text{pol}})}_{\text{TPE}} + \underbrace{1.350(7)}_{\text{QED + weak}} + \underbrace{0.004}_{\text{hVP}} \text{ meV} \quad (1.17)$$

The transition energy corresponds to a frequency of 44 THz or the wavelength of 6788 nm (or shortly 6.8 μm). This wavelength corresponds to the mid-infrared region of the spectrum and is rather technologically challenging for laser spectroscopy. This thesis describes the laser system developed for the spectroscopy of 1S HFS in μH in the *HyperMu* experiment. The 1 ppm precision implies determining the centroid position on the 40 MHz level. To achieve this accuracy the laser bandwidth should be <100 MHz

1.4 HYPERMU EXPERIMENT

The goal of the HyperMu experiment is to determine the 1S hyperfine splitting ($1\text{S}_{1/2}^{\text{F}=1} - 1\text{S}_{1/2}^{\text{F}=0}$) in μH to a relative uncertainty of 1 ppm, i.e., a precision of 40 MHz, with laser spectroscopy. The experiment itself comprises three stages:

1. Generation of muonic hydrogen in a cryogenic target housing an enhancement cavity.
2. Laser excitation of muonic hydrogen by pulses of nanosecond duration and energy of ~ 1 mJ at the 6.8 μm wavelength (or equivalently, 44 THz frequency or 182 meV energy).
3. Detection of the laser-induced spin flip of a single μH atom.

The experiment is designed to be conducted in the $\pi E5$ beamline at the CHRISP facility of the Paul Scherrer Institute (PSI), Switzerland, where a continuous beam of negative muons is available.

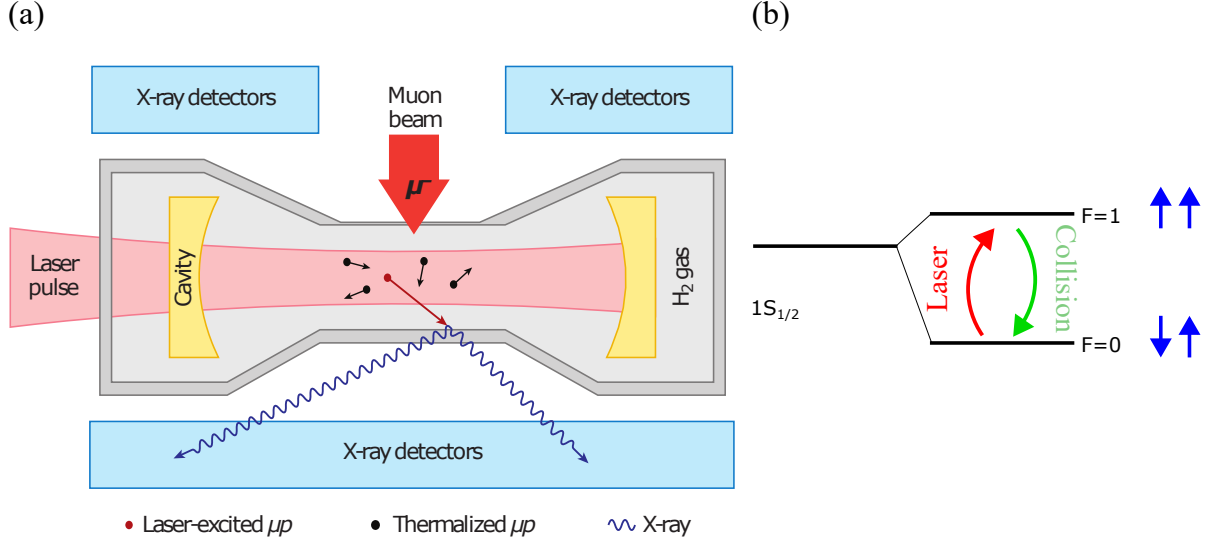


Figure 1.5: Principle of HyperMu experiment. (a) The experimental scheme features H₂ target where muons from the beamline form μH . The target encloses a toroidal enhancement cell that increases the laser fluence within the muon-stopping region. (b) Energy level diagram showing the laser excitation followed by the collisional de-excitation between the ground-state sublevels.

The final design of each aspect of the experiment is the culmination of extensive simulations and tests and is compiled in several doctoral theses and publications[42, 43, 44, 45, 46]. Here, we summarize the principle of the experiment and compile the results of the simulations to understand the requirements of the laser system for spectroscopy.

The principle of the experiment is given in Fig.1.5-(a). The setup consists of a low material budget hydrogen gas (H₂) target at a cryogenic temperature (22 K temperature, 0.5 bar pressure). A multipass toroidal enhancement cell encloses the region in the H₂ where the muons are stopped. This setup is surrounded by X-ray and electron detectors.

The incident muon beam from the beamline has a momentum of 12 MeV/c and a rate of 500 μ^- /s. After detection by an entrance counter, the incident muons propagate through an entrance window (10 μm -thick titanium) of H₂ gas target. Approximately 20% of the muons eventually are stopped in the H₂ gas in a disk-shaped volume (10 mm diameter, 1 mm thickness), with the rest stopping in the downstream target walls. These muons stopped in H₂ form μH in a highly excited state (principle quantum number $n \approx 14$)². Within a few nanoseconds after formation, the μH atoms de-excite to reach the 1S state and thermalize through collisions with H₂ in $\approx 1 \mu\text{s}$.

At this point, the laser pulses of 6.8 μm wavelength from the laser system enter the toroidal enhancement cell that surrounds the muon-stopping volume to excite the μH atoms from the $1S_{1/2}^{F=0}$ to $1S_{1/2}^{F=1}$ state. The enhancement cell is designed to maximize the fluence distribution within the muon-stopping volume by repeated reflection of the photons. The excited state $1S_{1/2}^{F=1}$ has a natural lifetime much longer than the muon lifetime.

²Energy conservation demands that the μH from a eH (in H₂) and a μ^- at rest, has binding energy equal to that of eH (~ 13.6 eV), which corresponds to $n \approx \sqrt{\frac{m_\mu}{m_e}} \approx 14$

Hence, it is not possible to determine the population of the excited state from the fluorescence of the $1S_{1/2}^{F=1}$ to $1S_{1/2}^{F=0}$ transition. An indirect detection method is thus designed (Fig.1.5-(b)). The laser-excited μH undergoes an inelastic collision with H_2 , gaining a kinetic energy of 0.1 meV (on average). At these large energies, the μH atom can diffuse efficiently in the H_2 gas and reach with significant probability the target walls. Gold atoms (Au) line the target walls and capture the μ^- from the μH to form μAu atoms in their excited state. The newly formed μAu atoms promptly de-excite, resulting in the emission of several characteristic X-rays at MeV energy [45]. These X-rays are detected by BGO detectors and serve as a signature of a successful laser-induced excitation.

The simulated time distribution of each μH arriving at the Au-lined target walls is shown in Fig.1.6-(a) where the signal from the muon entrance detector sets the time $t=0$. We assume that the laser pulses are coupled into the cavity at time $t=1000$ ns. As observed in the orange, which shows only the arrival times of μH undergoing a laser transition, it takes about 100 ns after excitation for the first μH atom to reach the target walls. An exponentially decaying background shows the non-laser excited μH that diffuses to the target walls. However, the laser pulses in-coupled at ~ 1 μs give rise to μH that arrive in the interval of 1100 ns to 1400 ns. This signal window of 1100 ns to 1400 ns is used to optimize signal/ $\sqrt{\text{background}}$ statistics. The HFS resonance is obtained by plotting the number of μAu -deexcitation events in this time window versus the laser frequency. An example is given in Fig.1.6-(b).

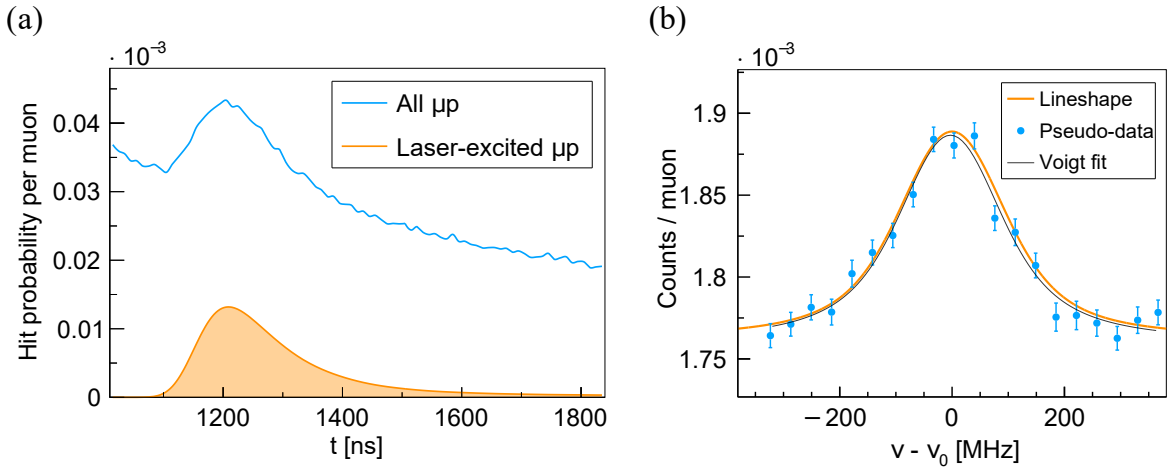


Figure 1.6: (a) Time distribution of arrival of μH at the target walls. Laser-excited μH diffuse faster than non-laser excited μH due to a higher kinetic energy of 0.1 eV. Detection of μH atoms within the time window 1100 to 1300 ns serve as the signal for μH excitation (b) Simulated resonance and pseudo data taking into consideration 2 weeks of beam time with 1 mJ pulse energy, 100 MHz bandwidth and enhancement cell reflectivity of 99.2%. The line shape is expected to be a Voigt profile broadened by collisions, Doppler effects, and laser parameters.

The laser excitation probability is closely related to the laser fluence distribution within the stopping volume. We note here that the 1S HFS $1S_{1/2}^{F=0}-1S_{1/2}^{F=1}$ transition in μH is an M1 transition with matrix element of $M_{\mu\text{H},1\text{S-HFS}} = 1.23 \times 10^{-34}$ m [46]. In comparison to the 2S-2P transition (E1) in μH , the transition previously measured by the CREMA collaboration [47], has a dipole matrix element of $M_{\mu\text{H},2\text{S}-2\text{P}} = 6.37 \times 10^{-32}$ m. Thus, the transition probability of 1S HFS transition in μH is smaller by a factor of

$|M_{\mu\text{H},1\text{S-HFS}}/M_{\mu\text{H},2\text{S-2P}}|^2 \sim 10^{-5}$. This means that the laser fluence requirement to excite the 1S HFS transition in μH is 10^5 times larger than the fluence for excitation of the 2S-2P transition.

Optical Bloch equations of the laser excitation and the subsequent collisional quenching of μH with H_2 were solved [46], considering collisional effects, Doppler broadening and laser bandwidth. These studies indicate that a peak fluence of $10\text{J}/\text{cm}^2$ for laser pulses of bandwidth 100 MHz provides a 20% probability of obtaining a μH atom that undergoes laser excitation followed by collisional quenching.

The high energy requirement is mitigated by the enhancement cell. The internal surfaces of the cell repeatedly reflect the spectroscopy pulses through the stopping volume, thereby allowing a relatively low-energy laser pulse to generate high fluence. Studies on the fluence distribution using optical ray tracing indicate that for a cavity reflectivity of 99.2% and diameter 100 mm, 1 mJ of pulse energy is needed by an ideal Gaussian beam (beam quality $M^2 = 1$) to obtain $\sim 12\text{J}/\text{cm}^2$. As continuous-wave lasers cannot satisfy the high energy requirement due to technical constraints, the laser photons must be pulses. Furthermore, assuming that the pulses are transform-limited Gaussian, the maximum bandwidth of 100 MHz implies that the laser pulses must have a minimal duration (FWHM) of $\tau = 0.44/100\text{MHz} \approx 4.4\text{ns}$ (See Eq.2.9). As we are aiming at a laser bandwidth of 10 MHz, we operate the laser system with pulses of $>40\text{ns}$.

These laser pulses must enter the toroidal enhancement cell after the μH thermalizes, i.e., $1\mu\text{s}$ after the μH formation. Thus, the laser system must be stochastically triggerable, sending in the laser pulse to excite the newly formed μH atom upon the signal sent by the muon entrance detector rather than continuously running at a constant repetition rate. For a muon of $500/\text{s}$ and a cavity reflectivity of 99.2%, the studies on μH diffusion, μAu de-excitation and X-ray detection efficiency (including background studies) [45] provide a signal rate of 0.06s^{-1} and a total background rate of 0.6s^{-1} for laser pulses of 1 mJ energy and 100 MHz bandwidth (FWHM). This limits the time $t_{4\sigma}$ needed to observe the signal with a 4σ significance over the background to be ~ 47 mins per frequency point. We also note here that the time duration $t_{4\sigma}$ decreases with higher repetition rate, lower bandwidth and higher pulse energy.

The simulated resonance for two weeks of data taking with 1 mJ laser pulse energy, a cavity reflectivity of 99.2% and $500\mu^-/\text{s}$ is shown in Fig.1.6-(b). The simulation shows that a linewidth of 220 MHz (at FWHM) is expected. This linewidth includes Doppler broadening, laser bandwidth and collisional effects. The frequency of the $6.8\mu\text{m}$ pulses must be tunable within the search range of $\pm 40\text{GHz}$ dictated by the theory uncertainty. Furthermore, the centre frequency of the pulses must be calibrated and known to $<40\text{MHz}$, prior to the spectroscopy campaign in μH , as we are aiming to 1 ppm uncertainty.

The resonance frequency measurement is limited by statistics. Systematic uncertainties are given mainly by pointing and fluctuations of the laser system. As the laser pulses must be mode-matched to the curvature of the enhancement cell and enter through an incoupling slit, pointing fluctuations, as well as energy fluctuations, can perturb the fluence distribution within the muon-stopping volume. An asymmetry in the performance of the laser system about the resonance (blue-red detuned sides) distorts the lineshape and, thus, the centroid determination. We estimate that the energy and centroid position of the laser beam must be stable up to $<1\%$.

Thus, the 8-week-long spectroscopy campaign calls for a stochastically triggerable highly-stable laser system that delivers $6.8\mu\text{m}$ pulses of 1 mJ energy, $\sim 50\text{ns}$ duration, 100 MHz bandwidth and $M^2 \sim 1$ within 900 ns when triggered, at an average repetition rate of

200 s⁻¹. These requirements posed on the laser system are summarized in Table.1.2, along with the main limiting factor in each case.

Parameter	Limiting factor	Requirement
Pulse build-up time	μ^- lifetime $\tau_\mu \sim 2.2 \mu\text{s}$	$<1 \mu\text{s}$
Trigger system	Continuous muon beam in PSI	Stochastic triggering
Average repetition rate	Required signal rate	200 s ⁻¹
Tunability	Theoretically expected search range	Single-frequency operation from 6798 nm - 6785 nm
Fluence	M1 dipole transition	2 J/cm ²
Pulse energy	Reflectivity of toroidal enhancement cell $\geq 99.2\%$	$\geq 1 \text{ mJ}$
Beam quality	Losses within enhancement cell	Beam quality $M^2 \sim 1$
Bandwidth	Excitation probability and required precision	$<100 \text{ MHz}$
Pulse duration	Laser bandwidth and lifetime of the enhancement cell	$\tau_p = 30\text{-}50 \text{ ns}$
Stability	8 weeks of spectroscopy campaign	1 % energy and pointing fluctuations

Table 1.2: Requirements of the 6.8 μm -laser system for spectroscopy in μH

HYPERMU LASER SYSTEM DESIGN

2.1 LASER PHYSICS AND PULSE GENERATION

A laser is a source of photons that are identical copies of one another. In a laser, a gain medium that emits photons when its atoms are de-excited is enclosed in an optical cavity. The simplest optical cavity consists of two mirrors that partially reflects the photons generated by the gain medium, thereby producing more photons by stimulated emission.

Pulses of photons can be generated by allowing the photons to circulate in the cavity for small losses and large gain to build up a large intracavity intensity. Extracting this circulating intensity from the cavity results in a pulse. This can be achieved through various methods, such as cavity dumping, Q-switching, Gain-switching, or mode-locking. The electric field of such a laser pulse with a Gaussian spatial and temporal profile is described by the equation

$$\vec{E}(\vec{r}, t) = \hat{e} \frac{E_0}{2} \frac{w_0}{w(z)} e^{-\frac{r^2}{w(z)^2}} e^{-i(kz - \omega t + k\frac{r^2}{2R(z)} - \psi(z))} e^{-\frac{t^2}{\tau^2}} + \text{c.c.}, \quad (2.1)$$

where c.c. denotes the complex conjugate of the previous term. We also assume that the pulse propagates in the \hat{z} direction and has focus at $z=0$. Here, E_0 is the amplitude of the Electric field, \hat{e} the direction of polarization of the electric field, $w(z)$ the beam radius at z along the propagation direction, $R(z)$ radius of curvature of the wavefront¹, w_0 the beam waist, τ the pulse duration, $k=2\pi/\lambda$ the magnitude of the wavevector $\vec{k} = k\hat{z}$ for wavelength $\lambda = c/\nu$ and frequency ν , $\omega = 2\pi\nu$ the angular frequency of light, c the speed of light in vacuum, $\psi(z) = \tan^{-1}(z/z_R)$ the Guoy phase and $z_R = \pi w_0^2/\lambda$ the Rayleigh range.

¹surfaces of constant phase

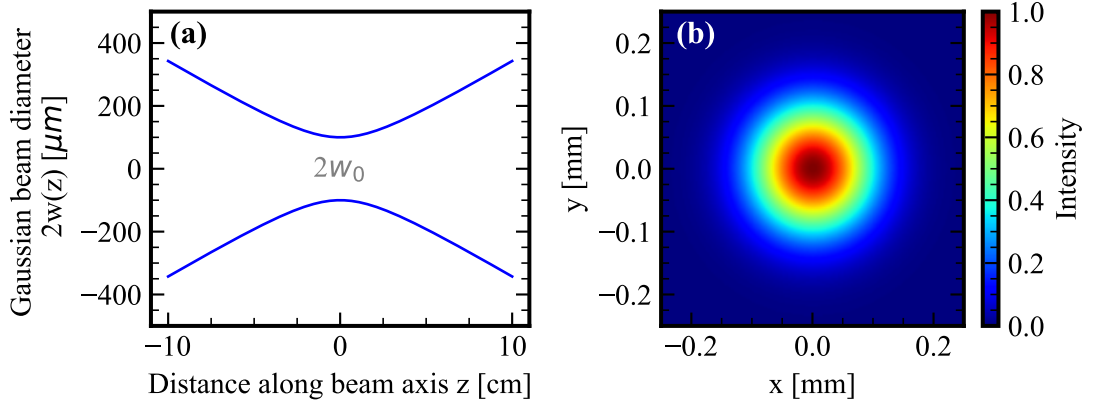


Figure 2.1: (a) Variation of beam diameter $2w(z)$ in the transverse direction (b) Transverse spatial profile of Gaussian beam

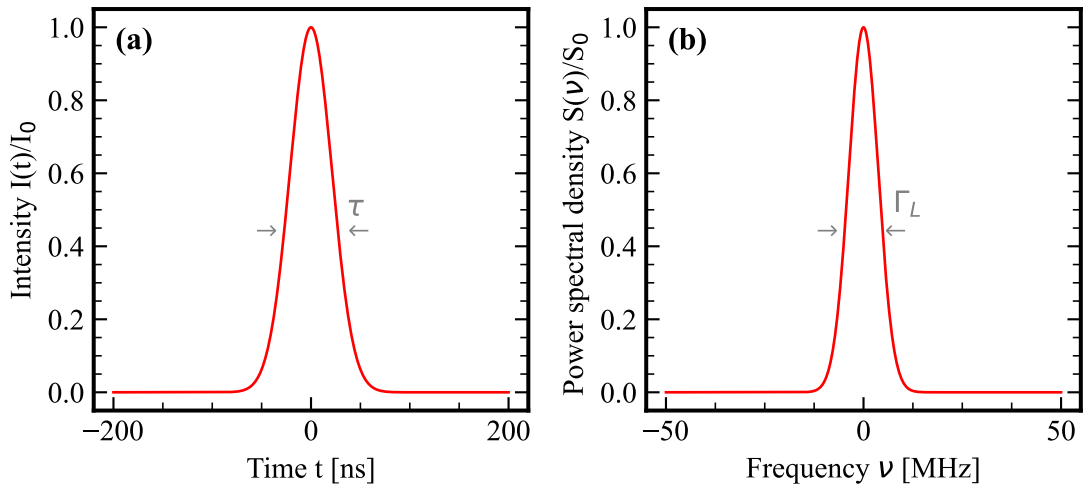


Figure 2.2: (a) Variation of intensity $I(t)$ with time t of a Gaussian pulse with FWHM pulse duration of $\tau=50$ ns (b) Power spectral density of the transform-limited ideal Gaussian pulse shown in (a). The bandwidth of the laser pulse is given by the FWHM of the power spectral density, calculated to be 8.8 MHz for $\tau_p=50$ ns

The intensity (optical power per unit area) of this laser pulse is given by

$$I(r, t) = \frac{c\epsilon_0 |E(r, t)|^2}{\pi w^2(z)/2} = I_0 e^{\frac{-2r^2}{w(z)^2}} e^{-\frac{4\ln(2)t^2}{\tau^2}}, \quad (2.2)$$

where ϵ_0 is the electrical permittivity of vacuum and $I_0=c\epsilon_0 w_0^2 |E_0|^2/\pi$ is the peak intensity. As the frequency ν in the optical regime is of the order of 10^{15} Hz, it changes too fast to be measured with electronic detectors (of bandwidth of order 10^9 Hz). Usually, the power or intensity is determined, and the beam radius $w(z)$ is defined as the radial distance at which the intensity falls to $1/e^2$ ($\approx 13.5\%$) of its peak value at that instant of time t . The pulse duration τ is the FWHM of the intensity profile $I(t)$ at the position z of the measurement.

For such an ideal Gaussian beam, the evolution of the beam waist $w(z)$ and the radius of curvature of the wavefront can be described by the equation

$$w^2(z) = w_0^2 \left[1 + \left(\frac{z}{z_R} \right)^2 \right] \quad \text{and} \quad \frac{1}{R(z)} = \frac{z}{z^2 + z_R^2} \quad . \quad (2.3)$$

Fig.2.1-a) shows such a variation of the Gaussian beam diameter with the position z along the beam axis at an instant of time t for a beam radius $w_0=0.1$ mm and wavelength $\lambda=1030$ nm. The beam strongly diverges at the waist $z=0$, with the beam diameter increasing only linearly after ~ 25 cm of propagation. Fig.2.1-b) shows the transverse spatial profile of the Gaussian beam at a certain position z . The ideal Gaussian has a radially symmetric profile.

Fig.2.2-a) shows the evolution of the intensity profile of a Gaussian pulse at the position z of pulse duration $\tau=50$ ns and peak intensity $I_0=1$ W/m² plotted using Eq.2.2. Fig.2.2-b) shows the power spectral density $S(\nu)$, calculated as

$$S(\nu) = |\tilde{E}(\nu)|^2 \quad (2.4)$$

where

$$\tilde{E}(\nu) = \mathcal{F}\{E(t)\} \quad (2.5)$$

is the Fourier transform of the temporal profile of the field given in Eq.2.1 at a given position. The bandwidth of the laser pulse is defined as the FWHM of the power spectral density $S(\nu)$. An ideal Gaussian pulse is transform-limited, which is to say that the variation of the phase $\phi(t)$ of the field is constant (equal to the angular frequency of the field).

$$\frac{d\phi}{dt} = \omega = \text{constant} \quad (2.6)$$

In the ideal case, the Fourier transform of the intensity profile $I(t)$ is proportional to the power spectral density

$$\mathcal{F}\{I(t)\} \propto S(\nu) \quad (2.7)$$

For the ideal Gaussian pulse, it can be shown that the power spectral density is a Gaussian centred around the centre frequency ν_0 with FWHM Γ_L .

$$S(\nu) = S_0 e^{-4\ln(2) \left(\frac{\nu - \nu_0}{\Gamma_L} \right)^2} \quad (2.8)$$

where S_0 is the peak value of the power spectral density. For transform-limited Gaussian pulses, the pulse duration τ and the bandwidth Γ_L are related by

$$\Gamma_L = \frac{2\log(2)}{\tau} \quad (2.9)$$

When laser beam profiles are elliptical instead of possessing cylindrical symmetry, beam waists along the two directions normal to the direction of propagation are defined and evolve respectively according to Eq.2.3. For example, for a beam propagating along \hat{z} , beam waists $w_x(z)$ and $w_y(z)$ along \hat{x} and \hat{y} , respectively, are defined. The spatial and temporal characteristics of a real laser beam deviate from those of an ideal Gaussian beam. Characterizing a temporal profile is easily achieved by measuring the intensity at point z with a photodetector, whereas to characterize the spatial profile of a real laser beam, one usually measures the transverse intensity distribution $I(x,y)$ of a real laser

beam at different positions z along the axis of the beam. Usually measured with a camera, transverse intensity distribution can be used to calculate the $D4\sigma$ beam diameter along, say, the x -direction, which can be determined as

$$D4\sigma_x = \sqrt{\frac{\int_{-\infty}^{\infty} \int_{-\infty}^{\infty} I(x, y) (x - \bar{x})^2 dx dy}{\int_{-\infty}^{\infty} \int_{-\infty}^{\infty} I(x, y) dx dy}} \quad , \quad (2.10)$$

where,

$$\bar{x} = \frac{\int_{-\infty}^{\infty} \int_{-\infty}^{\infty} I(x, y) x dx dy}{\int_{-\infty}^{\infty} \int_{-\infty}^{\infty} I(x, y) dx dy} \quad . \quad (2.11)$$

Note that this definition of a beam diameter takes into account the intensity distribution of a non-Gaussian real laser beam with $D4\sigma(z) = 2 w(z)$ only for an ideal Gaussian beam. By measuring $D4\sigma$ at different positions z along the axis of the beam, the angle of divergence of the beam is defined as

$$\Theta_x = \lim_{z \rightarrow \infty} \frac{D4\sigma_x(z)}{z} \quad (2.12)$$

can be determined. One can then define the beam quality factor M_x^2 of the beam along the x -direction as

$$M_x^2 = \frac{\pi D4\sigma_x \Theta_x}{\lambda} \quad (2.13)$$

For an ideal Gaussian beam $M_x^2 = 1$. This way, the spatial profile of a real laser beam is compared to that of an ideal Gaussian beam. A similar definition follows for $D4\sigma_y$, Θ_y and M_y^2 .

2.2 NONLINEAR OPTICS

When the light passes through a material, the dipoles in the material respond to the field so as to develop a field opposite to the field of the incident light, i.e, the material becomes polarized in response to the incident light field. In general, the wave equation for a field in a material reads

$$\nabla^2 \vec{E} - \frac{1}{c^2} \frac{\partial^2 \vec{E}}{\partial t^2} = \frac{1}{\epsilon_0 c^2} \frac{\partial^2 \vec{P}}{\partial t^2} \quad , \quad (2.14)$$

where \vec{P} is the polarization developed within the material due to the incident electric field \vec{E} . The polarization so developed due to the incident light field is dependent on the characteristics of the material as well as the magnitude and direction of the light field. In general, the i^{th} component of polarization developed (here, indices i, j, k and l take values 1, 2, 3 and correspond to components of the vector along the \hat{x} , \hat{y} , and \hat{z} direction, respectively) is given by

$$\begin{aligned} P_i(t; \omega) = \epsilon_0 \left[\sum_j \chi_{ij}^{(1)}(\omega) E_j(t; \omega) \right. \\ + \sum_{j,k} \chi_{ijk}^{(2)}(\omega; \omega_1, \omega_2) E_j(t; \omega_1) E_k(t; \omega_2) \\ \left. + \sum_{j,k,l} \chi_{ijkl}^{(3)}(\omega; \omega_1, \omega_2, \omega_3) E_j(t; \omega_1) E_k(t; \omega_2) E_l(t; \omega_3) + \dots \right] \quad (2.15) \end{aligned}$$

$$= P^L(t, \omega) + P^{NL}(t, \omega, \{\omega_N\}) \quad , \quad (2.16)$$

where we have separated the polarization that is linearly proportional to the incident field and the polarization which is nonlinearly dependent on the incident field. The linear part of the polarization is given by

$$P_i^L(t, \omega) = \epsilon_0 \sum_{j=1,2,3} \chi_{ij}^{(1)}(\omega) E_j(t; \omega) \quad , \quad (2.17)$$

and the non-linear part by

$$\begin{aligned} P_i^{NL}(t, \omega, \{\omega_N\}) = & \sum_{j,k=1,2,3} \chi_{ijk}^{(2)}(\omega; \omega_1, \omega_2) E_j(t; \omega_1) E_k(t; \omega_2) \\ & + \sum_{j,k,l=1,2,3} \chi_{ijkl}^{(3)}(\omega; \omega_1, \omega_2, \omega_3) E_j(t; \omega_1) E_k(t; \omega_2) E_l(t; \omega_3) + \dots \end{aligned} \quad (2.18)$$

Here, $\chi^{(N)}(\omega, \{\omega_N\})$ denotes the N^{th} -order optical susceptibility of the material at angular frequency ω when N photons interact within the material to generate a photon at the angular frequency ω . It is to be noted that susceptibility is generally a 3-dimensional tensor of rank $N+1$ that couples together electric fields in different directions. The material response is frequency dependent, as shown by the dependence of the susceptibility on the angular frequency ω . The linear response is to generate a field with the same frequency as the incident field.

Linear response - Refractive index and birefringence

The linear part of the polarization gives rise to the refractive index of the material. For optically isotropic materials, the susceptibility is independent of the polarization of the light. Essentially this means that the the first-order susceptibility $\chi^{(1)}$ is no longer dependent on the direction of polarization of the light. Mathematically, in this case $\chi^{(1)}$ is no longer a tensor of rank 2 but a scalar quantity. Such a material has only one refractive index, commonly represented as n and related to the first-order susceptibility by

$$n(\omega) = \sqrt{1 + \chi^{(1)}(\omega)} \quad (2.19)$$

As the refractive index is an effective property of the material, it is dependent on the temperature T of the crystal as well as the wavelength of light λ . In general, the variation of refractive index at wavelength λ with the temperature is described phenomenologically by the Sellmeier equation [48]

$$n^2(\lambda, T) = A(T) + \frac{B(T)}{1 - C(T)/\lambda^2} + \frac{D(T)}{1 - F(T)/\lambda^2} \quad (2.20)$$

where $A(T), B(T), C(T), D(T), F(T)$ are temperature dependent parameters unique to each material.

In contrast, optically anisotropic crystals can have more than one refractive index. We limit our discussion to uniaxial crystals - crystals are characterized by one direction of symmetry and hence have two refractive indices. For such crystals, there exists a direction for the propagation of light through the crystal for which the field experiences the

same refractive index, regardless of the polarization of light.

This is illustrated in Fig:2.3 for the case of propagation of light along the optic axis and normal to the optic axis. Consider light with polarization that is a mixture of s-polarization (say \hat{z}) and p-polarization (\hat{x})² incident on the surface of a uniaxial crystal. If the crystal is oriented such that its optic axis is along the direction of propagation of light \hat{y} , then both the polarizations experience the same refractive index. This refractive index is called ordinary refractive index n_o .

In contrast, when the optic axis of the crystal is not parallel to the direction of propagation of light, but rather, say, perpendicular to the direction of propagation, the field polarized along the optic axis observes the extraordinary refractive index n_e while the field polarized normal to the optic axis sees the ordinary refractive index. For an arbitrary angle of propagation through the crystal, the effective refractive index n_{eff} observed by the light has contributions both from n_o and n_e .

Note that the optic axis of the crystal is a property of the crystal structure, and the orientation of the crystal planes need not be aligned with the physical dimensions of the crystal. For a uniaxial crystal, the effective extraordinary refractive index is given by

$$\frac{1}{n_{e,eff}(\theta)} = \frac{\cos^2(\theta)}{n_o^2} + \frac{\sin^2(\theta)}{n_e^2} \quad , \quad (2.21)$$

where θ is the angle between the direction of propagation of light and the optic axis. Additionally, both the ordinary and extraordinary refractive indices are dependent on the temperature of the material and the wavelength by their respective Sellmeier equations (Eq.2.20)

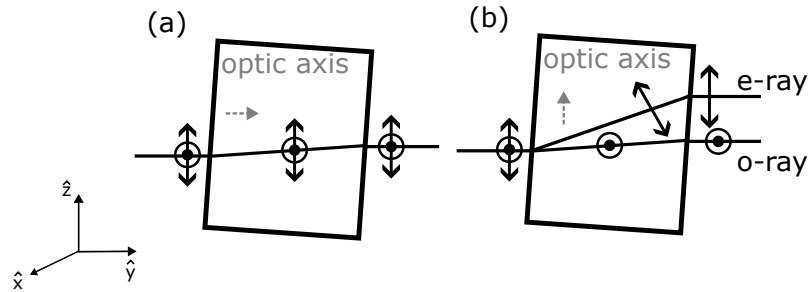


Figure 2.3: Illustration of birefringence for direction of propagation (a) along the optic axis (b) normal to the optic axis. Ordinary and extra-ordinary rays are assumed to be polarized along the \hat{x} and \hat{z} -axis, respectively.

Three-wave mixing

As seen from Eq:2.18, the nonlinear response of the material is a contribution dependent on the electric field of two or more light fields of different angular frequencies $\omega_1, \omega_2, \dots$. Interestingly, this gives rise to a polarization of angular frequency ω , subject to energy-momentum conservation, depending on the angular frequencies of the incident field. As a result, the oscillating dipoles that constitute this polarization emit photons of angular frequency ω in the direction of the incident fields. Thus, the nonlinear response of the material can generate photons of frequency different than the ones incident on it.

²s-and p-polarization refers to normal and parallel to the plane of incidence, respectively. For normal incidence to a surface, they can be chosen arbitrarily.

For a second-order nonlinear response, the possible generated frequencies from two input angular frequencies ω_1 and ω_2 are $|\omega_1 - \omega_2|$ (*Difference Frequency Generation*), $\omega_1 + \omega_2$ (*Sum Frequency Generation*), $2\omega_1$ and $2\omega_2$ (*Second Harmonic Generation*), and a DC field (*Optical Rectification*) (see Fig.2.4). The dominant nonlinear process is determined from the energy-momentum conservation relation for each process.

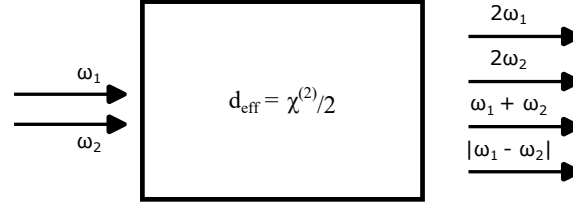


Figure 2.4: Possible three-wave mixing in nonlinear materials with non-vanishing second-order susceptibility.

To better understand three-wave mixing, we shall focus on the process of difference frequency generation involving plane waves. Specifically, we consider the case where a high energy *pump* field (of angular frequency ω_P) interacts with a *signal* field (ω_S) of lower energy to produce a new field termed the *idler* (ω_I). Assume that the incident fields (pump and signal) on the material are incident normal to the surface and collinear (propagating along \hat{z}) so that the generated field is also along the same direction. The wave equation implies that for a nonlinear frequency generation involving three waves, the electric fields evolve within the material as

$$\frac{dE_S}{dz} = \frac{2id_{\text{eff}}\omega_S^2}{k_S c^2} E_P E_I^* e^{i\Delta k z} \quad (2.22)$$

$$\frac{dE_I}{dz} = \frac{2id_{\text{eff}}\omega_I^2}{k_I c^2} E_P E_S^* e^{i\Delta k z} \quad (2.23)$$

$$\frac{dE_P}{dz} = \frac{2id_{\text{eff}}\omega_P^2}{k_P c^2} E_S E_I e^{-i\Delta k z} \quad , \quad (2.24)$$

where $d_{\text{eff}} = \chi^{(2)}/2$ is the nonlinear coefficient of the material along the axis of propagation \hat{z} , $\Delta k = k_S + k_I - k_P$. Note that we use scalar fields and assume that the polarization of each of the three fields is oriented appropriately to drive the nonlinear process (the polarizations may be normal or parallel to one another as we will see in the discussions below). Using the index notation, $i=P, S, I$, the terms $E_i, \omega_i = 2\pi\nu_i$ and k_i are the electric field amplitude at z , angular frequency and magnitude of wavevector of the i^{th} field.

The common factor $e^{-i\Delta k z}$ affects all three source terms³ at a point z within the crystal along the direction of propagation. Δk , called the phase-mismatch parameter, determines the period $2\pi/\Delta k$ at which the source terms oscillate between maximum and minimum. When $\Delta k \rightarrow 0$, the period $2\pi/\Delta k \rightarrow \infty$ and the source terms are maximum throughout their propagation. For all other values, the source terms vary sinusoidally.

This system of differential equations can be solved in terms of Jacobi elliptic sine function $\text{sn}(u, m)$ and cosine function $\text{cn}(u, m)$. The relevant calculations are available to the interested reader in [49]. We limit our attention to the scenario relevant to this thesis - where a pump and signal field of intensity $I_P(0)$ and $I_S(0)$ are incident at the face of the crystal (of length L) to generate a new idler field under ideal phase-matching conditions

³terms on the RHS of the PDE

($\Delta k=0$). The intensity of the fields at any point z within the crystal is then given by,

$$I_P(z) = I_P(0) \operatorname{cn}^2 \left(\frac{z}{L} \sqrt{\frac{I_P(0)}{I_{NL}}}, \gamma^2 \right) \quad (2.25)$$

$$I_S(z) = I_S(0) + I_P(0) \frac{\lambda_P}{\lambda_S} \operatorname{sn}^2 \left(\frac{z}{L} \sqrt{\frac{I_P(0)}{I_{NL}}}, \gamma^2 \right) \quad (2.26)$$

$$I_I(z) = I_P(0) \frac{\lambda_P}{\lambda_I} \operatorname{sn}^2 \left(\frac{z}{L} \sqrt{\frac{I_P(0)}{I_{NL}}}, \gamma^2 \right) \quad (2.27)$$

where

$$\gamma^2 = \frac{I_P(0)}{I_S(0) + I_P(0)} \quad (2.28)$$

denotes a measure of the fraction of pump photons to the total number of photons involved in the process and

$$I_{NL} = \frac{2\epsilon_0 c n_I n_S n_P \lambda_S \lambda_I}{16\pi^2 d_{eff}^2 L^2} \quad (2.29)$$

determines the scale-factor of the intensity for which the nonlinear process takes place. We note here the term $L\sqrt{I_{NL}/I_P(0)}$ is often referred to *phase-coherence length* in literature. For the above process, the conversion efficiency of the nonlinear process is given by

$$\eta \equiv \frac{I_P(0) - I_P(L)}{I_P(0)} = \operatorname{sn}^2 \left(\frac{z}{L} \sqrt{\frac{I_P(0)}{I_{NL}}}, \gamma^2 \right) \quad (2.30)$$

To better understand the difference frequency generation, we compare two important limits - one where the incident signal field is weak compared to the pump field and another where the incident signal field is strong compared to the pump field. To this end, we recollect here important approximations of the Jacobi elliptic function

$$\begin{aligned} \text{for } \gamma^2 \rightarrow 0, \\ \operatorname{sn}(x, \gamma^2) &\approx \sin(x) \\ \operatorname{cn}(x, \gamma^2) &\approx \cos(x) \\ \text{for } \gamma^2 \rightarrow 1, \\ \operatorname{sn}(x, \gamma^2) &\approx \tanh(x) \\ \operatorname{cn}(x, \gamma^2) &\approx \operatorname{sech}(x) \end{aligned} \quad (2.31)$$

Figure 2.5 shows the variation of the intensity of the pump, signal and idler fields for three values of γ^2 , i.e, for three different values of intensity of the incident signal field for the same intensity of the incident pump field. When there is a small amount of signal photons $I_S(0) \ll I_P(0)$, $\gamma^2 \sim 1$. As shown in Fig.2.5-a), the energy of the pump field is then transferred to the signal and idler fields, with their intensities increasing hyperbolically as

$$I_P(z) = I_P(0) \operatorname{sech}^2 \left(\frac{z}{L} \sqrt{\frac{I_P(0)}{I_{NL}}}, \gamma^2 \right) \quad (2.32)$$

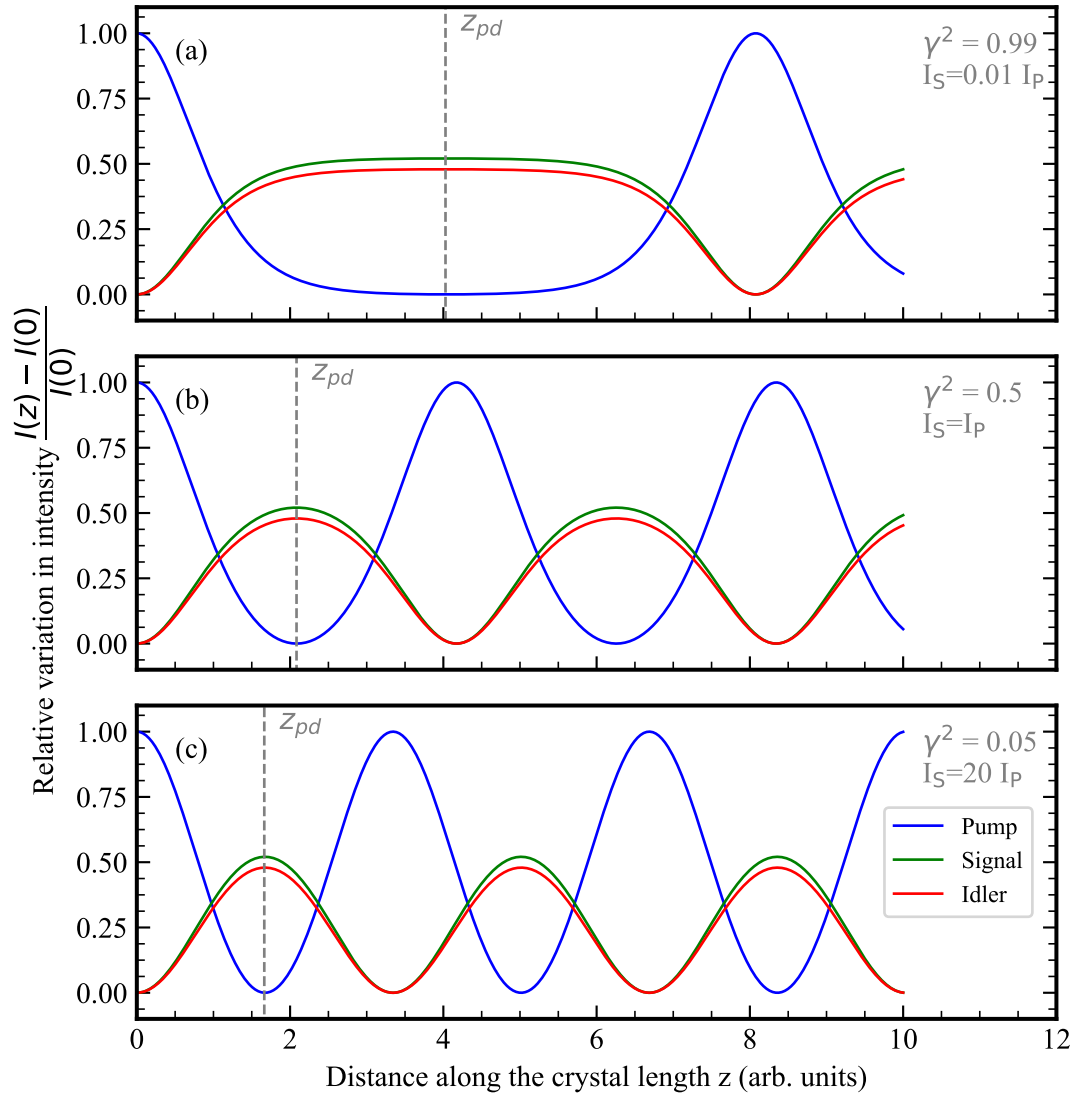


Figure 2.5: Relative variation in the intensities of the pump (blue), signal (green) and idler (red) fields for different ratios of incident signal to pump intensities (a) $I_S=0.01 I_P$ (b) $I_S=I_P$ (c) $I_S=20 I_P$. The legend in each case shows the corresponding values of γ^2 calculated using Eq.2.28. The point of pump depletion z_{pd} is marked as a grey dashed line.

$$I_S(z) = I_S(0) + I_P(0) \frac{\lambda_P}{\lambda_S} \tanh^2 \left(\frac{z}{L} \sqrt{\frac{I_P(0)}{I_{NL}}} \right) \quad (2.33)$$

$$I_I(z) = I_P(0) \frac{\lambda_P}{\lambda_I} \tanh^2 \left(\frac{z}{L} \sqrt{\frac{I_P(0)}{I_{NL}}} \right) \quad (2.34)$$

As the pump photons are split into idler and signal photons, the input signal field undergoes amplification by the pump field. Thus, the process is often called *optical parametric amplification* (OPA). One can further increase the conversion efficiency of the nonlinear process by enhancing the intensities using an optical cavity that is resonant for one or more of the fields participating in the nonlinear process. Such a system is called an *optical parametric oscillator* (OPO).

Once the pump field is fully exhausted, the signal and idler photons are converted by the nonlinear medium into new pump photons. This process called *back-conversion*, regenerates the pump field at the expense of the signal and idler fields. When pump field is fully regenerated, the energy once again flows from the pump field to the signal and idler fields. Thus, as the three fields propagate within the crystal.

In contrast, when there is equal or a much larger fraction of the signal photons $I_S \gtrsim I_P$, $\gamma \sim 0$ and the fields follow a sinusoidal evolution approximately. This can be seen by using the identity Eq.2.31 in Eq.2.25 to obtain the approximate solution

$$I_P(z) = I_P(0) \cos^2 \left(\frac{z}{L} \sqrt{\frac{I_P(0)}{I_{NL}}}, \gamma^2 \right) \quad (2.35)$$

$$I_S(z) = I_S(0) + I_P(0) \frac{\lambda_P}{\lambda_S} \sin^2 \left(\frac{z}{L} \sqrt{\frac{I_P(0)}{I_{NL}}} \right) \quad (2.36)$$

$$I_I(z) = I_P(0) \frac{\lambda_P}{\lambda_I} \sin^2 \left(\frac{z}{L} \sqrt{\frac{I_P(0)}{I_{NL}}} \right) \quad (2.37)$$

Fig.2.5-b) and (c) shows a plot of such scenarios with Fig.2.5-b) considering equal signal and pump intensities and Fig.2.5-c) considering a highly intense signal field for the same pump field. Although the signal intensity is large, each pump photon has a higher energy (since $\hbar\omega_P > \hbar\omega_S$). Thus, signal photons are not immediately converted to pump photons in both cases. Rather, the energy initially flows from the pump field to the signal and idler field until the pump is fully depleted.

Comparing Fig.2.5-b) and Fig.2.5-c) we see that the pump depletion occurs much earlier within the nonlinear crystal for a more intense signal field, and the fields evolve more sinusoidally than for a weaker signal field.

From Eq.2.25 we recognize that the points of pump-depletion z_{pd} are simply the maxima of the $\text{sn}^2 \left(\frac{z}{L} \sqrt{\frac{I_P(0)}{I_{NL}}}, \gamma^2 \right)$ function. Due to its periodicity, the points of maxima are determined by γ^2 and by I_{NL} . For $\gamma^2 \sim 0$, we obtain the familiar expression of the maxima for the sine-function so that, in this case,

$$z_{pd} = \frac{\pi L}{2} \sqrt{\frac{I_{NL}}{I_P(0)}} \quad (2.38)$$

Thus, the larger I_{NL} implies that the fields must propagate within the nonlinear crystal much further to completely transfer energy from the pump field to the idler and signal fields. This result can be extended to a Gaussian pulse using the relation $I_P = 2E_P/\pi w_P^2$ so that

$$z_{pd} = \frac{\pi L}{2} \sqrt{\frac{2I_{NL} \tau_P w_P^2}{E_P(0)}} \propto \frac{n_I n_S n_P \lambda_S \lambda_I w_P}{d_{eff}^2} \sqrt{\frac{\tau_P}{E_P(0)}} \quad (2.39)$$

using Eq.2.29. Since $\lambda_P = \lambda_S \lambda_I / (\lambda_S + \lambda_I)$ by virtue of the difference frequency generation process, we can express the product $\lambda_S \lambda_I$ in terms of the deviation from the pump wavelength δ defined so that

$$\delta = \frac{2\lambda_P - \lambda_S}{\lambda_S} = \frac{\lambda_I - 2\lambda_P}{\lambda_I} \quad (2.40)$$

This gives

$$z_{pd} \propto \frac{n_I n_S n_P w_P \lambda_P^2}{d_{eff}^2 (1 - \delta^2)} \sqrt{\frac{\tau_P}{E_P(0)}} \quad (2.41)$$

Thus, a nonlinear crystal with smaller refractive indices and a higher effective nonlinear coefficient can achieve the transfer of energy from the pump field to the idler and signal field with a shorter length. The physical dimensions of nonlinear crystals are often constrained by the crystal growth's technical feasibility. In such cases, the point of pump depletion z_{pd} can be adjusted for a given input pump energy $E_P(0)$ by tuning the Gaussian beam waist w_P of the pump, with a smaller Gaussian waist leading to earlier pump depletion. Similarly, for longer pulses, the nonlinear conversion process becomes increasingly difficult.

Eq.2.41 implies that as $\delta \rightarrow 0$, i.e, as $\lambda_S, \lambda_I \rightarrow 2\lambda_P$, z_{pd} attains the its minimum value, implying that for quasi-degenerate operation, the nonlinear conversion is most efficient. However, if the wavelengths are far apart ($\delta \rightarrow 1$, the conversion efficiency decreases. Generally, one would like to drive the difference frequency generation to obtain a particular idler or signal wavelength, and often, the wavelength of the pump field is pre-set by technical requirements. However, in a multistage nonlinear conversion scheme (as in our system), the freedom of choice of wavelength exists. By choosing the wavelength of the signal and idler field to be close to half the wavelength of the pump field, a more efficient nonlinear process is obtained.

While the nonlinear conversion process is much easier with a smaller Gaussian waist w_P and shorter pulse durations τ_P , the nonlinear material can only withstand a limited fluence. The maximum input fluence of the light field before it is optically damaged is described by its *damage threshold*. The damage threshold is often expressed as a fluence (unit J/cm²). It is empirically understood to have an inverse-square-root dependence on the pulse duration τ_P

$$F_{DT} \propto \sqrt{\tau_P} \quad (2.42)$$

Thus, longer pulses allow for much safer operation as the input fluence is farther away from the damage threshold regime while the nonlinear process becomes less efficient.

Phase matching

As the energy and momentum of a photon are proportion to ω and k , respectively, energy conservation for this process demands that

$$\omega_I = \omega_P - \omega_S \quad , \quad (2.43)$$

and momentum conservation implies $\Delta k = 0$, i.e,

$$k_I \hat{z} = k_P \hat{z} - k_S \hat{z} \quad , \quad (2.44)$$

for collinear propagation. Using the dispersion relation of the form $k = n(\omega)\omega/c$ for each of the three waves, Eq.2.44 becomes

$$n(\omega_I) \frac{\omega_I}{c} = n(\omega_P) \frac{\omega_P}{c} - n(\omega_S) \frac{\omega_S}{c} \quad . \quad (2.45)$$

For both Eq.2.43 and Eq.2.45 to be satisfied at the same time, it would imply that the refractive index of the material at each of the frequencies are equal: $n(\omega_P) = n(\omega_S) = n(\omega_I)$. Such a condition is satisfied only if the direction of propagation of the incident light and the material properties (temperature, internal domains,..) are optimized. The method by which these conditions are optimized to drive a specific non-linear process within the crystal is called *phase matching*. Of relevance to this thesis are the techniques of *angular phase matching* and *quasi-phase matching*.

Angular phase-matching

Angular phase matching uses the anisotropy in the nonlinear crystal that gives rise to birefringence to satisfy the condition $\Delta k = 0$. Note that the refractive index depends on the polarization of the light field as well as its direction of propagation within the crystal as per Eq.2.21. The variation of refractive index with wavelength as per the Sellmeier equation (Eq.2.20) can be compensated by propagating the light fields at an angle with the optic axis and orienting their polarizations appropriately. This angle between the propagation vector and the optic axis of the crystal for which $\Delta k = 0$ is called the phase-matching angle θ_{PM} . Typically, the phase-matching where the idler and the signal fields are oriented parallel is called *Type-I* phase-matching and when they are oriented orthogonal to one another is called *Type-II* phase-matching. For both types of phase-matching, the phase-matching angle as well as the effective nonlinear coefficient d_{eff} depends on the type of crystal structure. A discussion of the topic is omitted here, and the interested reader is referred to [50, 51].

Remembering that maximum transmission is obtained at normal incidence to the plane of the crystal ⁴, this implies that the physical faces of the crystal must be cut so that the propagation axis within the crystal corresponds to normal incidence. Despite the technical challenges posed by the manufacturing limitations, several nonlinear crystals can be engineered for angular phase-matching.

However, one of the disadvantages of angular phase matching arises from the fact that the direction of energy propagation, described by the Poynting vector \vec{S} , is not parallel to the direction of the wavevector \vec{k} when the incident fields are propagating at the angle with the optic axis of the crystal. We recollect from [17] that the Poynting vector is given by

$$\vec{S} = \frac{1}{\mu_0} \vec{E} \times \vec{B} \quad (2.46)$$

where μ_0 is the magnetic permeability, and we have assumed that the nonlinear material is non-magnetic. The direction of the wavevector is determined as the normal to the wavefront, i.e, the normal to the surface described by Maxwell's equation $\nabla \cdot \vec{D} = 0$, where $\vec{D} = \epsilon_0 \vec{E} + \vec{P}$ is the electric displacement vector. The polarization vector is not nec-

⁴from Fresnel equation

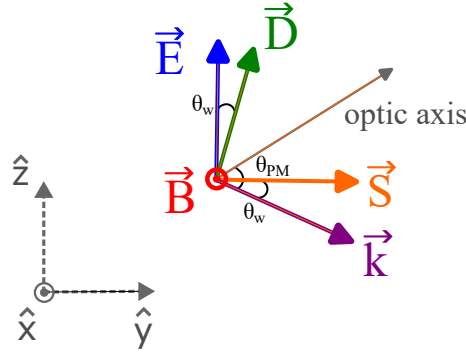


Figure 2.6: Illustration of the walk-off effect due to optical anisotropy. When the incident light field is propagating at an angle ϕ with the optic axis of the crystal, the electric field \vec{E} and the displacement vector \vec{D} of the field are not parallel due to the birefringence. Thus, the Poynting vector \vec{S} and the wavevector \vec{k} make an angle.

essarily parallel to the electric field \vec{E} as per Eq.2.17. Suppose as in Fig.2.6 that the magnetic field \vec{B} is along \hat{x} and the electric field vector \vec{E} is along \hat{z} , then the Poynting vector is along \hat{y} . The electric displacement vector \vec{D} is along the direction $\cos \theta_w \hat{x} + \sin \theta_w \hat{y}$, where θ_w is the angle between the \vec{E} and \vec{D} due to the anisotropy in polarization. As the wavevector \vec{k} must be normal to both \vec{D} and \vec{B} , the angle between the wavevector and the Poynting vector is also θ_w . Thus, the incident fields move away from each other as they propagate within the crystal, thereby deteriorating the overlap between the fields. This phenomenon, termed *walk-off*, decreases the efficiency of the nonlinear process with increasing propagation distance across the crystal. Moreover, as the spatial beam profile of the fields that gain in energy during the nonlinear process depends on the overlap, the walk-off effect leads to spatial profiles that deviate from that of an ideal Gaussian beam. The angle θ_w , called the *walk-off* angle, is given by

$$\theta_w = \tan^{-1} \left(-\frac{1}{n} \frac{\partial n}{\partial \theta_{PM}} \right) \quad (2.47)$$

Thus in general, a high refractive index and a large phase matching angle can lead to larger walk-off. As the refractive index also depends on the polarization, we note that the one of the fields can be chosen to have zero walk-off by polarizing the beam such that it sees only the ordinary refractive index n_o . Usually, this field is taken to be the pump field as most materials have refractive indices that decrease with increasing wavelength to minimize the walk-off effect.

The spatial overlap between the beams within the crystal is also determined by their Gaussian beam waists, incident beams with large beam waists provide more overlap to facilitate the nonlinear process over the same length than beams with smaller beam waists. As large beam waist leads to lower intensity, the trade-off between a better spatial beam quality due to reduced walk-off and lower conversion efficiency needs to be considered.

Quasi-phase-matching

Quasi-phase-matching is a method that bypasses the use of birefringence and relies on engineering the ferroelectric domains of a nonlinear crystal to achieve phase-matching

over a period within the crystal. Here, the crystal is fabricated such that the polarization of its ferroelectric domain is alternating periodically along the length of the crystal at the period Λ . The process called *periodic poling* gives rise to a spatially varying effective nonlinear coefficient given by

$$d(z) = d_0 \text{rect}(z, \Lambda) \quad (2.48)$$

where $\text{rect}(z, \Lambda)$ is a rectangular wave given by

$$\text{rect}(z, \Lambda) = \begin{cases} 1 & \text{if } 0 \leq z \leq \Lambda/2 \\ -1 & \text{if } \Lambda/2 < z \leq \Lambda \end{cases} \quad (2.49)$$

and $\text{rect}(z, \Lambda) = \text{rect}(z + \Lambda, \Lambda)$ and d_0 is the nonlinear coefficient along the poling axis of the crystal. Often, the poling axis of the crystal is chosen as the direction along which the nonlinear coefficient is maximum. Figure 2.7 shows an illustration of the ferroelectric domains in an un-poled crystal and a periodically-poled nonlinear crystal. This alternating

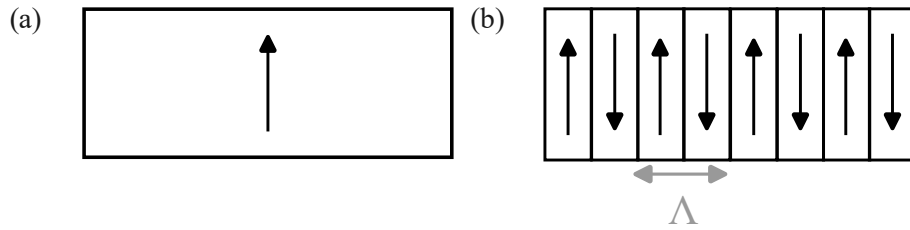


Figure 2.7: Illustration of the arrangement of ferroelectric domains in a periodically-poled crystal

structure of polarization partially compensates for the phase mismatch Δk within each cycle of period Λ . Using the Fourier transform of $\text{rect}(z, \Lambda)$, we can write Eq.2.48 as

$$d(z) = d_0 \sum_{N=-\infty}^{N=+\infty} \frac{2}{N\pi} \sin\left(\frac{N\pi}{2}\right) e^{\frac{i2\pi Nz}{\Lambda}} \quad (2.50)$$

Comparing this result with Eq.2.22, we see that $e^{\frac{i2\pi nz}{\Lambda}}$ changes the phase-matching condition from $\Delta k = k_I + k_S - k_P = 0$ to

$$\Delta k_N = k_I + k_S - k_P - \frac{2\pi N}{\Lambda} = 0 \quad (2.51)$$

The index n determines the order of quasi-phase-matching and the effective nonlinear coefficient as $d_{\text{eff}}^N = 2d_0/N\pi$. The reduction in the effective nonlinear coefficient with n prompts us to engineer the crystal so that first-order quasi-phase-matching ($N=1$) is dominant. This implies that the required poling period Λ can be calculated as

$$\Lambda = \frac{2\pi}{k_I + k_S - k_P} \quad (2.52)$$

The poling period Λ depends on the refractive index n through the wavevectors ($k = n\omega/c$). However, the degree of freedom offered by the poling period allows us to set the direction of propagation to parallel the optic axis ($\theta = 0$), thereby avoiding walk-off effects altogether. The spatial beam quality of the incident fields is preserved as the overlap of the incident fields is maintained throughout the crystal during their propagation.

In practice, the poling period is ultimately set by the wavelengths and the required

operating temperature to facilitate a particular nonlinear process.

Effect of phase-mismatch

It is clear from Eq.2.22 that a deviation from the phase-matching condition $\Delta k = 0$ reduces the nonlinear conversion process. One can show that the conversion efficiency η falls from its maximum value η_{\max} as a sinc^2 -function with increasing phase mismatch [50].

$$\eta = \eta_{\max} \text{Sinc}^2(\Delta kL/2) \quad (2.53)$$

where L is the length of the crystal. This relation is fully valid for nonlinear interaction involving a highly intense pump field compared to a signal field and approximately holds in all other cases. As the wavevector depends on the refractive index $n(T, \theta)$ as $k = n\omega/c$, the phase mismatch due to un-optimum temperature and angle θ can be written as Taylor series about the optimum $\Delta k = 0$

$$\Delta k = \frac{\partial n}{\partial T}(T - T_0) + \frac{\partial n}{\partial \theta}(\theta - \theta_0) + O(2) \quad (2.54)$$

where $T - T_0$ and $\theta - \theta_0$ refer to deviation from the optimum phase-matching temperature T_0 and angle θ_0 , respectively and $O(2)$ refers to the higher-order terms in the Taylor series. Within the phase-matching region, the variation of the refractive index due to either of these parameters is small and can be considered to be constant. Under this assumption, we find that $\Delta k \propto T - T_0, \theta - \theta_0$ so that the conversion efficiency

$$\eta = \eta_{\max} \text{Sinc}^2\left(0.886 \frac{T - T_0}{\Delta T}\right) \text{Sinc}^2\left(0.886 \frac{\theta - \theta_0}{\Delta \theta}\right) \quad (2.55)$$

where ΔT_{FWHM} and $\Delta \theta_{\text{FWHM}}$ indicate the temperature and angular phase-matching bandwidths, respectively.

2.3 GENERAL LAYOUT

The requirements of the laser system for the μH spectroscopy experiment were compiled in Table.1.2 (See Chapter 1). To couple in pulses of 1 mJ energy at 6.8 μm wavelength into the toroidal enhancement cell, we aim to generate 3 mJ energy to account for unoptimized in-coupling, a non-Gaussian beam ($M^2 > 1$) and propagation losses of the spectroscopy pulse from the laser system to the beamline (from atmospheric moisture, optical elements, etc...). Figure 2.8 shows the layout of the laser system. The principle of the laser system lies in the downconversion of NIR pulses (1030 nm) into 6.8 μm pulses in two steps of difference frequency generation. It consists of 4 stages :

- the 1030 nm thin-disk laser system that generates single-frequency pulses of >200 mJ energy and 50 ns duration within 900 ns upon trigger.
- the 2.1 μm -MOPA that downconverts the 1030 nm pulses into pulses of wavelength 2149 nm and 25 mJ energy.
- the 3.1 μm -MOPA that downconverts the 1030 nm pulses into pulses of wavelength 3143 nm and 3 mJ energy.
- a 6.8 μm -DFG stage that generates the required 6.8 μm pulses of 3 mJ energy from 2149 nm and 3143 nm pulses.

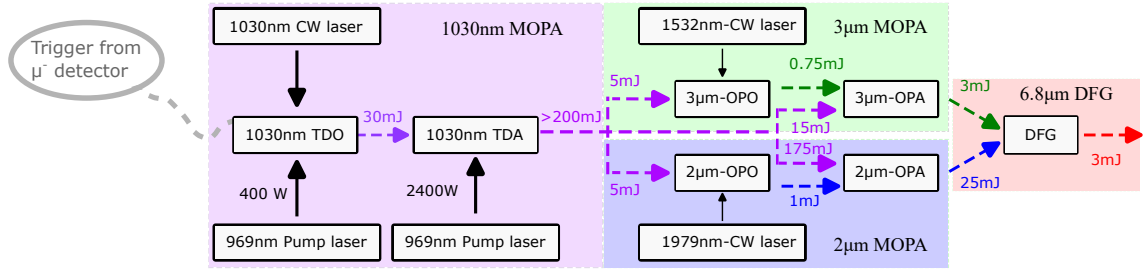


Figure 2.8: Layout of the laser system for HyperMu experiment. Pulses of 1030 nm wavelength (violet) and 50 ns duration are generated and amplified in a Yb:YAG thin disk laser MOPA that is pumped with high-power CW-diode lasers. These pulses of energy >200 mJ are downconverted via difference frequency generation in two MOPA branches - 2.1 μm (blue) and the 3.1 μm branch (green), which produce pulses of 25 mJ energy at 2149 nm wavelength and 3 mJ energy at 3143 nm wavelength, respectively. Pulses of 3 mJ energy at the required wavelength of 6.8 μm (red) are generated in the 6.8 μm -DFG stage from the difference frequency generation between the 2149 nm pulse and the 3143 nm pulse. The wavelength of the seed laser of the 3.1 μm -OPO is scanned to scan the wavelength of the 6.8 μm spectroscopy pulses.

The 1030 nm, 2.1 μm and 3.1 μm pulses are generated in a injection-seeded PDH-stabilized cavity to ensure single-frequency operation. While the frequency of the 1030 nm and 2.1 μm pulses are fixed, the frequency of the 3.1 μm pulses can be tuned to scan the frequency of the 6.8 μm pulses across the resonance in μH .

Two-step DFG stage and choice of wavelengths

Within the current limits of laser technology, direct generation of 3 mJ energy of 6.8 μm laser pulses of duration 50 ns with a single laser system is not possible due to the lack of an appropriate gain medium. The most frequent approach in generating pulses with wavelength in the mid-infrared involves a two-stage design - generation of laser pulses of wavelength centred in the near-infrared (from 780 nm to 2500 nm) of required pulse duration and spectral profile in a pulsed laser, followed by a nonlinear optical downconversion stage that converts these pulses in the near-infrared regime to the mid-infrared regime using difference frequency generation [52, 53]. The availability of nonlinear crystals with a high enough nonlinear coefficient, large aperture size, low absorption and high damage threshold determines the efficiency and feasibility of such designs. Table.2.1 compares the figure-of-merit d_{eff}/n^3 and damage threshold of different nonlinear crystals in their respective transparency window. Here, the maximum possible d_{eff} is chosen for the calculation. Zinc germanium phosphate (ZGP) is the most efficient nonlinear crystal for generating 6.8 μm . It is commercially available for large apertures (\sim cm), offers high damage threshold (2 J cm^{-2} for 10 ns pulses of 2 μm) and transparent between 2 μm to 8 μm with very high figure-of-merit ($\sim 183\text{ pm}^2/\text{V}^2$). However, the transparency window of ZGP implies that the pump photons must have be of wavelength >2 μm .

Laser pulses of wavelength near 2 μm can be directly generated in thulium or holmium-based laser systems. Such laser systems are typically designed as fibre lasers or rod lasers due to the low-emission cross-sections of their gain medium. This makes the high-energy requirement of the pump photons for the short pulse-build up time of 900 ns challenging for nanosecond pulses.

Nonlinear Crystal	Transparency range	d_{eff} [pm V ⁻¹]	Refractive index	Figure-of-merit d_{eff}^2/n^3 [pm ² V ⁻²]	Damage threshold [J cm ⁻²]
PPLNB	330 - 5500 nm	14.81	2.18	21.17	6.7
PPKTP	350 - 4500 nm	9.33	1.74	16.52	33
LNB	330 - 5500 nm	4.96	2.18	2.37	6.7
KTP	350 - 4500 nm	2.5	1.74	1.27	33.5
RTP	350 - 4500 nm	2.77	1.75	1.43	33.5
KTA	350 - 4000 nm	2.28	1.76	0.95	33.5
ZGP	2000 - 8000 nm	75	3.13	183	4.5
AgGaSe ₂	700 - 18000 nm	33	2.7	55	1.7
CSP	660 - 6600 nm	84	3.2	215	7.2
OP-GaP	700 - 12500 nm	50	3.0	92	9.8

Table 2.1: Comparison of nonlinear crystals: Nonlinear coefficient d_{eff} (generally constant over transparency range), refractive index, figure-of-merit (FOM), damage threshold, and pump energy. 'PP' in PPLNB indicates that the crystal of LNB is periodically-poled and optimized for quasi-phase-matching. Similar holds for PPKTP.

The problem of generating pulses of wavelength 2 μm can be solved by a nonlinear conversion stage. Table 2.1 lists several nonlinear crystals, such as PPLNB, PPKTP, etc... that allow for the generation of the required wavelength of 2 μm by nonlinear conversion from pump pulses with a wavelength in range 900-1200 nm. Laser technology in this wavelength range is more developed than in the range of 2 μm , with high-energy nanosecond pulsed lasers of Nd:YAG or Yb:YAG frequently used in industrial applications. Moreover, the previous laser spectroscopy experiments of the CREMA collaboration in muonic atoms utilized a Yb:YAG thin-disk laser with a wavelength of 1030 nm that generated 80 mJ of pulses at an average repetition rate of 200 s⁻¹. This laser system however did not satisfy the single-frequency requirement calling for a complete re-design of the laser system. We opt to pursue a similar approach utilizing a Yb:YAG thin-disk laser that generates pulses of wavelength 1030 nm of duration 50 ns. These pulses of wavelength 1030 nm can then be downconverted to a wavelength near 2 μm by difference frequency generation using PPLNB or PPKTP.

As Eq. 2.41 indicates that the nonlinear process is enhanced for the quasi-degenerate wavelength choice, i.e, when $\lambda_S = \lambda_I = 2\lambda_P$ ($\delta=0$), ideally we would like to choose $\lambda_S = \lambda_I = 2060$ nm given the pump wavelength of 1030 nm. However, the ZGP crystal, although mostly transparent for wavelengths near 2 μm , is partially absorptive as shown in Fig. 2.9, making nonlinear conversion at 2060 nm difficult. Moreover, we would ideally like to choose a signal frequency for which a laser is commercially available, as this allows us to facilitate the nonlinear conversion process and provide a stable and known frequency for the idler, a major prerequisite for laser spectroscopy. To balance these criteria, we opt for $\lambda_S = 1979$ nm and $\lambda_I = 2149$ nm.

As the wavelength of the pump pulses in the ZGP-based 6.8 μm -DFG stage has been fixed to be 2.1 μm , the wavelength of signal pulses must be tunable around ~ 3143 nm. Table 2.1 indicates that PPLNB or PPKTP are transparent for 3143 nm. Thus, these pulses can be generated by downconversion of the 1030 nm pulses from the thin-disk laser. For this DFG process, given the wavelength of the idler to be 3143 nm, we can determine the wavelength of the signal photons to be 1532 nm.

Note that the established layout featuring a two-stage difference frequency generation

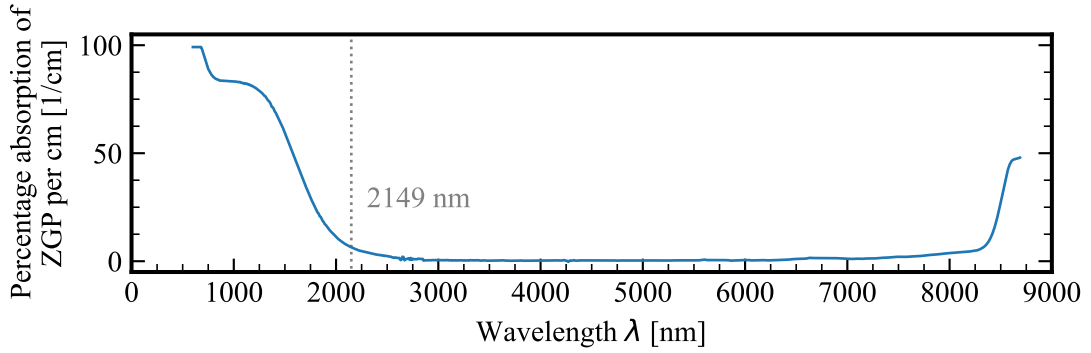


Figure 2.9: Absorption spectrum of a ZGP crystal of length 1 cm. At the wavelength of 2149 nm, the absorption is $\sim 4\%$, compared to the $\sim 10\%$ absorption at 2060 nm

scheme implies that the frequency of the $6.8\ \mu\text{m}$ is independent of the frequency of the $1030\ \text{nm}$ (discussed in Sec.2.3.4). For scanning the wavelength of the $6.8\ \mu\text{m}$ pulses across the search range of $6798\ \text{nm} - 6785\ \text{nm}$, at least one of the wavelengths that participate in the difference frequency generation stages ($1979\ \text{nm}$, $2149\ \text{nm}$, $1532\ \text{nm}$ or $3143\ \text{nm}$) must be tunable. Among these wavelengths, $1532\ \text{nm}$ lies in the telecom band. Optical technology in this wavelength range is well-developed, with stable, widely tunable single-frequency narrow-band lasers commercially available. Thus, we opt to design the laser system such that the wavelength of the $6.8\ \mu\text{m}$ can be tuned by tuning the wavelength of the $1532\ \text{nm}$ while stabilizing the wavelengths $1979\ \text{nm}$, $2149\ \text{nm}$ and $3143\ \text{nm}$ for the spectroscopy campaign.

Energy requirements and constraints

The energy of the idler $6.8\ \mu\text{m}$ pulses is determined by the energy of the input pump $2.1\ \mu\text{m}$ and signal $3.1\ \mu\text{m}$ pulses. The energy of the latter two pulses is dependent on the energy of the input pump $1030\ \text{nm}$ pulses, and that of the signal pulses in each case. Ultimately, the maximum possible energy of the $6.8\ \mu\text{m}$ pulses is determined by the available energy of the $1030\ \text{nm}$ pulses and the conversion efficiency of each nonlinear process. To determine the total energy of the $1030\ \text{nm}$ pulses needed, commercial proprietary software *SNLO* that allows for numerical evaluation of Eq.2.22 by the finite-element method is used. Fig.2.10-a) shows the variation of the energy of the $6.8\ \mu\text{m}$ pulses with that of the $2.1\ \mu\text{m}$ pulses for two energies of $3.1\ \mu\text{m}$ pulses in a ZGP crystal of dimensions $12 \times 12 \times 10\ \text{mm}$ under ideal phase-matching condition ($\Delta k = 0$), assuming the nonlinear coefficient to be $d_{\text{eff}} = 75\ \text{pm/V}$ and the Beer-Lambert absorption coefficient of $\sim 0.066\ \text{cm}^{-1}$ at $2.1\ \mu\text{m}$. The simulation considers Type-I phase-matching with walk-off angles of $\theta_w = 12\ \text{mrad}$ for the $6.8\ \mu\text{m}$ and $3.1\ \mu\text{m}$ pulses (design set such that $2.1\ \mu\text{m}$ sees no walk-off), pulse durations of FWHM $\tau_p = 50\ \text{ns}$ and Gaussian beams with beam waist of $w_0 = 550\ \mu\text{m}$ (corresponding to minimum possible waist for $27\ \text{mJ}$ of input energy due to the damage threshold limit) with the waist positions at the centre of the crystal.

The energy requirements must be set conservatively as Fig.2.10-a) ignores information on the beam quality M^2 . Significant deterioration in the beam quality is to be expected due to the walk-off of the $6.8\ \mu\text{m}$ and $3.1\ \mu\text{m}$ pulses from the $2.1\ \mu\text{m}$ pulse. Furthermore, as the laser system is based on a two-stage nonlinear stage starting with the conversion of pulses of $1030\ \text{nm}$ from the TDO, deterioration in the beam quality with each stage as well as shortening of the pulse duration (thereby a reduction in conversion efficiency)

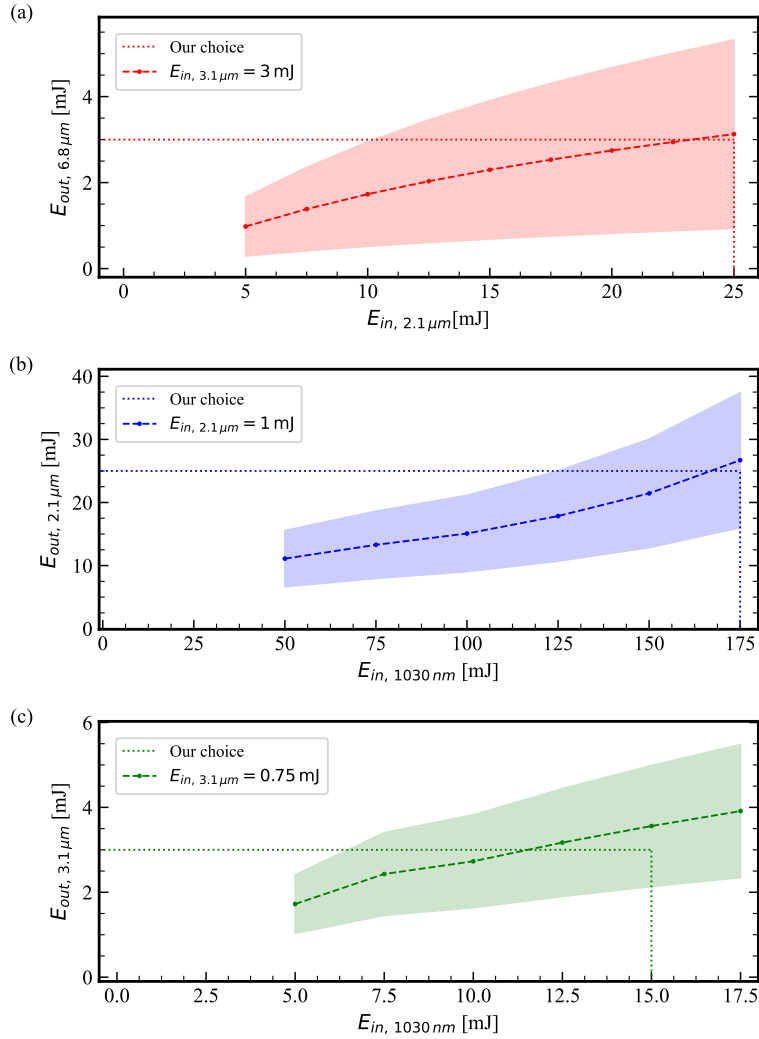


Figure 2.10: Results from SNLO simulations (a) the output energy of 6.8 μm pulses with the input energy of 2.1 μm pulses in ZGP of length 10 mm, assuming $d_{eff}=75$ pm/V and beam waist $w_0=550$ μm (b) the output energy of 2.1 μm pulses with the input energy of 1030 nm pulses in PPKTP crystal of 12 mm length, $d_{eff}=9.33$ pm/V and beam waists $w_0=240$ μm . (c) the output energy of 3.1 μm pulses with the input energy of 1030 nm pulses in MgO:PPLNB crystal of 14 mm length and beam waists $w_0=587$ μm . In each case, we assume pulse duration $\tau_p=50$ ns, equal beam waists for all three beams, $M^2=1$, ideal phase-matching and that the position beam waist is at the centre of the crystal. The shaded region indicates $\pm 40\%$ tolerance level for the simulation that accounts for deviations from ideal beam characteristics, reduction in efficiency due to imperfections in crystal and room for optimization for (b) and (c). Since the 6.8 μm pulses suffer absorption losses due to atmospheric H_2O , the tolerance limit is extended to $\pm 70\%$ for (a). Shown in grey is our choice for the operating point.

and propagation losses are to be expected. The higher the M^2 of the 6.8 μm pulse is determined to be, the more must be the energy to obtain the same fluence distribution with the toroidal enhancement cell for excitation of μH . Furthermore, imperfections in the nonlinear crystal can lead to a lower d_{eff} . We assume that the energy requirements must be tolerant up to $\sim \pm 40\%$ to account for these effects and room for optimization of the beam waist and pulse duration. Additionally, since the H_2O molecules within the atmosphere can absorb 6.8 μm wavelength, we extend the tolerance limit to 70%. Thus we determine that to generate 3 mJ of 6.8 μm pulses, we must first generate 25 mJ of 2.1 μm pulses and 3 mJ of 3.1 μm pulses.

To generate single-frequency high-energy pulses of 2.1 μm and 3.1 μm with beam quality $M^2 \sim 1$, we follow the well-established *master oscillator power amplifier* (MOPA) scheme where a preliminary low-energy single-frequency pulse of excellent beam quality is generated in an OPO (optical parametric oscillator), followed by its amplification in an OPA (optical parametric amplifier). This distributes the total energy between two branches, bringing the operating regime of the whole system farther away from the damage threshold limit imposed by the nonlinear crystal. The single-frequency operation of each branch can then be ensured by injection-seeding of the OPO cavity with the CW laser light at the signal wavelength and Pound-Drever-Hall stabilization of the cavity to the signal wavelength (See Chapter 3).

To generate 25 mJ pulses of 2.1 μm , we must downconvert 1030 nm pulses through the PPLNB or PPKTP crystals. The PPLNB has a higher figure-of-merit, while PPKTP has a higher damage threshold. The commercial availability of PPKTP crystals with large apertures is currently limited, while PPLNB is well-tested in multiple similar OPO schemes. Thus, PPLNB is suitable for highly efficient nonlinear conversion in the low-energy regime, such as in the OPO, whereas the PPKTP is needed in the OPA as we expect a larger energy budget for amplification to high energy. We opt to pursue the generation of 2.1 μm pulses of energy 1 mJ from 5 mJ of 1030 nm pulses in an injection-seeded PDH-stabilized OPO cavity where the nonlinear process is facilitated by the PPLNB crystal and the CW intracavity 1979 nm-seed laser photons. Fig.2.10-b) shows the simulation of output energy of 2.1 μm pulses with input energy of 1030 nm pulses in a single-pass OPA in PPKTP crystal of length 12 mm under ideal phase matching conditions. The simulation assumes an input energy of 1 mJ for the 2.1 μm pulses into the OPA and that the Gaussian beam waists of all the three beams are 240 μm . Once again, we assume a 40% tolerance is needed, as indicated by the shaded region. We see that to obtain 25 mJ of 2.1 μm pulses, we must have 1030 nm pulses of energy ~ 175 mJ of when input energy of 2.1 μm pulses is 1 mJ. Subsequently, a PPKTP-based OPA must amplify the 2.1 μm pulses to the energy of 25 mJ using 175 mJ of 1030 nm pulses.

Similar to the 2.1 μm -branch, the 3.1 μm -branch begins with an OPO that is PDH stabilized to the injection-seeded CW photons of wavelength 1532 nm-seed laser. The lower energy requirement of the 3.1 μm -branch makes PPLNB a better choice for both the OPO and the OPA. Figure 2.10-c) shows the variation of the energy of the 3.1 μm pulses with the input energy of 1030 nm pulses for a PPLNB crystal of 14 mm length as well as the $\pm 40\%$ tolerance region. The simulation assumes an input energy of 0.75 mJ for the 3.1 μm pulses into the OPA and that the Gaussian beam waists of all the three beams are 587 μm . This indicates that 20 mJ of 1030 nm pulses are needed to obtain 3 mJ of 3.1 μm . To this end, we aim to generate 0.75 mJ of 3.1 μm pulses from 5 mJ of 1030 nm pulses with the 3.1 μm -OPO, followed by their amplification to 3 mJ with 15 mJ of 1030 nm pulses in the 3.1 μm -OPA.

Considering the tolerance level of $\pm 40\%$, this brings the total energy of 1030 nm pulses

needed to be between 117 mJ and 273 mJ, with an average value of 195 mJ. Similar to the nonlinear stages, we opt for 1030 nm-branch features a MOPA layout. The 1030 nm pulses of duration 50 ns are generated in an injection-seeded PDH-stabilized thin-disk laser by the method of cavity dumping. The pulses are then amplified by a multipass thin-disk amplifier to energies of 150 – 300 mJ. The layout of the chosen scheme is summarized in Fig:2.8. Details pertaining to the design of the 1030 nm thin-disk MOPA system and the 3.1 μm -branch are given in the doctoral dissertations [43] and [54], respectively. Below, we summarize the salient points relevant for the remainder of the thesis. Chapters 2, 3 and 4 present the design and characterization of the 2.1 μm -OPO, 2.1 μm -OPA and the 6.8 μm -DFG stage, respectively.

1030 nm *Thin Disk Oscillator-Amplifier*

The parent source of the 1030 nm photons is the thin-disk oscillator (layout shown in Fig:2.11-a). This laser gets its name from the fact that its gain medium has disk-shaped geometry. To generate population inversion for laser operation, energy levels of the gain medium are excited using a high-power continuous-wave (CW) laser, which also heats the gain medium to high temperatures. When such optical substrates are heated, they develop a curvature that acts to focus or defocus light, a phenomenon called thermal lensing, and makes their use in optical resonators challenging. The disk geometry works to ameliorate much of this unwanted heat load by confining the thermal gradient in the longitudinal direction, i.e, along the propagation direction. Further reduction in the thermal lens effect is obtained by the efficient cooling of the medium from the large surface-to-volume ratio.

The TDO features a Yb:YAG disk of thickness 500 μm and 14 mm diameter with AR⁵ coating on one side and HR⁶ coating on the other for the wavelength range of 940-1080 nm. The HR-side of the disk is glued to a diamond substrate of diameter 25 mm that acts as a heat-sink due to its high thermal conductivity. The free side of the diamond heat spreader is water-cooled to reduce the temperature of the disk-diamond system and, hence, reduce the thermal lens effect. As the thickness of the disk is rather small, sufficient pump light is not absorbed in a single pass to produce enough population inversion. Thus, laser light from a CW diode laser of wavelength 969 nm and power 400 W is imaged repeatedly onto the disk in a multipass configuration based on a 4f-imaging scheme to obtain a pump spot of diameter 5.2 mm. As many of the details of optical pumping and disk laser design are beyond the scope of this thesis, the interested reader is referred to [43, 55] for the relevant simulations and technical details.

The resonator is designed to be similar to a Fourier transform resonator, in conjunction with a Galilean telescope [43]. This makes it passively stable against the effects of thermal lensing of the disk and pointing fluctuations. The pointing of the light is further stabilized with a quadrant photodetector PD_A and a commercial autoalignment system.

As shown in Fig.2.11-a), optical pulse generation is achieved by cavity dumping using the Pockels cell in conjunction with a thin-film polarizer (TFP). The Pockels cell consists of a BBO crystal (size: 10 x 10 x 20 mm), mounted onto two electrodes that are connected to a high-voltage (HV) switching circuit. The Pockels cell can be thought of as a voltage-controlled waveplate that allows us to increase or decrease the intracavity power and, hence, the outcoupling of the cavity.

During the spectroscopy campaign of μH , the signal from the entrance detector will

⁵AR: Anti-reflective coating

⁶HR: Highly-reflective coating

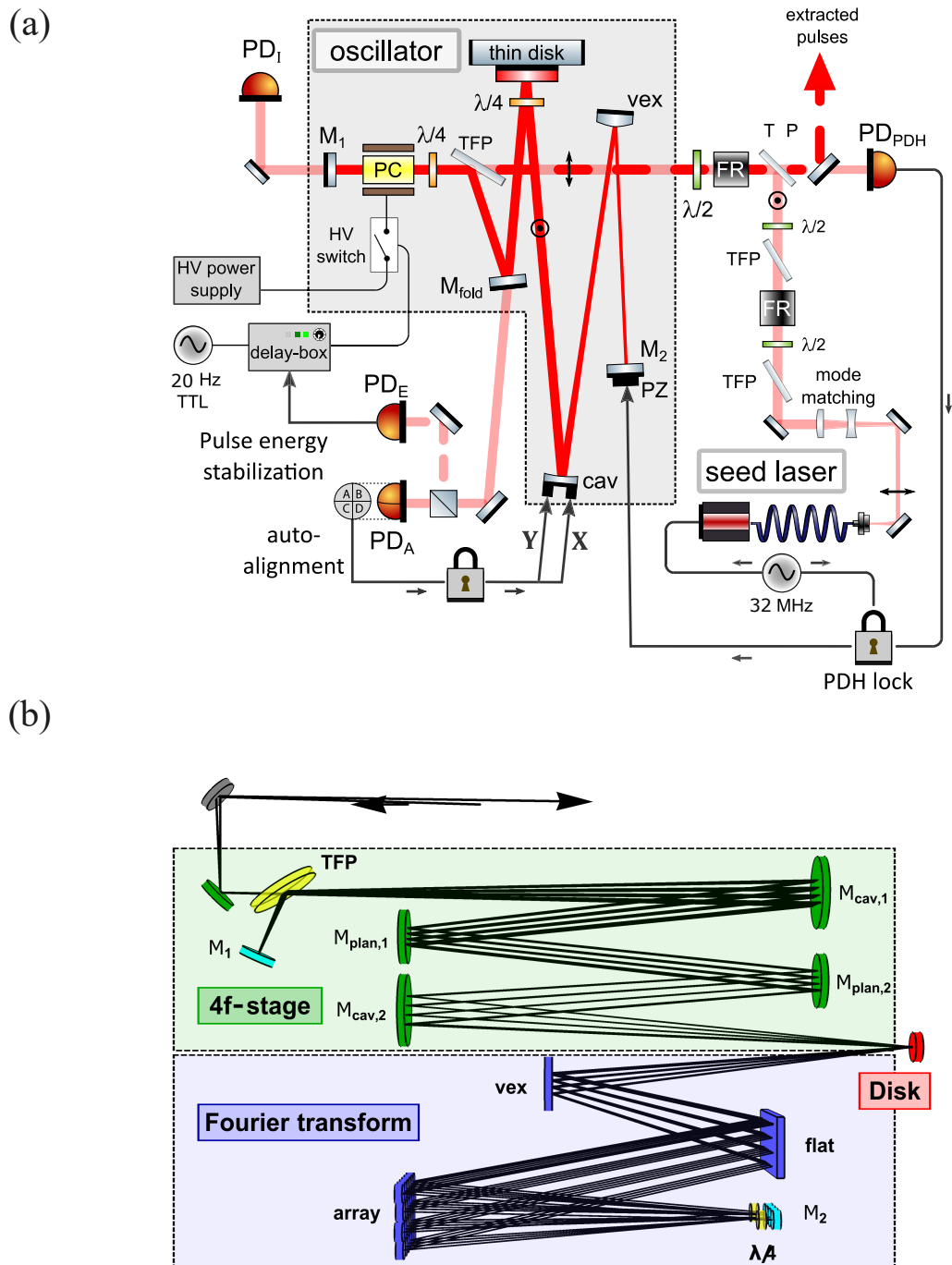


Figure 2.11: Layout of the (a) thin-disk oscillator (b) thin-disk multipass amplifier. TDO is injection-seeded and PDH stabilized. The trigger signal closes the cavity of the TDO leading to pulse that increases in energy with each round-trip. Photodiode PD_E monitors the intracavity pulse intensity. Once sufficient energy is reached, the cavity is opened to extract the pulse in the direction of the TDA or the nonlinear stage. The TDA features a 4f-stage that images the beam at mirror M_1 onto the disk and Fourier transform stage that stabilizes the beam size in each pass.

be used by the HV switching circuit to trigger the laser. For the purpose of developing the laser system, we use a TTL signal generator to provide a continuous trigger of 20 Hz as a substitute. The trigger signal leads to closing of the cavity through the action of the Pockel cell. An optical pulse that circulates within the cavity, extracting energy from the disk with each round-trip, is formed. Once sufficient energy is reached, the pulse is extracted from the cavity.

During the pulse formation period, a photodetector PD_E monitors the circulating intracavity intensity. The signal that prompts the pulse extraction is given to the switching circuit only when this photodetector current reaches a pre-set value, i.e., when the intracavity intensity reaches a set value. As every pulse that is generated from the TDO is extracted for the same set value of intracavity intensity, the energy of each extracted pulse is nearly the same, ensuring high pulse energy stability.

To ensure that the laser pulse is generated at the required wavelength, CW light of wavelength 1030 nm from a diode laser (Toptica DL Pro) of linewidth <kHz is mode-matched and injected into the TDO cavity. The cavity length of TDO is stabilized via the Pound-Drever-Hall locking scheme [56] to ensure that the injection-seeded photons are resonant in the cavity. For this purpose, injection-seeded light is phase-modulated at 32 MHz and a PDH scheme free of Trojan operating point is implemented [57]. In addition to ensuring a high frequency stability, injection seeding the optical cavity reduces the amount of time needed to generate the pulse and ensures that the latency of the TDO is <1 μ s, as needed for the μ H spectroscopy. Additionally, the emission cross-sections of the Yb:YAG gain medium is dependent on the wavelength of the light, a stable wavelength also ensures energy stability.

The 1030 nm pulses from the TDO are amplified by the thin-disk amplifier (TDA). As shown in Fig.2.11-b), the latter is a multipass system where a Yb:YAG thin-disk gain medium is pumped with a CW diode laser of power 2.4 kW and wavelength 969 nm. It is designed to amplify the 1030 nm pulses to energies of 300 mJ while preserving their transverse beam quality. To this end, a two-stage optical propagation scheme is designed - the 4f-stage that images the input 1030 nm beam into the TDA to the disk, followed by a *Fourier transform*-stage that stabilizes the beam size in each round-trip against the focal power of the disk. The propagation path of the pulse follows the sequence

$$4f - \text{disk} - FT - \text{disk} - 4f - 4f - \text{disk} - FT - \text{disk} - \dots$$

and increases in energy with each pass through the disk. The implemented scheme utilizes 20-passes through the disk, giving a total propagation length of \sim 25 m for the 1030 nm pulses. Ultimately, a mutli-pass disk amplifier capable of amplifying 30 mJ of 1030 nm pulse energy to 300 mJ has been realized. The interested reader is referred to [43, 58] for further details and relevant results.

3.1 μ m-MOPA branch

Figure 2.12 shows the optical and electronic layout of the 3.1 μ m-MOPA. Pulses of 3.1 μ m wavelength are generated in an OPO that is singly-resonant for the signal wavelength of 1.5 μ m. The cavity is injection-seeded with CW laser light of narrow linewidth from a 1532 nm-seed laser. PDH locking of the cavity to the 1532 nm-seed laser ensures that the in-coupled light from 1532 nm-seed laser is resonant within the cavity.⁷

⁷cavity length = $n \frac{\lambda_{1.5\mu\text{m}}}{2}$, where $n=1,2,3,\dots$

The 1030 nm pulses of 5 mJ energy are coupled into the cavity through the TFP. The cavity features a MgO:PPLNB of size 3x3x14 mm. Within the nonlinear crystal, 1030 nm pulses (pump) from the TDO interact with CW 1.5 μm light (signal), which is resonant in the cavity, to produce pulses the 3.1 μm (idler). The generated 3.1 μm pulses and the depleted 1030 nm pulses are transmitted out of the cavity through a dichroic mirror. These 3.1 μm pulses are successfully filtered using dichroic mirrors (HR:1030 nm, HT:3.1 μm) to remove the depleted 1030 nm pulses and propagated to the 3.1 μm -OPA. Prior to their amplification, the 3.1 μm pulses pass through lenses that optimize the size and collimation in the crystal. Here, the spatial and temporal profile of the 3.1 μm pulses are overlapped with that of the 1030 nm pulses within a MgO:PPLNB crystal of size 3x3x25 mm. The 3.1 μm pulses of 0.75 mJ energy are amplified to 3 mJ with 20 mJ pump energy of 1030 nm wavelength. Beam quality M^2 of the 3.1 μm pulses after the amplification was determined to be 1.15, indicating a nearly-Gaussian spatial profile.

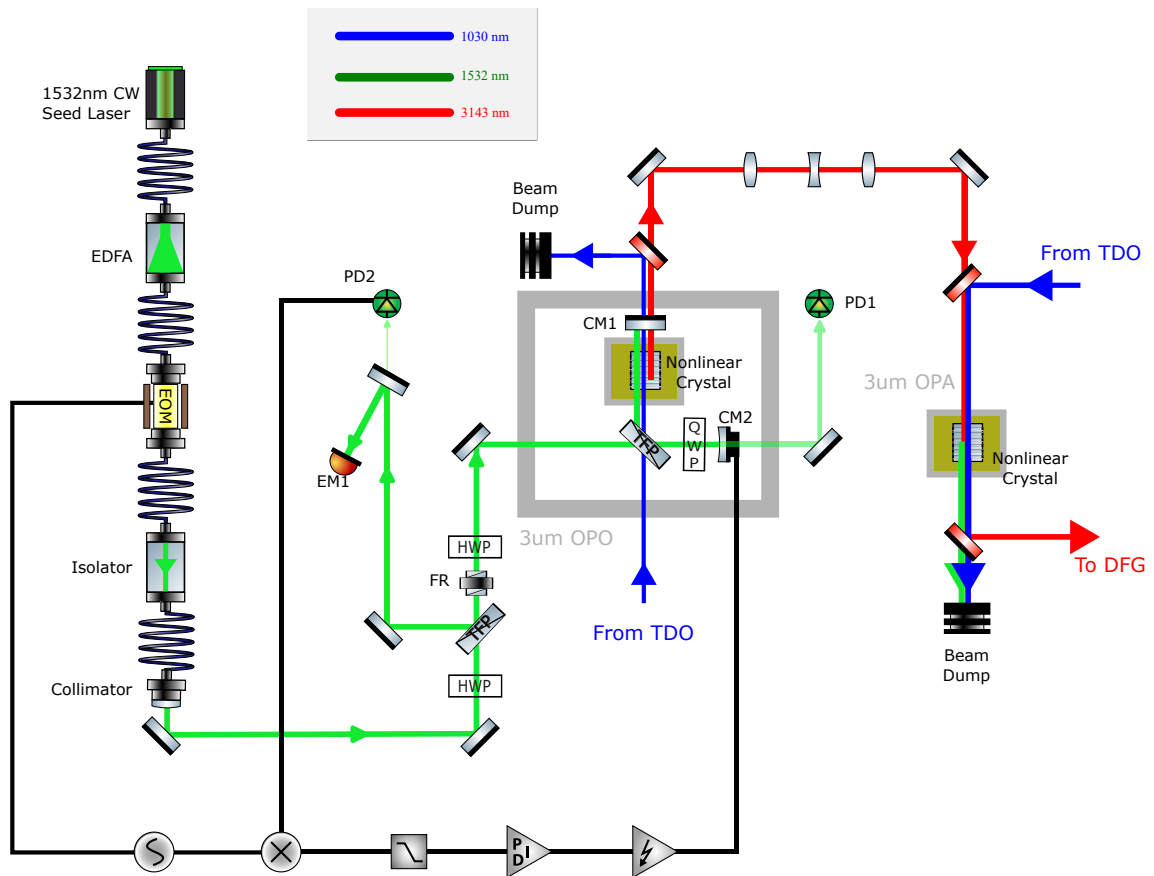


Figure 2.12: Optical and electronic layout of the 3.1 μm -MOPA. CW laser light from a diode laser (1532 nm-seed laser) is injection-seeded into the cavity of the 3.1 μm -OPO. PDH stabilization of the cavity to 1532 nm-seed laser is achieved by phase-modulation of the injected light and subsequent measurement of the reflected light from the cavity by the photodiode PD2. Pulses of wavelength 1030 nm enter the OPO cavity through the TFP and are down-converted by interaction with the nonlinear crystal MgO:PPLNB and the intracavity 1.5 μm to generate pulses of 3.1 μm wavelength. 3.1 μm pulses exit the OPO cavity through dichroic mirror CM1 and are later amplified by the 3.1 μm -OPA in a similar difference frequency generation process.

Control system for spectroscopy and frequency calibration

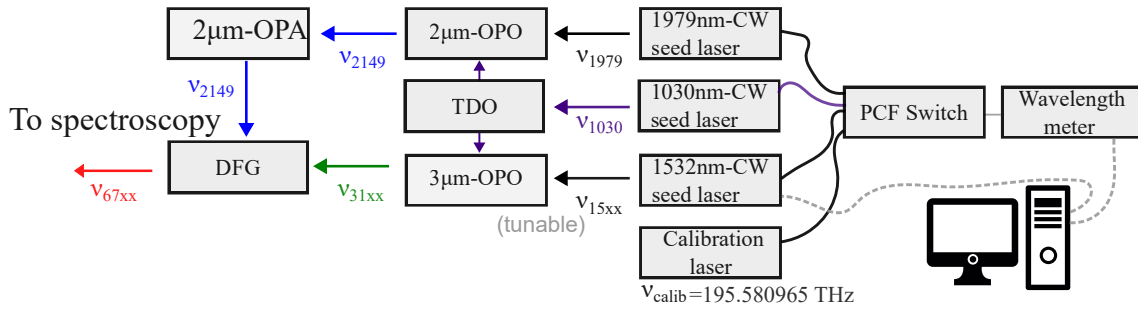


Figure 2.13: Layout of frequency control and monitoring system of laser system for spectroscopy. The solid straight arrows represent the propagation of photons in free space between different parts of the laser system. A part of the light from each of the seed lasers that injection seed the TDO, 2.1 μm and 3.1 μm -OPO are coupled into a photonic crystal fiber (PCF) switch via fiber couplers (solid curved lines). The wavelength of these lasers is measured with a wavelength meter connected to the PC. The wavelength meter is calibrated against the wavelength of a reference laser (1532.830 45 nm or 195.580 965 THz in frequency). The frequency ν_{1979} and ν_{15xx} are used to determine ν_{67xx} using eq:2.58. The 1532 nm-seed laser, that injection seeds the 3.1 μm -OPO, and the wavelength meter are controlled via the PC (dashed grey lines) so that ν_{15xx} can be varied to scan ν_{67xx} across the desired range.

Figure 2.13 shows the layout of the implemented frequency control system. The frequency of 1979 nm-seed laser and 1532 nm-seed laser are measured by a wavelength meter (WS8-30, HighFinesse) through a fiber-coupled photonic crystal fiber (PCF) switch. The manufacturer specified 3σ -confidence interval of the true wavelength with respect to the measured wavelength⁸ for the wavelength meter is 30 MHz. The wavelength meter is calibrated against a reference laser (SLR1532, HighFinesse), which is stabilized to the P(13)-line of C_2H_2 of frequency 195.580 965 THz. The frequency ν_{15xx} of the 1532 nm-seed laser is computer-controlled to vary its frequency at ν_{67xx} .

Center frequency considerations

To obtain the desired frequency in each part of the laser system with high frequency stability, the optical cavities of the TDO, 2.1 μm -OPO and 3.1 μm -OPO are stabilized via Pound-Drever-Hall locking scheme to laser light from narrow-bandwidth single-frequency diode lasers of the frequencies ν_{1030} ⁹, ν_{1979} , and ν_{15xx} ¹⁰, respectively (Sec: 2.3).

In the 2.1 μm -OPO, the photons of frequency ν_{1030} from the TDO pulses interact with the photons of frequency ν_{1979} from 1979 nm-seed laser circulating through the nonlinear crystal and are converted into photons of frequency ν_{2149} and ν_{1979} . As the bandwidth of the 1979 nm-seed laser is narrow, the frequency profile of the ν_{2149} pulses is determined by that of the ν_{1030} pulses and any variation in the phase of the ν_{1030} pulses is transferred to the phase of the ν_{2149} pulses. The centre frequency of the ν_{2149} pulse is uniquely deter-

⁸Frequency range about the measured wavelength over which the probability of finding the true wavelength is 99.73 %

⁹The index denotes the wavelength of the laser in nm: e.g., here 1030 nm

¹⁰'xx' in the index indicates that the wavelength can be tuned

mined by the difference between the centre frequency of the ν_{1030} pulse and the frequency of the ν_{1979} laser, $\nu_{2149} = \nu_{1030} - \nu_{1979}$.

When the pulses from the 2.1 μm -OPO are amplified by the 2.1 μm -OPA, the frequency profile of the pulses is expected to be preserved in the amplification as the frequencies of the 2.1 μm and the 1030 nm pulses are fixed. As detailed in Chapter 4 and in Fig.2.8, the pulses from 2.1 μm -OPA interact with pulses of frequency ν_{31xx} from the 3.1 μm -OPO in a DFG stage to produce pulses of frequency ν_{67xx} .

The 3.1 μm -OPO is injection-seeded with photons of frequency ν_{15xx} from 1532 nm-seed laser that can be set to a value between 195.4 THz to 195.7 THz. The photons of frequency ν_{1030} and ν_{15xx} interact, and the ν_{1030} -pulse is converted into pulses of frequency ν_{15xx} and ν_{31xx} so that $\nu_{31xx} = \nu_{1030} - \nu_{15xx}$. Thus, the frequency ν_{31xx} of the pulse from 3.1 μm -OPO can be tuned by varying ν_{15xx} .

Ultimately, the centre frequency of the ν_{67xx} is uniquely determined from the frequencies of the seed-lasers: ν_{1979} and ν_{15xx} :

$$\nu_{67xx} = \nu_{2149} - \nu_{31xx} \quad (2.56)$$

$$= (\nu_{1030} - \nu_{1979}) - (\nu_{1030} - \nu_{15xx}) \quad (2.57)$$

$$= \nu_{15xx} - \nu_{1979} \quad (2.58)$$

Interestingly, the frequency ν_{67xx} of the 6.8 μm pulses does not depend on the frequency ν_{1030} of the pulses from the TDO. Thus, any fluctuation in the frequency of the TDO pulses does not affect the frequency of the 6.8 μm pulses. Nonetheless, injection-seeding of the TDO allows for better energy and frequency stability for the laser system.

2.4 CONCLUSION

To satisfy the stringent requirements of the laser system for μH spectroscopy, a multi-stage laser system based on nonlinear downconversion is realized. High energy pulses of wavelength 1030 nm and duration 50 ns are generated in a thin-disk oscillator. These pulses of 30 mJ energy are amplified to >200 mJ energy in a multi-pass thin disk amplifier. These 1030 nm pulses are downconverted into pulses of wavelength 2.1 μm and 3.1 μm in two separate parallel branches of the laser system. The 3.1 μm pulses are generated by downconversion of 1030 nm pulses on interaction with CW intracavity 1.5 μm , facilitated by the nonlinear crystal MgO:PPLNB in the singly-resonant injection-seeded 3.1 μm -OPO. 0.75 mJ of 3.1 μm pulses with $M^2 \sim 1.1$ are generated from 5 mJ of 1030 nm pulses. These pulses are further amplified to energies of 3 mJ with 15 mJ of 1030 nm pulses with the nonlinear crystal MgO:PPLNB in the 3.1 μm -OPA. Post-amplification, the pulses still remain nearly Gaussian with $M^2 \sim 1.3$.

Pulses of 2.1 μm wavelength and 1 mJ energy are generated in the singly-resonant injection-seeded 2.1 μm -OPO by the nonlinear interaction of the 1030 nm pulses and the CW intracavity 1.9 μm , mediated by a MgO:PPLNB nonlinear crystal. Amplification of these 2.1 μm pulses is achieved in the 2.1 μm -OPA with 175 mJ of 1030 nm pulse, mediated by the crystal PPKTP, to obtain energies of 25 mJ. The 25 mJ of 2.1 μm and 3 mJ of 3.1 μm pulses so generated interact in the nonlinear crystal ZGP to generate 3 mJ of 6.8 μm . The implementation of the 2.1 μm -MOPA and 6.8 μm -DFG stage and the subsequent characterization of the frequency profile are the subjects of this thesis.

The nonlinear downconversion stage to generate pulses of wavelength 6.8 μm involves 5 different wavelengths -1030 nm, 3.1 μm , 2.1 μm , 1.5 μm and 1.9 μm . By allowing 1.5 μm

to be varied and stabilizing all other wavelengths, the frequency of the 6.8 μm pulses can be scanned across the resonance of the 1S HFS in μH . Injection-seeding and PDH stabilization of the TDO, 3.1 μm -OPO and 2.1 μm -OPO ensures high frequency stability and single-frequency operation.

2.1 μM -VARIABLE FINESSE OPTICAL PARAMETRIC OSCILLATOR

This chapter describes the design of the 2.1 μm -OPO (Fig.3.1) that downconverts the 1030 nm pulses into 2.1 μm and 1.9 μm pulses via difference frequency generation in a singly resonant cavity. The OPO cavity (Fig.3.1) consists of a thin film polarizer (TFP), a quarter waveplate (QWP), a highly-reflective (HR) plane mirror and a curved mirror. The intracavity TFP reflects only s-polarized light. The fraction of s-polarized light that is rotated to p-polarized light in each round trip, and hence lost, depends on the orientation of the fast axis of the intracavity QWP. This allows the intracavity power and the finesse of the OPO cavity to be controlled by the QWP. As such, a variable-finesse cavity, capable of operating at different intracavity intensity, is realized.

In essence, the salient features of the OPO are :

- A tunable-finesse singly-resonant OPO at the signal wavelength of 1.9 μm
- Pound-Drever-Hall stabilization scheme of the cavity to the seed laser with infinite-capture range for excellent frequency and energy stability
- Output idler pulses of wavelength 2.1 μm and energy ~ 1 mJ for an input pump pulse energy of 5 mJ of duration 50 ns at the wavelength of 1030 nm, corresponding to conversion efficiency of 50 %
- A beam quality of $M_M^2 = 1.28$ and $M_m^2 = 1.12$ along the major and minor axis of the beam, respectively.

3.1 TECHNICAL IMPLEMENTATION

The CW laser light from 1979 nm-seed laser is phase-modulated (at frequency 665 MHz) using an electro-optical modulator (EOM) and amplified with a thulium-doped fiber amplifier (TDFA) to 50 mW power. This CW light from the fiber optics system is mode-matched to the OPO cavity through a collimator (focal length 7.5 mm). An optical isolator (I1950P4, Thorlabs) ensures that the sensitive fiber optics is well-protected from the light reflected by the cavity.

The cavity consists of a planoconcave mirror M4 ($R_c = 500$ mm), a dichroic mirror M5 ($R > 99.9\%$ at 1.9 μm , $T > 0.5\%$ at 1030 nm), a thin film polarizer (131823, Layertec), a quarter waveplate (QWP) and the nonlinear crystal (MgO-doped. PPLNB, dimension: 3 x 3 x 14 mm, poling period $\Lambda = 31.3$ μm). The poling period was determined from Eq.2.52 using the commercial software SNLO. The nonlinear crystal is housed in an oven for temperature control. The planoconcave mirror M4 is attached to a piezo-electric transducer (PZT) so that the cavity length can be electronically controlled. Light is coupled into the cavity from the seed laser system through the polarizer. The leaking 1.9 μm light through the mirror M4 is measured by photodetector PD1 to monitor the cavity profile. Figure 3.2

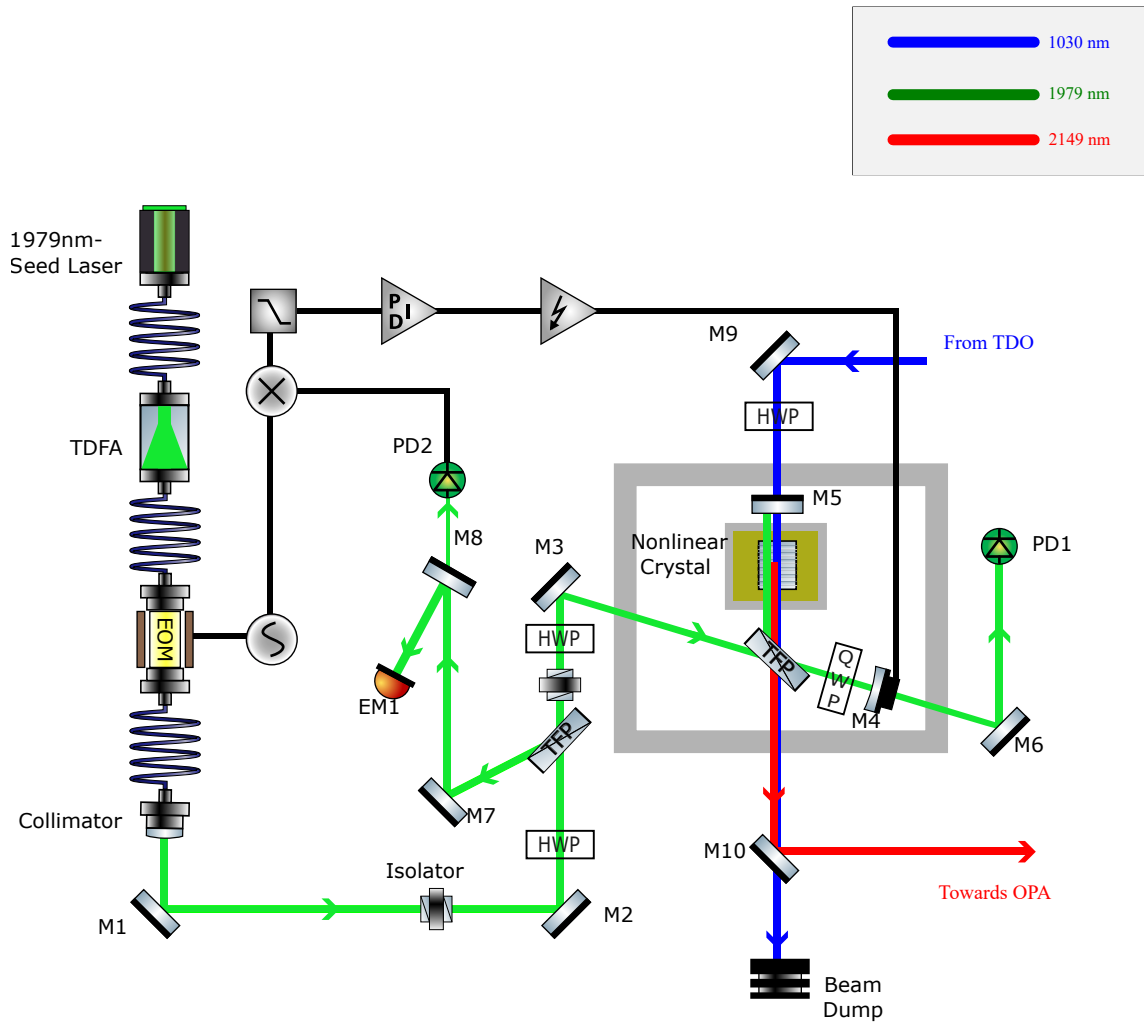


Figure 3.1: Optical and electronic layout of the singly resonant injection-seeded PDH-locked OPO Cavity. After amplification by a fiber amplifier (TDFA) and modulation by an EOM, CW-1.9 μm from a single-frequency diode laser and injection seeded into the OPO Cavity. The light in the cavity is purely s-polarized as the thin film polarizer transmits the p-polarization. The beat note between the light reflected from the cavity and the light which does not enter the cavity is used for Pound-Drever-Hall locking. The feedback from the PID is supplied to the piezoelectric transducer attached to the curved cavity mirror.

shows the variation of the Gaussian beam diameter $2w(z)$ of the cavity mode. Within the 14 mm length of the nonlinear crystal, the beam remains collimated to a beam waist of $350\ \mu\text{m}$.

The part of the injection-seeded light reflected by the cavity propagates through a Faraday rotator (FR) and is, hence, reflected by the polarizer TFP2. The photodetector PD2 uses the leakage of this CW light through a mirror for PDH stabilization of the cavity to the $1979\ \text{nm}$ -seed laser. After demodulation with an RF mixer, the DC component of the photodiode signal is extracted with a low-pass filter. This signal is utilized by a PID controller to stabilize the length of the cavity such that the injection-seeded $1.9\ \mu\text{m}$ laser light is resonant in the cavity.

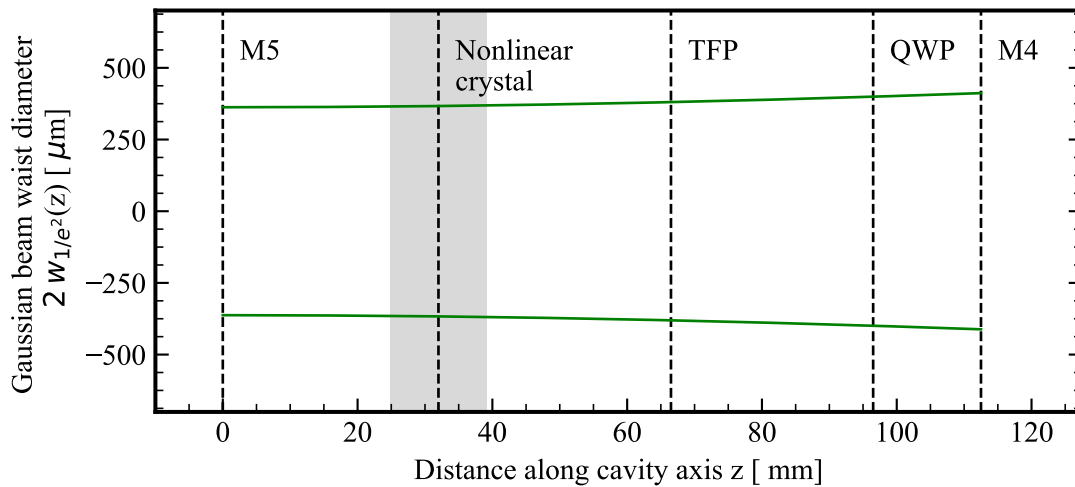


Figure 3.2: Mode diameter of signal at $1.9\ \mu\text{m}$ along the cavity axis. The shaded region of width 14 mm corresponds to the nonlinear crystal.

The $1030\ \text{nm}$ pulses from the TDO enter the cavity through the dichroic mirror M5 and are overlapped with the CW- $1.9\ \mu\text{m}$ intracavity field. Under optimum phase-matching, the $1030\ \text{nm}$ pulses are downconverted by the nonlinear crystal to generate $2.1\ \mu\text{m}$ pulses and $1.9\ \mu\text{m}$ pulses. The $1.9\ \mu\text{m}$ pulse is reflected from the cavity in the direction of the PDH stabilization segment and monitored by energy meter EM1. The generated $2.1\ \mu\text{m}$ pulses and the depleted $1030\ \text{nm}$ pulses are transmitted through the TFP. Dichroic mirror M10 separates the $2.1\ \mu\text{m}$ pulses from the $1030\ \text{nm}$ pulses, which is sent to a beam dump. The $2.1\ \mu\text{m}$ pulses propagate to the $2.1\ \mu\text{m}$ -OPA.

3.2 VARIABLE FINESSE SINGLY-RESONANT CAVITY DESIGN

Injection-seeding and cavity layout

Relevant to us are two possible OPO cavity designs - the singly-resonant OPO design and the doubly-resonant OPO design. In a doubly-resonant OPO cavity, two of the three frequencies that participate in the nonlinear DFG process within the crystal - the signal and the idler- are resonant and allowed to circulate in the OPO cavity. In contrast, a singly resonant OPO allows either the signal or the idler to be resonant. For brevity of discussion, we consider the SRO design where the signal is resonant and that the angular frequency ω_p of the pump is fixed. Fig.3.3 shows the diagrammatic representation of the

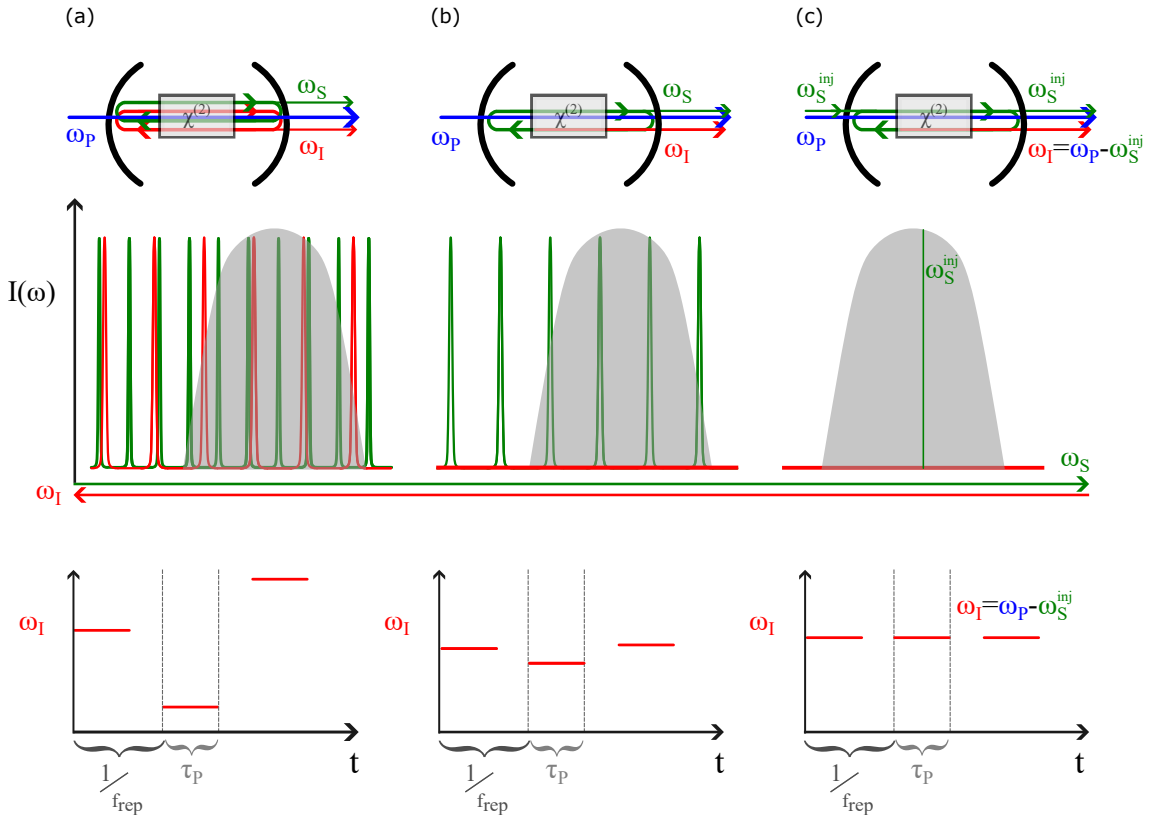


Figure 3.3: Optical layout, the intracavity spectral profile and the expected behaviour of the frequency of the 2.1 μm (idler) pulse with time is shown for (a)doubly-resonant OPO (b)singly-resonant OPO (c) singly-resonant OPO with injection seeding at ω_S^{inj} . The intracavity profile of the idler ω_I and the signal ω_S are overlaid on top of one another such that at any point in the plot, they form a combination that satisfies the energy conservation relation $\omega_P = \omega_I + \omega_S$. The phase-matching region is generally broad compared to the free spectral range of the cavity (grey) and includes several modes. The relevant time scales - the pulse duration τ_P of the 1030 nm pump pulse and the time between the pulses $1/f_{rep}$, where f_{rep} is the repetition rate is marker in each case.

OPO cavity and relevant plots for this discussion. These two designs differ in two key aspects - the conversion efficiency and the cavity mode structure.

The doubly-resonant OPO allows the circulation of the idler in addition to the signal, thereby increasing the circulating power. The higher circulating power in the doubly-resonant OPO drives the DFG process more efficiently for the same pump energy as compared to the singly-resonant design. However, the high intensity of the intracavity field implies that the operating point of the doubly-resonant OPO is much closer to the damage threshold regime of its optical components.

The mode structure of an OPO cavity is described by an Airy profile (or approximately a Lorentz profile) with maximum values at the resonant signal frequencies that are evenly spaced by the free spectral range $\delta\nu_{FSR}$ of the cavity. In the doubly-resonant OPO, the cavity mode structure also includes the idler frequencies. Note that in Fig.3.3, both the idler (red) and the signal (green) mode structures are overlaid on top of one another in the criteria that satisfies the energy conservation relation $\omega_P = \omega_S + \omega_I$. The shaded gray region represents the phase-matching region and is typically broad and encom-

passes several cavity modes. Given a given combination of idler and signal frequencies (ω_I^0, ω_S^0) that satisfies the energy conservation relations and is phase-matched, the set of combinations $(\omega_I^0 \pm \delta\omega, \omega_S^0 \mp \delta\omega), (\omega_I^0 \pm 2\delta\omega, \omega_S^0 \mp 2\delta\omega), \dots$ are also possible. During OPO operation, any of the modes ω_S within the phase-matching region can be amplified, with the mode that is closest to the peak having the largest amplification. Thus the frequency of the signal pulses, and hence the frequency of the corresponding idler pulse $\omega_I = \omega_P - \omega_S$, that is generated is different from one pulse to next. In the doubly-resonant OPO, neither of the combinations are close to the peak in the phase-matching region. Additionally, both the signal and the idler frequencies have to satisfy the resonance condition set by the cavity $\omega_S = N\pi c/2L_{cav}$ and $\omega_I = N'\pi c/2L_{cav}$ (where N and N' are integers.) Thus any external perturbations on the OPO that affect the cavity length L_{cav} can more easily lead to mode-hopping. This effect is considerably less visible in the singly-resonant OPO as only the signal frequency needs to satisfy the resonance condition $\omega_S = N\pi c/2L_{cav}$. Calculations pertaining to the proof of this effect is described in [50]. Thus, to have a higher damage threshold and to ensure that the frequency of the idler is less prone to external fluctuations, we opt to pursue a singly-resonant cavity design.

However, even the singly-resonant OPO does not give the desired idler frequency. One method to ensure that the same signal frequency undergoes amplification is to populate the cavity with a CW-laser light of the desired signal frequency ω_S^{inj} . This technique, called *injection seeding*, ensures that the generated idler frequency is fixed such that $\omega_I = \omega_P - \omega_S^{inj}$, for a stable pump frequency ω_P . It is ideal to choose a laser of linewidth that is narrower than the linewidth of the cavity mode to act as the seed laser for maximum power transfer into the cavity. For this purpose, we seed the singly-resonant OPO cavity with a diode laser of frequency 151.436 90(1) THz (wavelength 1979.6520(1) nm) as shown in Fig.3.1. The injection-seeded frequency ω_S^{inj} is made to be always resonant in the cavity via Pound-Drever-Hall stabilization (see Sec.3.2.5) by tuning the cavity length.

Note that in the case of doubly-resonant OPO, one must have injection-seed and implement PDH stabilization for both the idler and the signal frequencies to ensure single-frequency operation. Such a scheme is technically complicated and suffers from a very narrow operation point as the phase-matching condition $\omega_P = \omega_S + \omega_I$ does not leave a single degree of freedom when $\omega_P, \omega_S, \omega_I$ are fixed.

Variable-finesse cavity

Fig.3.4 shows the change in polarization of the injection-seeded CW laser light from the 1979 nm-seed laser in one round-trip of the cavity through the TFP. In the first segment of the round-trip, the p-polarized CW 1.9 μm laser enters the cavity through the TFP light and passes through the quarter waveplate. The QWP rotates the p-polarized light into an elliptical polarization depending on the angle of orientation θ of the fast-axis of the QWP.

The elliptically polarized light is transmitted by the QWP to the first cavity mirror, only to be reflected to the QWP in the second round-trip segment, where it once again rotated. Thus, in the first two segments of the cavity-round trip in the TFP-QWP-cavity mirror assembly, p-polarized light is converted to elliptically polarized light, having some amount of s-polarization¹. The amount of power converted to s-polarization solely depends on the orientation θ of the QWP.

In the third segment, this elliptically polarized light is separated into the s-polarization,

¹Elliptical polarization is a linear combination of the linear s- and p-polarization states of light with appropriate phase difference

which is reflected into the second cavity mirror, and p-polarization, which is transmitted through the cavity in the direction of the CW laser light from 1979 nm-seed laser. The s-polarized segment completes a round-trip in the cavity after reflection by the second cavity mirror and another reflection by the TFP.

Thus, the circulating power in the cavity is dependent on the fraction of light converted from p-polarization to s-polarization by the QWP. This implies that intracavity power and, hence, the finesse of the cavity can be varied by tuning the orientation of the QWP θ .

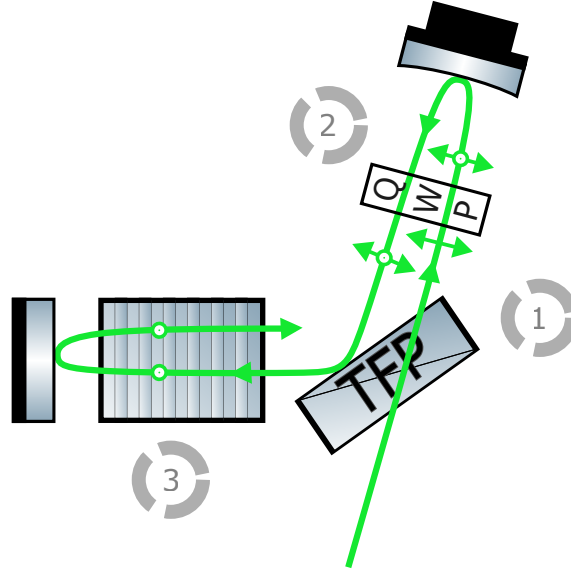


Figure 3.4: Intracavity polarization variation in the OPO cavity. Symbols: \odot : s-polarization, \updownarrow : p-polarization. Input light through the TFP is p-polarized. It is rotated into an elliptically polarized state by two passes through the QWP during the first round trip. The s-polarized fraction of this light is projected into the nonlinear crystal and curved mirror M4. The curved mirror M4 focuses this s-polarized beam to mirror M5 after reflection by the TFP.

Jones matrices

To mathematically understand the 'tunable-finesse' feature of the cavity design, we use Jones matrix formalism to model the effect of optical components of the cavity on the polarization of the intracavity beam. In this formalism, a set of basis vectors $\{\hat{e}_p, \hat{e}_s\}$, where $\hat{e}_s=(0,1)$ denotes s-polarization (polarization normal to the plane of incidence) and $\hat{e}_p=(1,0)$ denotes p-polarization (polarization parallel to the plane of incidence and normal to \hat{e}_s).² Accordingly, the electric field of an arbitrary polarization can be described is represented by

$$\vec{E}_{in} = \begin{pmatrix} E_p^{in} e^{i\phi_p} \\ E_s^{in} e^{i\phi_s} \end{pmatrix}, \quad (3.1)$$

where E_p^{in} and ϕ_p are the amplitude and the phase of the field along \hat{e}_p . A similar definition follows for s-polarization. Given an optical component, we can assign a 2×2

²Unless stated otherwise, the optical components involved in the laser system have their plane of incidence parallel to the optical table. This means that the polarization normal to the optical table is s-polarized while along parallel to the table is p-polarized.

matrix M , commonly referred to as the Jones matrix, such that the polarization of light transmitted through the matrix \vec{E}_{out} is given by

$$\vec{E}_{\text{out}} = M \cdot \vec{E}_{\text{in}} \quad (3.2)$$

Given a series of three optical components, with Jones matrices M_1, M_2 and M_3 , the field after the final element \vec{E}_{out} in the series is obtained by determining the field after the i^{th} element $\vec{E}_{i,\text{out}} = M_i \cdot \vec{E}_{i-1}$

$$\vec{E}_{\text{out}} = M_3 \cdot \vec{E}_{2,\text{out}} = M_3 \cdot M_2 \cdot \vec{E}_1 = M_3 \cdot M_2 \cdot M_1 \cdot \vec{E}_{\text{in}} \quad (3.3)$$

Thus, in this formalism, the resultant field from a series of N number of optical elements, where the Jones matrix of i^{th} element is M_i , is obtained by the matrix multiplication of the Jones matrix of each element in the order in which they appear

$$\vec{E}_{\text{out}} = M_N M_{N-1} \dots M_1 \vec{E}_{\text{in}} \quad (3.4)$$

Here, we note the Jones matrix for each relevant component of the OPO cavity as follows:

$$M_{\text{TFP,refl}} = \begin{pmatrix} 0 & 0 \\ 0 & 1 \end{pmatrix}, M_{\text{mir}} = \begin{pmatrix} 1 & 0 \\ 0 & -1 \end{pmatrix}, M_{\text{crystal}} = \begin{pmatrix} 1 & 0 \\ 0 & 1 \end{pmatrix} \quad (3.5)$$

and

$$M_{\text{QWP}}(\theta) = e^{i\frac{\pi}{4}} \begin{pmatrix} \cos^2(\theta) + i \sin^2(\theta) & (1-i) \sin(\theta) \cos(\theta) \\ (1-i) \sin(\theta) \cos(\theta) & \sin^2(\theta) + i \cos^2(\theta) \end{pmatrix} \quad (3.6)$$

where $M_{\text{TFP,refl}}, M_{\text{mirror}}, M_{\text{crystal}}$ and M_{QWP} are the Jones matrices for the reflection by the TFP, the reflection by the mirror, the transmission through the nonlinear crystal and the transmission through the QWP. θ is the angle of the fast-axis of the QWP with respect to \hat{e}_p .

The Jones matrix for reflection by the TFP is easily understood from the fact that it selectively reflects s-polarized light. We also note here that the effect of the mirror on the incident field is to provide it with a π -phase shift for the s-polarized component on reflection and that the nonlinear crystal is essentially a transmissive element that does not alter the polarization of the incident field. The QWP is an optical component that is engineered to provide generate circularly polarized light, $\vec{E}_{\text{circ}} = \frac{1}{\sqrt{2}}(1, i)$, for light polarized 45° from its fast axis. Appropriate rotation of the coordinate system allows the derivation of M_{QWP} given in Eq.3.5. The interested reader is referred to [59] for further details.

The light in the cavity is reflected back and forth multiple times and makes several passes through the optical components. As per Eq.3.4, the round-trip Jones matrix is the product of the individual Jones matrices of each component in the sequence at which the light passes through (from Eq. 3.4). Thus, the Jones matrix of the cavity is given by

$$M_{\text{cav}} = M_{\text{TFP,refl}} \cdot M_{\text{crystal}} \cdot M_{\text{mir}} \cdot M_{\text{crystal}} \cdot M_{\text{TFP,refl}} \cdot M_{\text{QWP}}(\pi - \theta) \cdot M_{\text{mir}} \cdot M_{\text{QWP}}(\theta) \quad (3.7)$$

To better understand the polarization dynamics within the cavity, we differentiate the cavity into two segments - segment 1 : QWP-Mirror-QWP-TFP and segment 2 : Crystal-Mirror-crystal-TFP. The individual Jones matrices of these components are then given

by

$$\begin{aligned} M_{\text{Seg1}} &= M_{\text{TFP,refl}} \cdot M_{\text{QWP}(\pi - \theta)} \cdot M_{\text{mir}} \cdot M_{\text{QWP}(\theta)} \\ &= \begin{pmatrix} 0 & 0 \\ -i \sin(2\theta) & i \cos(2\theta) \end{pmatrix} \end{aligned} \quad (3.8)$$

and

$$\begin{aligned} M_{\text{Seg2}} &= M_{\text{TFP,refl}} \cdot M_{\text{crystal}} \cdot M_{\text{mir}} \cdot M_{\text{crystal}} \\ &= \begin{pmatrix} 0 & 0 \\ 0 & 1 \end{pmatrix} \end{aligned} \quad (3.9)$$

When light \vec{E}_{in} is incident onto the TFP, only the p-polarized component $\vec{E}_{\text{in}}^{\text{p}} = \vec{E}_{\text{in}} \cdot \hat{e}_{\text{p}}$ enters the cavity, into the segment 1. The effect of segment 1 on this light is to send

$$\begin{aligned} \vec{E}_{\text{inj}} &= M_{\text{Seg1}} \cdot \vec{E}_{\text{inc}}^{\text{p}} \\ &= \begin{pmatrix} 0 \\ -i \sin(2\theta) \end{pmatrix} \end{aligned} \quad (3.10)$$

into segment 2. The remaining light

$$??\vec{E}_{\text{refl}} = \vec{E}_{\text{inc}}^{\text{p}} - \vec{E}_{\text{inj}} \quad (3.11)$$

is transmitted through the TFP, and does not enter the segment 2, i.e, it is reflected from the cavity before the first roundtrip and is used for the Pound-Drever-Hall stabilization scheme. The second segment simply acts to choose the s-polarized component of the circulating field in each round trip. The total Jones matrix of the cavity is given by

$$\begin{aligned} M_{\text{cav}} &= M_{\text{Seg1}} \cdot M_{\text{Seg2}} \\ &= \begin{pmatrix} 0 & 0 \\ -i \sin(2\theta) & i \cos(2\theta) \end{pmatrix} \end{aligned} \quad (3.12)$$

Thus, if the CW laser light from the 1979 nm-seed laser is purely p-polarized so that $\vec{E}_{\text{in}} = (1, 0)$, the resultant field after one round-trip is given by

$$\vec{E}_{1,\text{RT}} = M_{\text{cav}} \cdot \vec{E}_{\text{in}} = \begin{pmatrix} 0 \\ -i \sin(2\theta) \end{pmatrix} = \vec{E}_{\text{inj}} \quad (3.13)$$

and the intensity of the field after one round-trip is given by

$$I_{1,\text{RT}} = \frac{c\epsilon_0}{2} |\vec{E}_{1,\text{RT}}|^2 = I_{\text{in}} \sin^2(2\theta) = I_{\text{inj}} \quad (3.14)$$

where $I_{\text{in}} = \frac{c\epsilon_0}{2} |\vec{E}_{\text{in}}|^2$ is the intensity of the light from 1979 nm-seed laser³. Thus, the intensity of the light from the seed laser is attenuated by a factor of $\sin^2(2\theta)$ by the cavity. Similarly, we can calculate the field after the 2nd round-trip,

$$\begin{aligned} \vec{E}_{2,\text{RT}} &= M_{\text{cav}} \cdot \vec{E}_{1,\text{RT}} = M_{\text{cav}}^2 \cdot \vec{E}_{\text{in}} \\ &= \begin{pmatrix} 0 \\ (-i)^2 \sin(2\theta) \cos(2\theta) \end{pmatrix} \end{aligned} \quad (3.15)$$

³ ϵ_0 and c refers to the electrical permittivity of vacuum and speed of light, respectively.

, ultimately the field after the n^{th} round-trip is given by

$$\vec{E}_{n,RT} = M_{\text{cav}}^n \cdot \vec{E}_{\text{in}} = \begin{pmatrix} 0 \\ (-i)^n \sin(2\theta) \cos^n(2\theta) \end{pmatrix} \quad (3.16)$$

and has the intensity

$$I_{n,RT} = I_{\text{inj}} \cos^{2n}(2\theta) \quad (3.17)$$

Thus, of the intensity $I_{\text{inj}} = I_{\text{in}} \sin^2(2\theta)$ that is injected into the cavity, the field suffers a polarization-dependent round-trip loss in its intensity given by

$$l_{RT}^{\text{Pol}} = \frac{I_{n-1,RT} - I_{n,RT}}{I_{n-1,RT}} = 1 - \cos^2(2\theta) \quad (3.18)$$

Thus, depending on the orientation θ of the QWP, the field experiences a loss per round-trip of $1 - \cos^2(2\theta)$. Note that this loss is in addition to the polarization-independent round-trip losses due to the imperfect reflections from optical surfaces of the cavity mirrors and the TFP and the transmission loss through the nonlinear crystal and the QWP. Factoring in the effective polarization independent reflectivity R_0 of the optics, the total round-trip loss is given by

$$l_{RT} = 1 - R_0 \cos^2(2\theta) \quad (3.19)$$

Intracavity spectral profile and finesse

We recollect from [59] that the circulating intensity in an optical cavity of length L_{cav} with round-trip losses l_{RT}

$$I_{\text{circ}}(\nu) = I_{\text{inj}}(\nu) \left[\left(1 - \sqrt{l_{RT}}\right)^2 + 4\sqrt{l_{RT}} \sin^2(\phi_{RT}(\nu, L_{\text{cav}})) \right]^{-1}, \quad (3.20)$$

when light of intensity $I_{\text{inj}}(\nu)$ at frequency ν . Here, $\phi_{RT} = \frac{2\pi\nu L_{\text{cav}}}{c}$ is the round-trip phase. The intracavity profile has an Airy distribution, which is well-approximated by a Lorentz lineshape (as shown in Fig.3.6). The Lorentzian finesse \mathcal{F} of the cavity, defined as the ratio of the FWHM of the intracavity profile $\Delta\nu_{\text{FWHM}}$ and the free spectral range $\delta\nu_{\text{FSR}} = c/2L_{\text{cav}}$, is given by

$$\begin{aligned} \mathcal{F}(\theta) &= \frac{\Delta\nu_{\text{FWHM}}}{\delta\nu_{\text{FSR}}} = -\frac{2\pi}{\ln(1 - l_{RT})} \\ &= -\frac{2\pi}{\ln(R_0 \cos^2(2\theta))} \end{aligned} \quad (3.21)$$

Using Eq.3.19, we find that the intracavity circulating intensity and the finesse of the cavity are dependent on the orientation of the waveplate θ as

$$I_{\text{circ}}(\nu) = I_{\text{inj}}(\nu) \left[\left(1 - \sqrt{R_0 \cos^2(2\theta)}\right)^2 + 4\sqrt{R_0 \cos^2(2\theta)} \sin^2(\phi_{RT}(\nu, L_{\text{cav}})) \right]^{-1}, \quad (3.22)$$

$$\mathcal{F}(\theta) = \frac{\pi}{2} \left[\sin^{-1} \left(\frac{1 - \sqrt{R_0 \cos^2(2\theta)}}{2\sqrt{R_0 \cos^2(2\theta)}} \right) \right]^{-1}, \quad (3.23)$$

For a frequency ν_0 that is resonant in the cavity, $\sin(\phi_{RT}) = 0$ so that

$$I_{\text{circ}}(\nu_0) = I_{\text{inj}}(\nu_0) \left[\left(1 - \sqrt{R_0 \cos^2(2\theta)} \right)^2 + 4\sqrt{R_0 \cos^2(2\theta)} \right]^{-1}, \quad (3.24)$$

From these equations, we note that as $\theta \rightarrow \frac{\pi}{4}$, the finesse of the cavity and intracavity power increase, the round trip loss is reduced, and resonances of cavity spectral profile become narrower. The opposite happens as $\theta \rightarrow 0$, with the cavity rejecting more injected light, reducing the finesse and intracavity power.

The OPO operation begins when the total gain due to the pump input energy is larger than the round-trip losses. We note here from [51], that the oscillation threshold E_{osc} for the OPO with a gain of G_0 per pump input energy

$$\begin{aligned} E_{\text{osc}} &= \frac{2l_{RT}}{G_0} \\ &= \frac{2(1 - \cos^2(2\theta))}{G_0} \end{aligned} \quad (3.25)$$

The low oscillation threshold implies that a high conversion efficiency is obtained for relatively low input pump energies. Thus, conversion efficiency saturation occurs much earlier for OPOs with low thresholds. The total amount of idler generated at high input energy is comparatively lower than that of an OPO with a larger round-trip loss. These two regimes, the oscillation threshold regime and the saturation regime, can be tuned by varying the round-trip losses of the OPO, a feature enabled by the QWP of the variable-finesse cavity design.

The damage threshold regime of the OPO, where the probability for optical damage on the optics is high, is also determined also by the intracavity power. A higher intracavity power, i.e, a higher cavity finesse increases the probability for damage of the nonlinear crystal for the same input pump fluence. In the OPO cavity, the nonlinear crystal has the lowest optical damage threshold ($\sim 2 \text{ J/cm}^2$) among the optics and is most susceptible to damage. Thus for long-term stable operations, it a lower finesse is preferred.

The ideal operation point of the OPO is determined by the energy budget of the 1030 nm input pulse energy, the required output energy dictated by subsequent parts of the laser system and inherent losses of the cavity. To optimize operating at a given input pulse energy of 1030 nm to produce a set output energy of 2.1 μm , the intracavity power and cavity losses needs to tuned to optimize the between the oscillation threshold point, saturation limit and the damage threshold regime. The variable finesse cavity, for which the cavity finesse is dependent on the orientation θ of the QWP angle, allows one to balance the operating point accordingly.

The measurements in Fig.3.5 show the variation of the cavity finesse with the angle of the QWP. To determine the finesse, the cavity profile (Fig.3.6) was against a Lorentz function. The FWHM linewidth of the cavity profile and the free spectral range were determined. The fit of the function described in Eq.3.23 agrees well with the measured data. The fit determines the maximum round trip loss to be $R_0 = 0.968$. A maximum finesse \mathcal{F}_{max} of ~ 182.91 is expected to be possible.

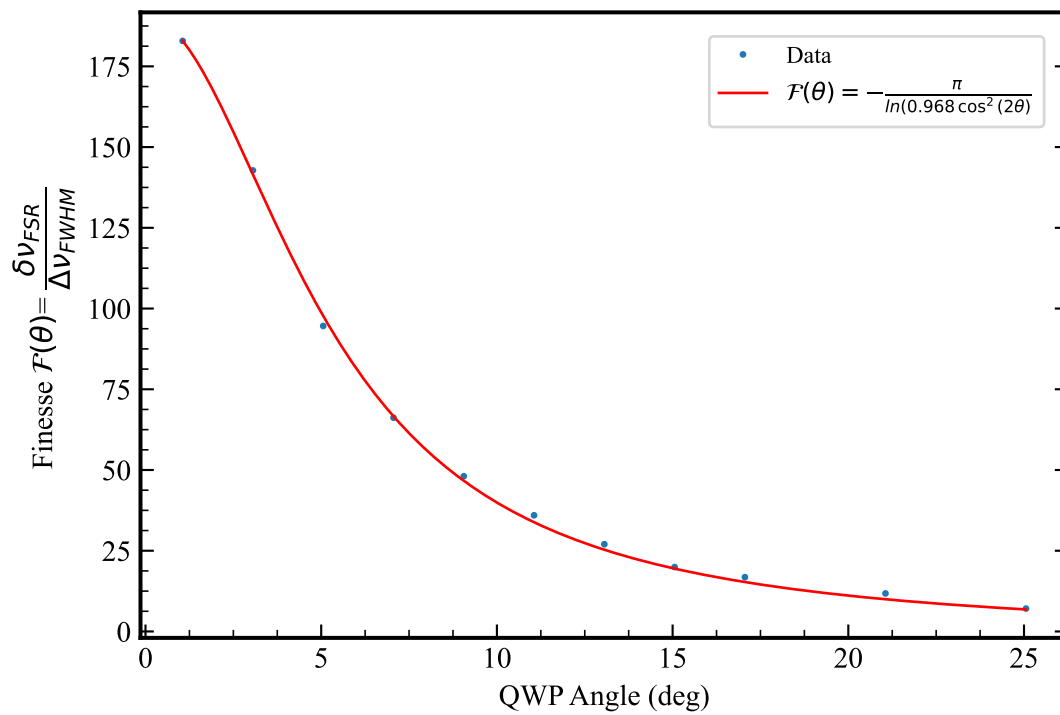


Figure 3.5: Variation of the cavity finesse with the angle of the QWP. Eq.3.23 is used to fit the data. The total polarization-independent roundtrip loss is determined to be 96.8% from the fit.

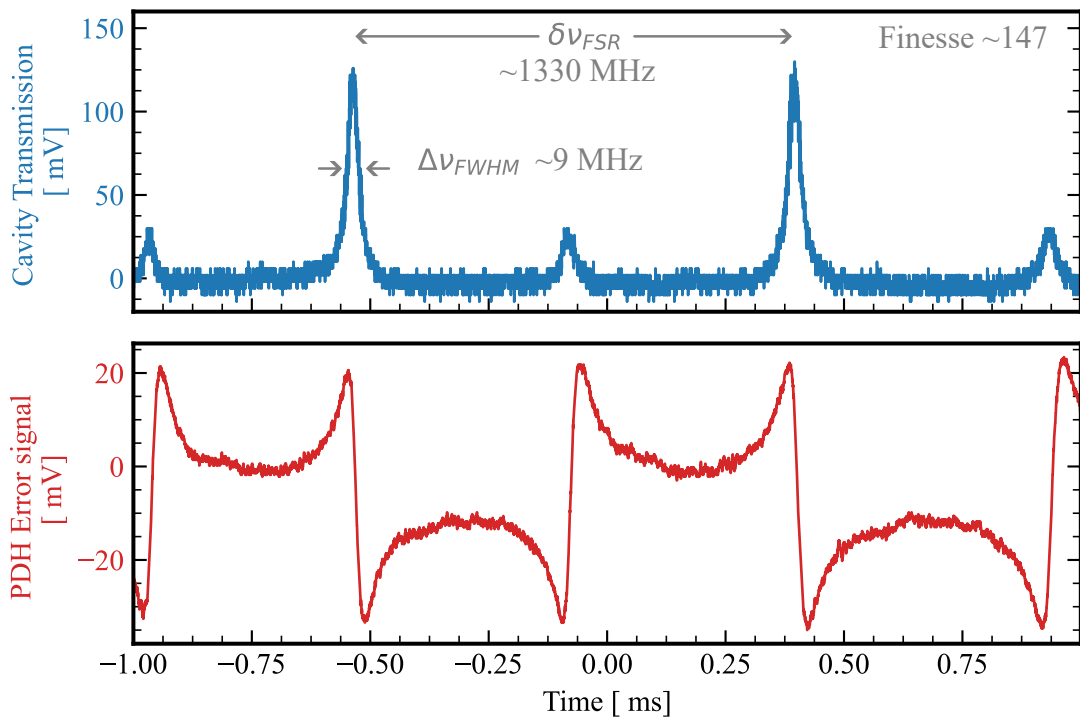


Figure 3.6: Trace of cavity transmission and the PDH-error signal as measured by photodiode PD1 and PD2, respectively (see Fig.3.1) The side-bands are positioned at half the free spectral range $\delta\nu_{FSR}$ away from the carrier.

Pound-Drever-Hall stabilization

We recollect from [59] that only those frequencies that satisfy the relation ν

$$L_{\text{cav}} = \frac{m\lambda}{2} \quad (3.26)$$

where $m = 1, 2, \dots$ are resonant in the cavity. To ensure that the CW laser light from 1979 nm-seed laser of frequency ν_S is always resonant in the cavity during the operation of the laser system, the cavity length L_{cav} must be optimized to satisfy the above condition. This is achieved by Pound-Drever-Hall (PDH) stabilization [56, 60] of the cavity length to match the frequency ν_S of 1979 nm-seed laser.

The PDH scheme involves phase-modulating the injected beam to generate sidebands about its centre frequency. A beat signal between the light that does not enter the cavity ($\propto \vec{E}_{\text{refl}}$, see Eq.??) and the light that is exiting the cavity after several round trips provides a phase-sensitive signal of deviation from the resonance. This signal can be demodulated and used to stabilize the cavity length L_{cav} to the injected frequency ν_S .

Consider that the incident field from the 1979 nm-seed laser is $E_L(t) = E_0 e^{i2\pi\nu_S t}$ of amplitude E_0 and phase-modulation generates sidebands at Ω . The resultant field is given by

$$E_{\text{inc}}(t) = E_0 e^{i(2\pi\nu_S t + \beta \sin \Omega t)} \quad , \quad (3.27)$$

where β is the modulation depth. Compared to the field from the laser E_L , this field consists of side-bands $\nu_S \pm \Omega/2\pi, \nu_S \pm 2\Omega/2\pi, \dots$, distributed about the carrier frequency ν_S . We limit our analysis to the scenario of interest ($\beta < 1$) where most of the power is distributed to the first-order sidebands at $\nu_S \pm \Omega/2\pi$ and the carrier frequency ν_S . The field after phase modulation is then approximated by Taylor expansion to be

$$E_{\text{inc}}(t) \approx E_0 \left[J_0(\beta) e^{i2\pi\nu_S t} + J_1(\beta) e^{i(2\pi\nu_S + \Omega)t} - J_1(\beta) e^{i(2\pi\nu_S - \Omega)t} \right] \quad (3.28)$$

Here, $J_i(\beta)$ refers to the Bessel function of the first kind. The field reflected E_{ref} by a typical two-mirror cavity is given by

$$E_{\text{ref}} = E_0 [r(\nu_S) J_0(\beta) e^{i2\pi\nu_S t} + r(\nu_S + \Omega/2\pi) J_1(\beta) e^{i(2\pi\nu_S t + \Omega t)} - r(\nu_S - \Omega/2\pi) J_1(\beta) e^{i(2\pi\nu_S t - \Omega t)}] \quad (3.29)$$

where $r(\nu)$ is the reflectance of the cavity. The reflectance of a typical two-mirror cavity with round-trip losses \mathcal{L}_{RT} and free spectral range $\delta\nu_{\text{FSR}}$ is given by [56]

$$r(\nu) = \frac{(1 - \mathcal{L}_{\text{RT}})(e^{i2\pi\nu/\delta\nu_{\text{FSR}}} - 1)}{1 - (1 - \mathcal{L}_{\text{RT}})^2 e^{i2\pi\nu/\delta\nu_{\text{FSR}}}} \quad (3.30)$$

In our variable finesse cavity design, the polarization-dependent round-loss, given by Eq.3.19, implies that the reflectivity of the cavity (Eq.3.31) also depends on the orientation θ of the QWP. Thus

$$r(\nu) = \frac{R_0 \cos^2(2\theta) e^{i2\pi\nu/\delta\nu_{\text{FSR}}} - 1}{1 - R_0^2 \cos^4(2\theta) e^{i2\pi\nu/\delta\nu_{\text{FSR}}}} \quad (3.31)$$

Thus, once again, cavity reflectivity can be tuned by varying θ , allowing for more optical power available for the reflected signal from the cavity. Using this reflected intensity

is given by

$$\begin{aligned}
I_{\text{ref}} = & I_c |r(\nu_S)|^2 + I_s \{ |r(\nu_S + \Omega/2\pi)|^2 + |r(\nu_S - \Omega/2\pi)|^2 \} \\
& + 2\sqrt{I_c I_s} \{ \text{Re} [r(\nu_S)r^*(\nu_S + \Omega/2\pi) - r^*(\Omega/2\pi)r(\nu_S - \Omega/2\pi)] \cos(\Omega t/2\pi) \\
& + \text{Im} [r(\nu_S)r^*(\nu_S + \Omega/2\pi) - r^*(\Omega/2\pi)r(\nu_S - \Omega/2\pi)] \sin(\Omega t/2\pi) \} \\
& + (2\Omega/2\pi \text{ terms}) \quad , \quad (3.32)
\end{aligned}$$

, and is detected by a photodetector that measures the reflected light from the cavity. Note that while the terms with $|r(\nu_S)|^2$, $|r(\nu_S + \Omega/2\pi)|^2$ and $|r(\nu_S - \Omega/2\pi)|^2$ have constant intensity in time, while the cross-terms give the sinusoidally varying beat-note.

$$\begin{aligned}
e(t) = & 2\sqrt{I_c I_s} \{ \text{Re} [r(\nu_S)r^*(\nu_S + \Omega/2\pi) - r^*(\nu_S)r(\nu_S - \Omega/2\pi)] \cos(\Omega t/2\pi) \\
& + \text{Im} [r(\nu_S)r^*(\nu_S + \Omega/2\pi) - r^*(\nu_S)r(\nu_S - \Omega/2\pi)] \sin(\Omega t/2\pi) \} \quad (3.33)
\end{aligned}$$

The amplitude of the beat note is dependent on the difference in the contribution of the positive sideband $r(\nu_S)r^*(\nu_S + \Omega/2\pi)$ to that from the negative sideband $r^*(\Omega/2\pi)r(\nu_S - \Omega/2\pi)$. As the cavity is minimally reflective at perfect resonance, these terms signify the distance between the resonant frequency of the cavity and the frequency ν_S of the 1979 nm-seed laser. A positive (negative) amplitude for this difference implies that the resonance frequency of the cavity must be red-shifted (blue-shifted) to ensure that ν_S is resonant in the cavity with $e(t) \rightarrow 0$ as ν_S is fully resonant. Thus, the resonance of the intracavity profile is determined by the point at which this difference is zero. By demodulating this signal at $\Omega/2\pi$, we obtain a measure of the deviation of the resonance frequency of the cavity from the frequency ν_S of the 1979 nm-seed laser. An appropriate variation of the cavity length or the signal frequency can be used to satisfy this condition at all times, thereby ensuring that the injection-seeded photons are always resonant within the cavity.

Fig.3.7 shows the intracavity profile of the cavity and the demodulated error signal for different values of modulation frequency for a cavity of length $L_{\text{cav}}=11.2$ cm, corresponding to a free-spectral range of $\delta\nu_{\text{FSR}}=1332$ MHz. The phase of the demodulation determines the relative orientation of the slope of the error signal. Here, we consider the case when the resonance of the cavity corresponds to the zero-point in the negative-slope region of the error signal. When $\Omega/2\pi=400$ MHz or 800 MHz, we see that there exist other regions where the sloped of the error signal is negative, corresponding to the interference of the side-bands of the resonance. This indicates that for these values of modulation frequency, a unique determination of the resonance from the error signal is not possible. However, when the modulation is set to be $\Omega/2\pi =666$ MHz, i.e., half the free-spectral range of the cavity, the positive sideband of a resonance combines with the negative sideband of the next resonance to negate their respective out-of-phase components, leading to a region where the side-bands are uniquely determined by a positive-slope of the error signal. The absence of a negative-slope region near the sidebands allows for the resonance of the cavity profile to be uniquely determined. Thus, when environmental perturbations unlock the phase-locked loop, an immediate relock to the nearest cavity mode is carried out, ensuring that the OPO cavity is always locked to the 1979 nm-seed laser, leading to a single-frequency operation. The modulation frequency used for PDH locking is thus set to be half the free spectral range of the cavity. Further features of this condition are explored in the publication [57].

Fig.3.6 shows the trace of the cavity transmission profile as measured with photodetector PD1 (See Fig.3.1). The corresponding error signal of the PDH locking obtained after

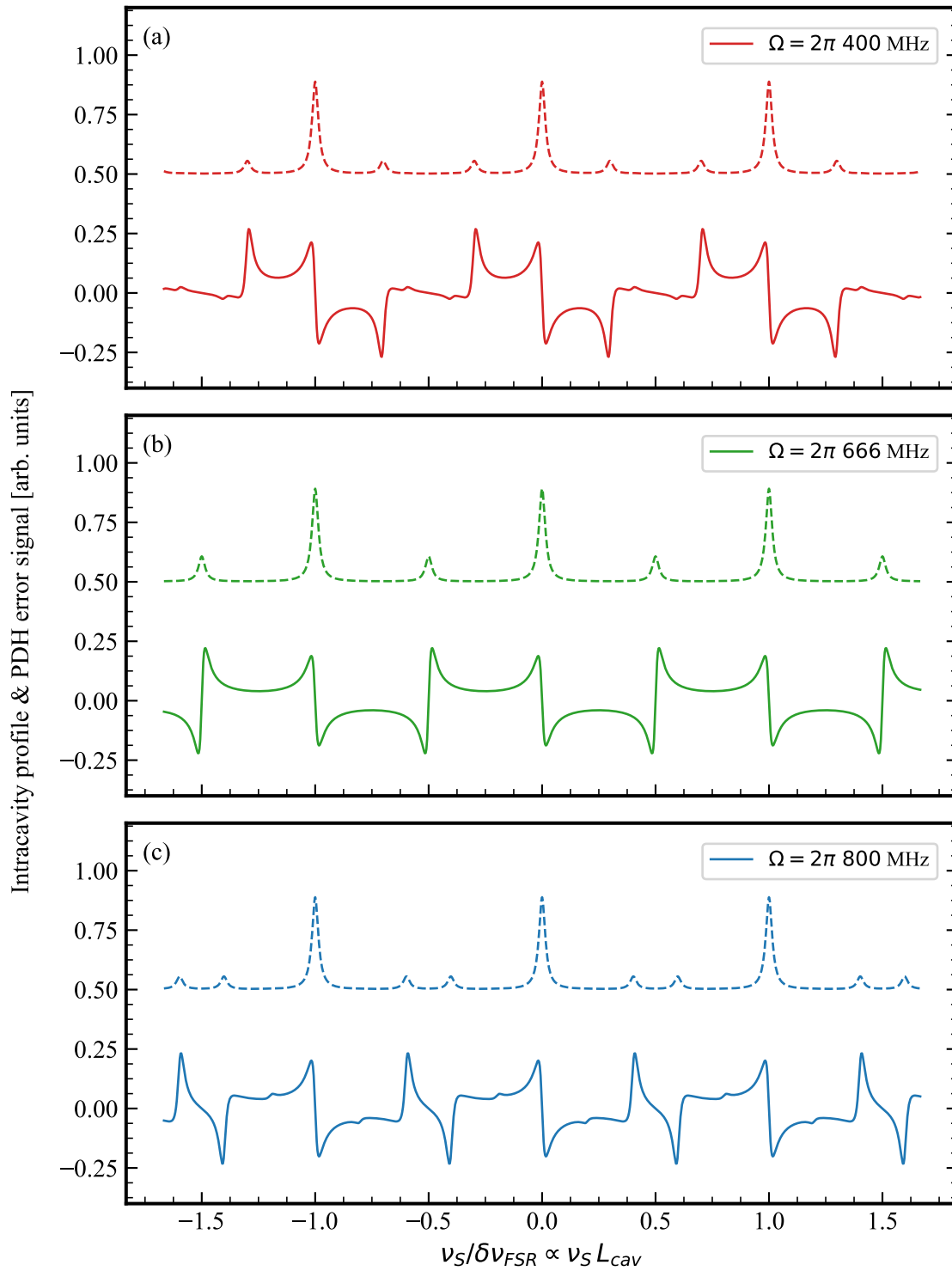


Figure 3.7: Intracavity profile (dotted lines) and the error signal (solid lines) of PDH locking for a cavity of length 11.2 cm for different modulation frequencies $\Omega/2\pi =$ (a) 400 MHz (b) 666 MHz ($=\delta\nu_{\text{FSR}}/2$) (c) 800 MHz. The locking point of the PDH stabilization scheme is determined by the slope at the zero-point of the error signal and the zero-point.

demodulation is shown below. As we would like to ensure that a given frequency ν_s of the 1979 nm-seed laser is resonant within the cavity, we modulate the cavity length L_{cav} (rather than the frequency of the 1979 nm-seed laser) to satisfy the resonance condition set by the error signal. To control the cavity length with an electronic signal, one of the cavity mirrors (M4) was glued to a piezo-electric transducer (PZT), to which the error signal after demodulation was applied.

3.3 CHARACTERIZATION OF THE OPO

Characterization scheme

To characterize the operating regime of the OPO, the scheme shown in Fig.3.8 is implemented. The intracavity profile, monitored by the photodetector PD1, is used to determine the cavity finesse. The temperature T of the nonlinear crystal is controlled by a thermoelectric controller (TEC). The energy of the 1030 nm and 2.1 μ m pulses after the OPO is measured by energy meters EM1 and EM2, respectively. For both the pulses, the mean energy and RMS deviation of 100 pulses are used for characterization. To characterize their spatial profile, part of the 2.1 μ m pulses is focused with a planoconvex lens f_1 . A camera measures the spatial profile of the beam and determines the beam diameter $D_{4\sigma}$ of the 2.1 μ m pulses. Using this layout, the performance of the OPO at different crystal temperatures T , cavity finesse \mathcal{F} and input 1030 nm energy and the spatial profile is characterized. Fig. 3.9 shows the variation of the conversion efficiency of the OPO operation, normalized to the maximum observed value, with the crystal temperature. Away from the optimum temperature for phase-matching, the conversion efficiency η defined as

$$\eta = \frac{E_{in,1030} - E_{out,1030}}{E_{in,1030}} = \frac{E_{out,2149} + E_{out,1979}}{E_{in,1030}} \quad (3.34)$$

is expected to decrease with the temperature T as a sinc^2 -function (See Sec.2.2). The fit

$$\eta(T) = \eta_{max} \text{sinc}^2 \left(0.886 \frac{T - T_0}{\Delta T_{FWHM}} \right) \quad (3.35)$$

to the data indicates that the phase matching of the nonlinear process is most optimum at $T_0=24.66$ °C. The phase matching bandwidth, given by the FWHM of the fit ΔT_{FWHM} , is determined to be 10 °C. Compared to the thermal stability of 0.1 °C achieved by the TEC, the phase matching is well-tolerant and optimized for the nonlinear process. Fig.3.10 plots the energy of generated 2.1 μ m pulses against that of the input 1030 nm pulses for different cavity finesse as well as the conversion efficiency. Input 1030 nm pulse energy is limited to <7 mJ to avoid optical damage of the nonlinear crystal. As expected, we see that the oscillation threshold is lower, leading to OPO operation at relatively lower values of input pump energy as compared to the case for low finesse. However, the conversion efficiency begins to saturate much earlier for higher finesse, thereby reducing the total amount of energy $E_{out,2149}$ generated for the given pump energy. These features of the OPO allow us to optimize the operation for a given value of input pump energy, i.e., to maximize $E_{out,2149}$ by varying the Finesse \mathcal{F} for the given $E_{in,1030}$.

The effect of injection-seeding and PDH stabilization on the energy of 2.1 μ m pulses is studied in Fig.3.11. In Fig.3.11-a), the energy of 2.1 μ m is plotted against that of input 1030 nm for different cases - without injection-seeding and PDH stabilization, with injection-seeding but without PDH stabilization and with injection-seeding and PDH stabilization. The PDH stabilization of the cavity to the 1979 nm-seed laser provides a much

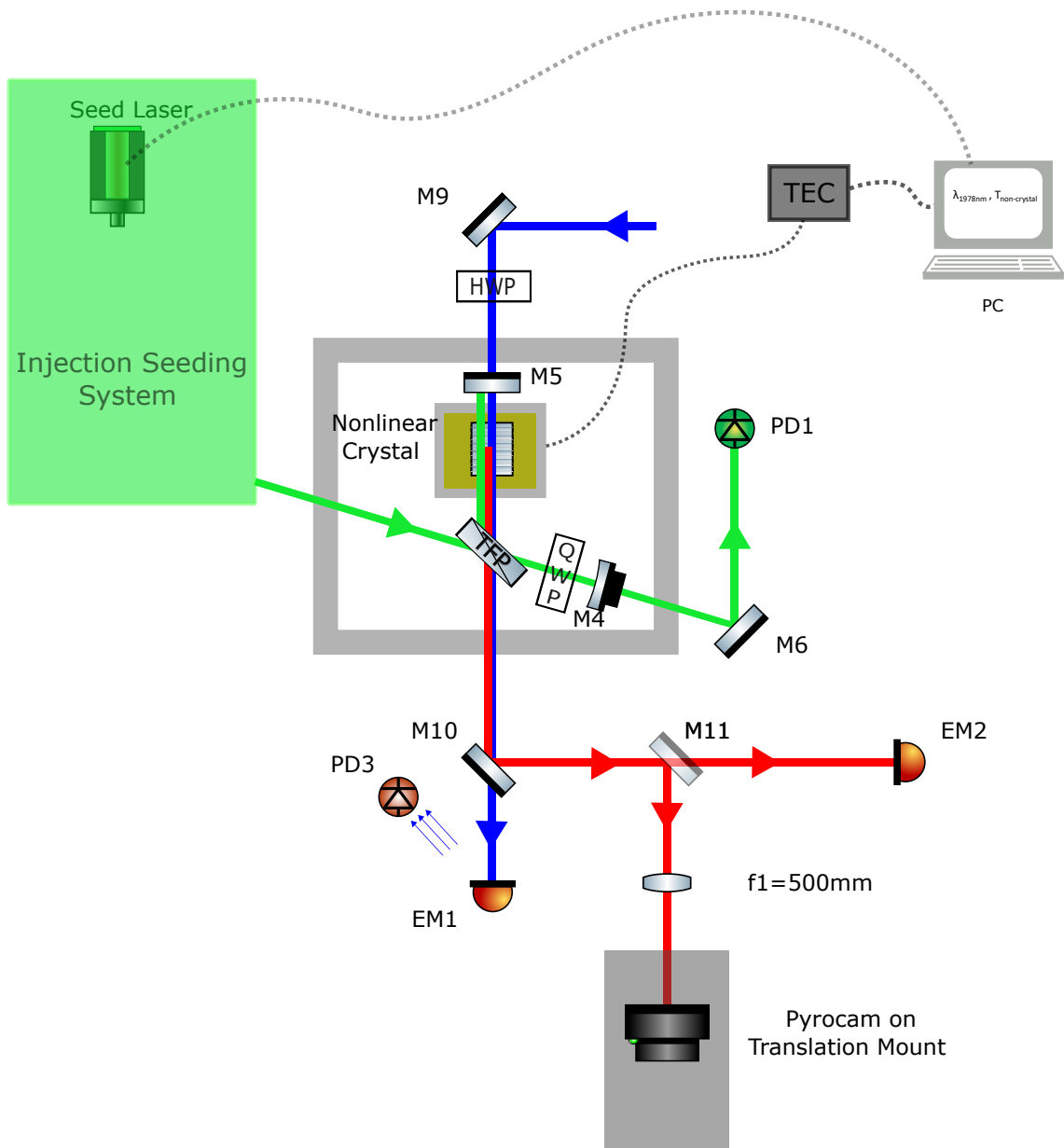


Figure 3.8: Scheme used for energy and beam quality characterization of the output of the OPO

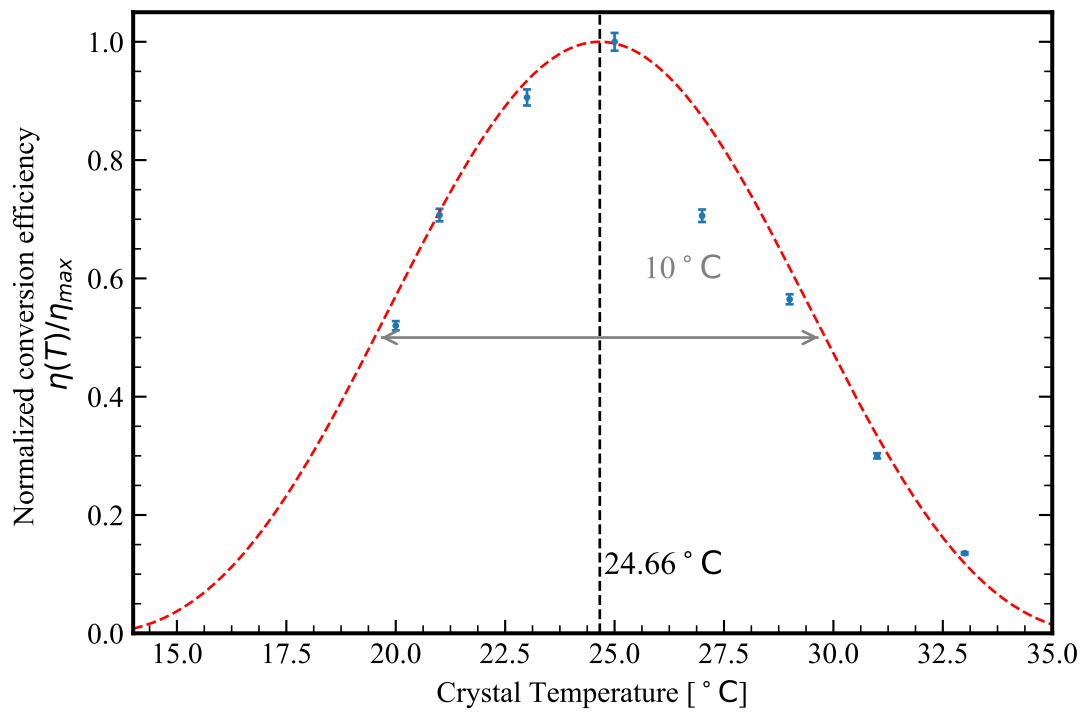


Figure 3.9: Variation of conversion efficiency of the 2.1 μm -OPO with the temperature of the crystal. The conversion efficiency, calculated using Eq.3.34 is fit to a sinc^2 -function. The fit determines the optimum temperature and the phase-matching bandwidth (FWHM) to be $T_0 = 24.66^\circ\text{C}$ and $\Delta T_{\text{FWHM}} = 10^\circ\text{C}$, respectively.

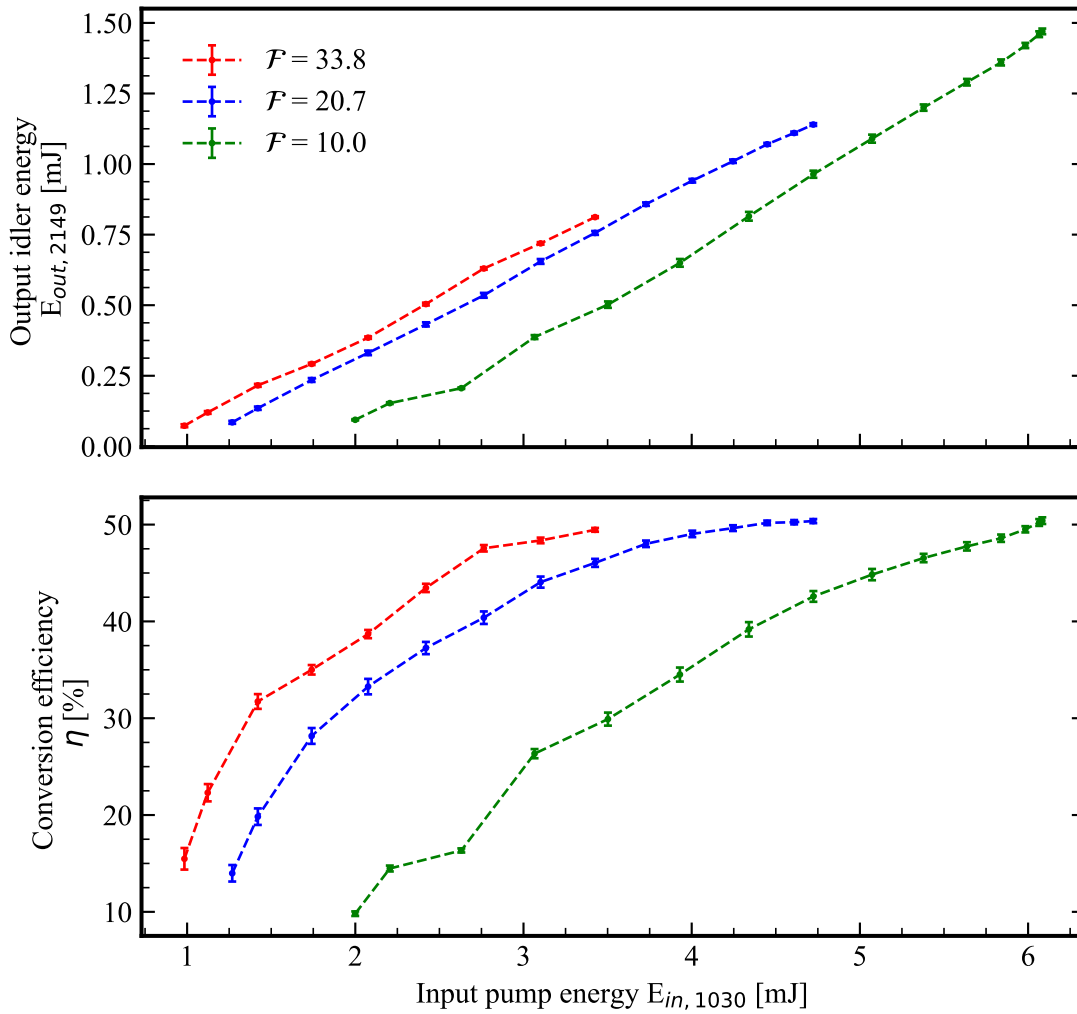


Figure 3.10: Variation of the energy of 2.1 μ m pulses with that of the 1030 nm pulses for different cavity finesse.

higher pulse energy of $2.1\ \mu\text{m}$ for the same energy of $1030\ \text{nm}$ pulses. Moreover, the energy stability is much higher (Fig.3.11-b), characterized by the lowest RMS deviation ($\sim 1\%$ for $E_{\text{in},1030} > 3.5$) among the three cases. We note that in this regime, the energy stability approaches that of the $1030\ \text{nm}$ input pulses. It is seen that even without PDH stabilization, the injection seeding of the OPO cavity gives rise to a higher pulse energy compared to that without injection seeding. However, when PDH stabilization is inactive, it is not necessary that the injection-seeded light is resonant in the cavity. Thus, every time a $1030\ \text{nm}$ pulse pumps the OPO, a different signal cavity mode dominates during pumping, with the injection-seeded $1.9\ \mu\text{m}$ mode being resonant and dominating for some but not all of the 100 measured pulses. This gives rise to higher energy with lower stability when the cavity is injection-seeded with no PDH stabilization scheme.

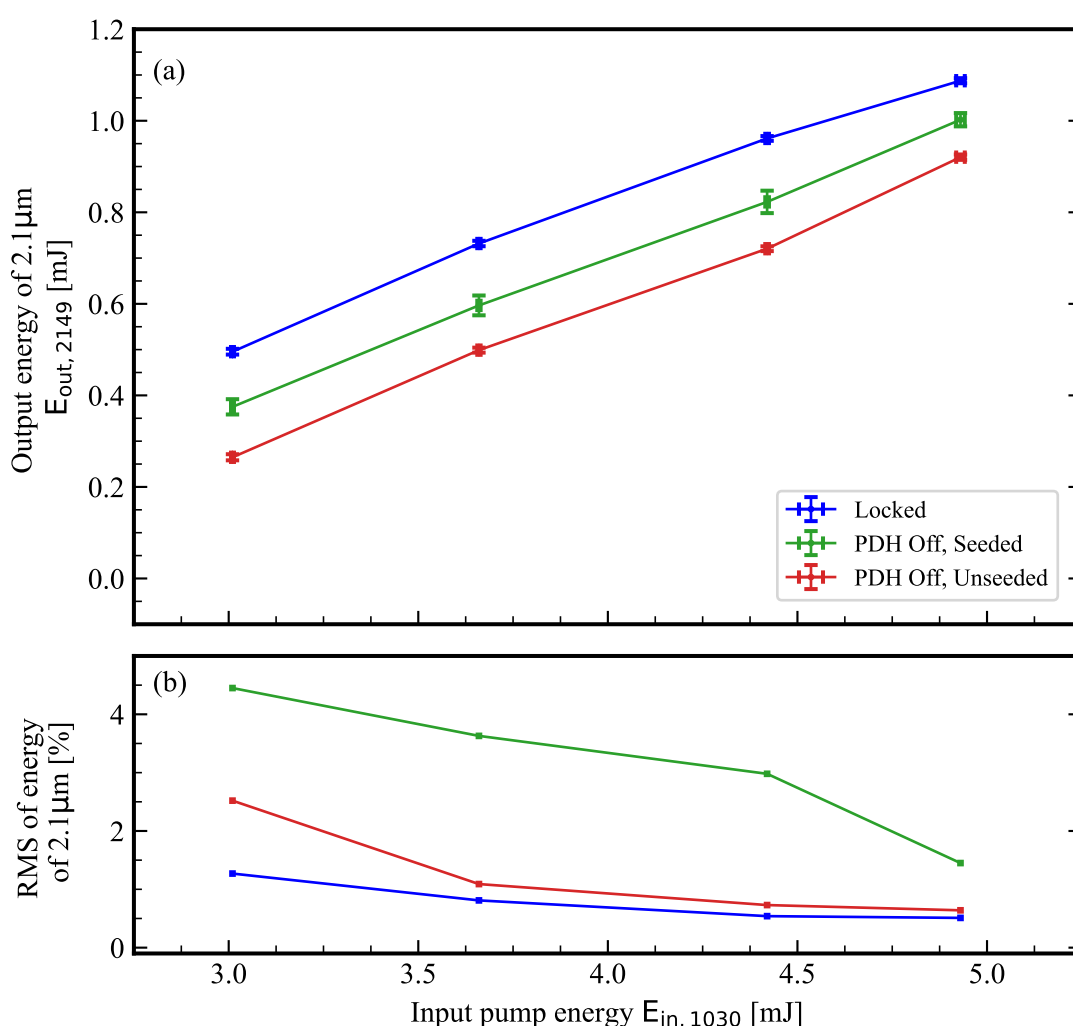


Figure 3.11: Average energy of $2.1\ \mu\text{m}$ pulses and the RMS of 100 pulses for conditions of Pound-Drever-Hall locking and injection seeding. Blue: PDH locking of OPO cavity to injection seeded light is active. Green: PDH locking is inactive while the OPO cavity is injection-seeded. Red: PDH locking of OPO cavity is inactive, and the cavity is not injection seeded.

The beam profile measured by the camera is used to determine the M^2 of the $2.1\ \mu\text{m}$

beam. The beam diameter $D4\sigma_M$ and $4\sigma_m$ of the 2.1 μm pulses along the major and minor beam axis is measured. The measured data is shown in Fig.3.12. The fitting method is identical to that described in [61]. A second-order polynomial is fit to the square of the measured beam diameter along the major axis of the beam

$$D4\sigma = \sqrt{a + bz + cz^2} \quad (3.36)$$

which allows the determination of the M^2 of the 2.1 μm beam along the major axis as

$$M_{M}^2 = \frac{\pi}{8\lambda} \sqrt{4ac - b^2} \quad (3.37)$$

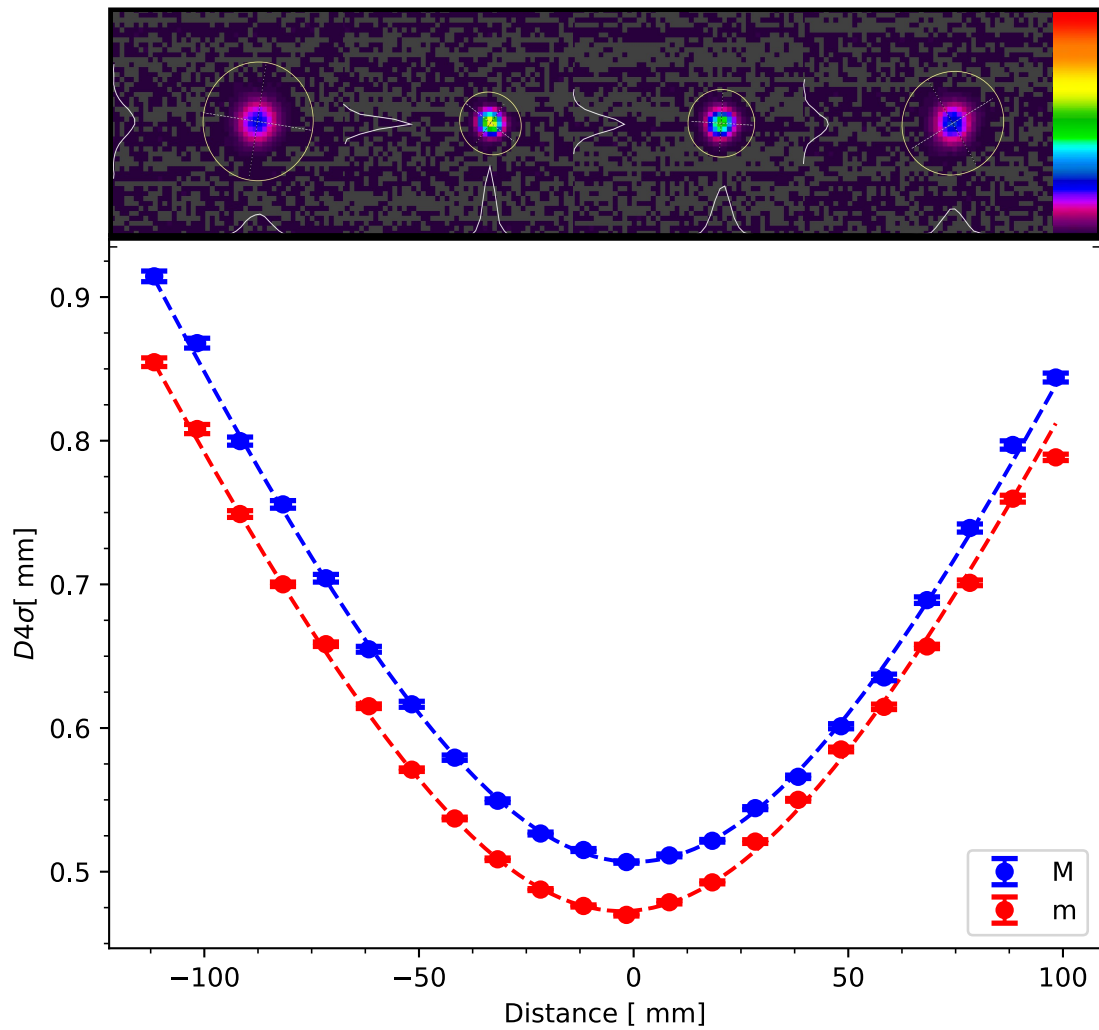


Figure 3.12: Beam quality characterization of OPO output. Variation of the beam diameter $D4\sigma_M$ and $4\sigma_m$ along the major and minor axis of the beam is plotted against the distance from the focus. The function $D4\sigma = \sqrt{a + bz + cz^2}$ is seen to adequately describe the evolution of the beam diameter

Similarly, M_{m}^2 of the 2.1 μm beam along the minor axis can be determined. In this manner, the beam quality factors along the major and minor axis are determined as $M_{M}^2=1.26(0.02)$ and $M_{m}^2=1.13(0.02)$. Compared to the $M_{M,TDO}^2=1.30$ and $M_{m,TDO}^2=1.33$

of the 1030 nm pump beam [55, 43], the 2.1 μm pulse is seen to have a M^2 much closer to unity, i.e, the generated 2.1 μm beam has a more a Gaussian spatial profile than the input pump beam. This mode-cleaning can be traced back to the OPO cavity which only allows a specific spatial profile (see Fig.3.2) for the injection-seeded resonant 1.9 μm signal beam. The PDH stabilization and injection-seeding, shown to increase the fluence (Fig.??), promotes the generation of 1.9 μm photons of the spatial profile maintained by the cavity. The spatial profile of the 2.1 μm , which depends on the overlap between the 1030 nm and the 1.9 μm beams, is hence constrained closer to unity by the resonant 1.9 μm intracavity beam.

3.4 CONCLUSION

A singly-resonant OPO featuring a variable-finesse cavity is realized. The OPO cavity is injection-seeded and PDH stabilized to CW-1.9 μm photons to ensure single-frequency operation. Within the OPO, the nonlinear crystal PPLNB downconverts the 1030 nm into 2.1 μm and 1.9 μm photons.

We realize the target set by the subsequent parts of the laser system by generating 1 mJ of 2.1 μm pulses for the energy budget of 5 mJ of the 1030 nm pump. The finesse of the cavity provide a degree of freedom to choose the operating point, according to any change in the energy budget or required output. The pulses have an energy stability of <1% RMS, largely limited by the energy stability of the 1030 nm pulses. Moreover, the high-energy 2.1 μm pulses are seen to have a nearly Gaussian spatial profile, characterized by an excellent beam quality factor $M_{M}^2=1.26(0.02)$ and $M_{m}^2=1.13(0.02)$, along the major and minor axis. The beam quality is also limited by that of the 1030 nm input pulses from the TDO. In short, the generated 2.1 μm pulses are ready for amplification by the subsequent 2.1 μm OPA stage.

The newly generated 2.1 μm pulses from the 2.1 μm -OPO (see Chapter 3) do not satisfy the energy requirement to drive the DFG of 6.8 μm as only a maximum energy of ~ 1 mJ is available for 5 mJ of 1030 nm input pump energy. As increasing the input pulse energy of 1030 nm, brings the operating point of the OPO closer to the damage threshold regime, we must separately amplify the pulses by an optical parametric amplifier (OPA) - the 2.1 μm -OPA. We recollect here from the design considerations of the laser system (Chapter 2) that the goal of the 2.1 μm -OPA is to amplify the 2.1 μm pulses to an energy of 25 mJ for an energy budget of ~ 175 mJ pulse energy for the 1030 nm pulses. However, as the TDA is under optimization, we are limited to a maximum 1030 nm pulse energy of 20 mJ from the TDO and 100 mJ available as pump energy of the OPA. Here, we present the results on the 2.1 μm -OPA when pumped with the aforementioned 1030 nm energies from the respective systems.

Within the OPA, the 1030 nm photons from the TDO and the 2.1 μm photons from the 2.1 μm -OPO interact to produce more 2.1 μm photons and 1.9 μm . While nonlinear process is identical to that in the 2.1 μm -OPO, it is not enhanced by an optical cavity (as in the OPO) but occurs in a single-pass through the nonlinear crystal. Ideally, the amplification process must not deteriorate the spatial profile (characterized by the M^2) of the 2.1 μm pulses as any aberrations in the wavefront can propagate to the subsequent DFG stage of the laser system. Thus, the M^2 of the 2.1 μm pulses after amplification must be as close to unit as possible. Finally, a broad phase matching bandwidth of the OPA operation is ideal for the thermal stability of the whole system.

Technical Implementation

The nonlinear process becomes more efficient with intensity ($I \propto w_0^{-2}$), with smaller beam waists (w_0) driving the conversion process more efficiently (see Chapter 2). In contrast to the 2.1 μm -OPO, where design constrains the beam sizes, a more flexible choice of beam waists are allowed in the case of the 2.1 μm -OPA. Note that the nonlinear crystal of choice, periodically poled KTP (PPKTP) has a very high damage threshold (See Table 2.1). This implies that the minimum possible Gaussian beam radius is $w_{1/e^2} \sim 220$ μm for the 21 mJ of total incident energy. To maximally drive the nonlinear process, we set the beam waist of the 1030 nm and 2.1 μm pulses to have a beam waist of ~ 245 μm .

The optical layout of the OPA is displayed in Fig.4.1. Before their amplification, the 2.1 μm pulses are separated from the depleted 1030 nm pulse that pumps the 2.1 μm -OPO by dichroic mirrors DCM1 and DCM2. The lens f1 collimates the 2.1 μm pulse while the lenses f2 and f3 shape the beam to the required beam waist. Similarly, the 1030 nm pulses from the TDO are beam-shaped by lenses f4 and f5 to the required beam waist. The propagation length of the pulses is set such that both the pulses meet at the PPKTP crystal simultaneously. The phase matching of the nonlinear process in the PPKTP crystal

(dimensions $4 \times 4 \times 12$ mm, poling period $37.87 \mu\text{m}$) is optimized by adjusting the crystal temperature with a commercial oven.

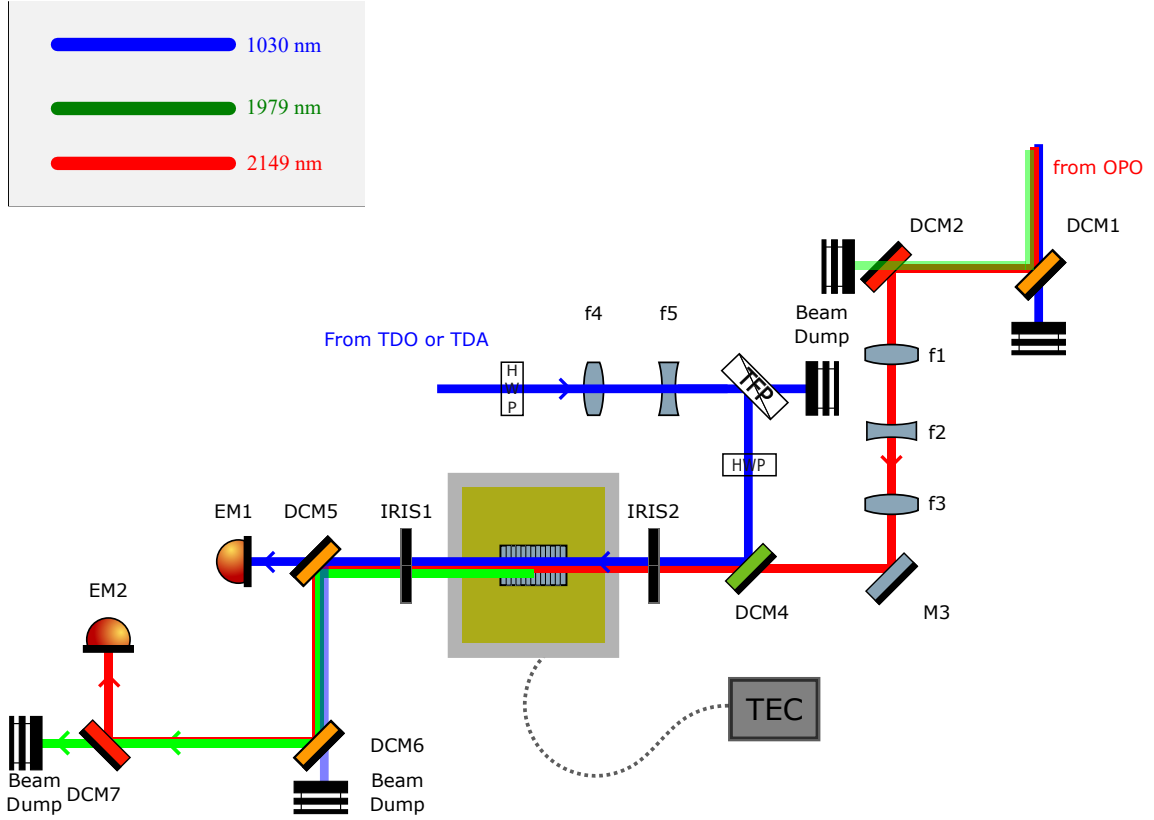


Figure 4.1: Optical layout of the $2.1 \mu\text{m}$ -OPA is shown. The 1030 nm pulses (blue) are used to amplify the $2.1 \mu\text{m}$ pulse (red) from the OPO. The $2.1 \mu\text{m}$ pulses are overlapped with the 1030 nm pulses within the PPKTP crystal. The crystal is housed in a commercial oven controlled by a thermoelectric controller. The amplified pulses of $2.1 \mu\text{m}$, the newly-generated $1.9 \mu\text{m}$ (green) and the depleted 1030 nm pump pulses are separated using dichroic mirrors DCM5 and DCM6. Energy meters EM1 and EM2 are used to characterize the depletion of energy of 1030 nm pulse and the amplification of the $2.1 \mu\text{m}$ pulse.

Characterization

To characterize the OPA operation, the average pulse energy and standard deviation at 100 pulses of $2.1 \mu\text{m}$ and 1030 nm are measured after the OPA by energy meters EM2 and EM1, respectively. Similar to PPLNB used in the $2.1 \mu\text{m}$ -OPO, the PPKTP crystal is quasi-phase-matched. To optimize the phase matching of the nonlinear process, the temperature of the crystal is tuned to maximize the measured energy of the $2.1 \mu\text{m}$ pulses (or equivalently, minimize the measured energy of the depleted 1030 nm pulses) and hence the conversion efficiency of the OPA for the given input 1030 nm pump energy. Fig. 4.2 shows the observed variation of the conversion efficiency of the $2.1 \mu\text{m}$ pulses (calculated as in Eq.3.34) with the crystal temperature. The optimum phase matching temperature is determined to be 38.95°C . Moreover, the phase matching is seen to be extremely broad, with the data fitting to the expected Sinc^2 -dependence with an FWHM of 96°C . For further characterization, the crystal was set to 38.95°C .

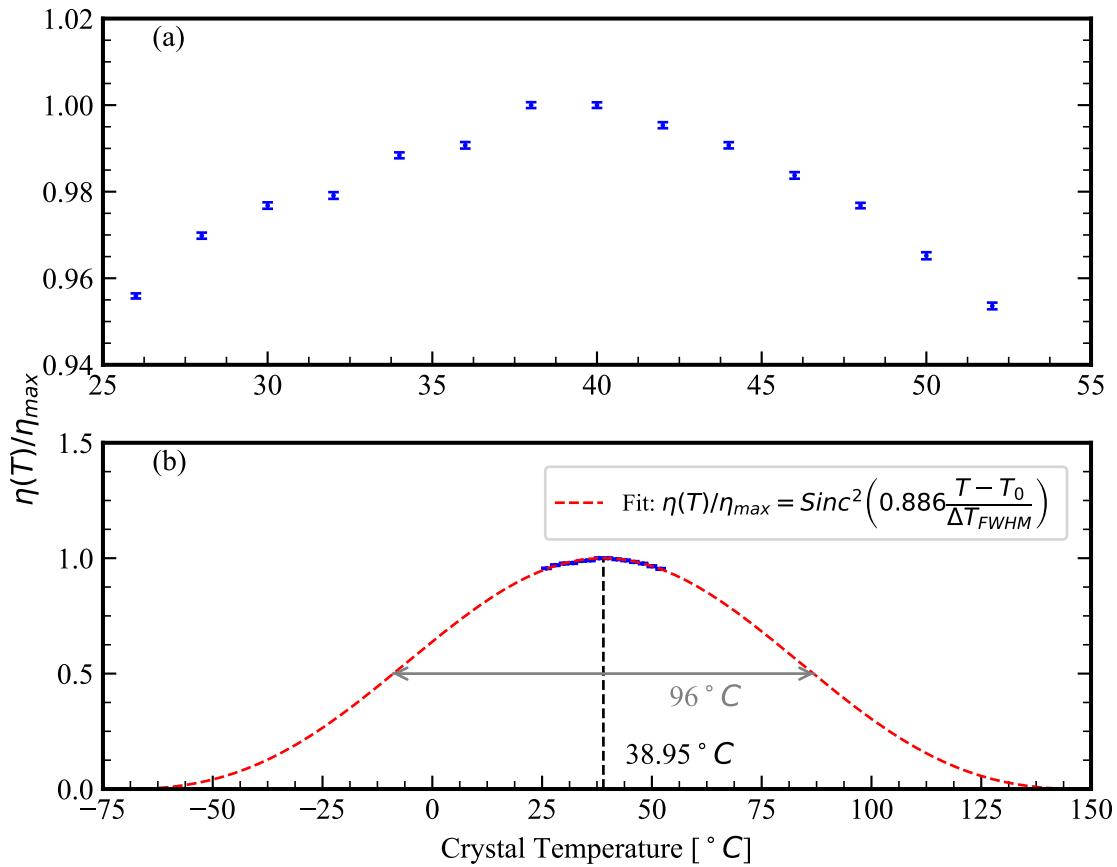


Figure 4.2: Variation of conversion efficiency of the 2.1 μm -OPA with temperature of the crystal. (a) Measured data (b) A sinc^2 – function is fitted to the data, extrapolated to larger temperature range to highlight the broad phase matching bandwidth. The optimum phase matching temperature is determined to be 38.95 °C from the fit. Additionally, the phase matching is extremely broad, with the FWHM of the fit determined to be 96 °C.

Amplification of the 2.1 μm pulses by the 1030 nm pulses is studied in Fig.4.3. The measured energy is seen to compare well with the corresponding SNLO simulations. Overall, the average energy of the 2.1 μm pulses is seen to be very stable ($<1\%$) as indicated by the standard uncertainties (standard deviation/ \sqrt{n} , number of pulses $n = 100$). A maximal energy of 4.8 mJ is reached for 20 mJ of input 1030 nm pulse energy. Generated energy of the 2.1 μm pulses is seen to increase linearly with the input 1030 nm pump energy, with an average conversion efficiency of 38%. The slight decrease in conversion efficiency indicates that the further optimization is needed to maximize the conversion at high input pump energies.

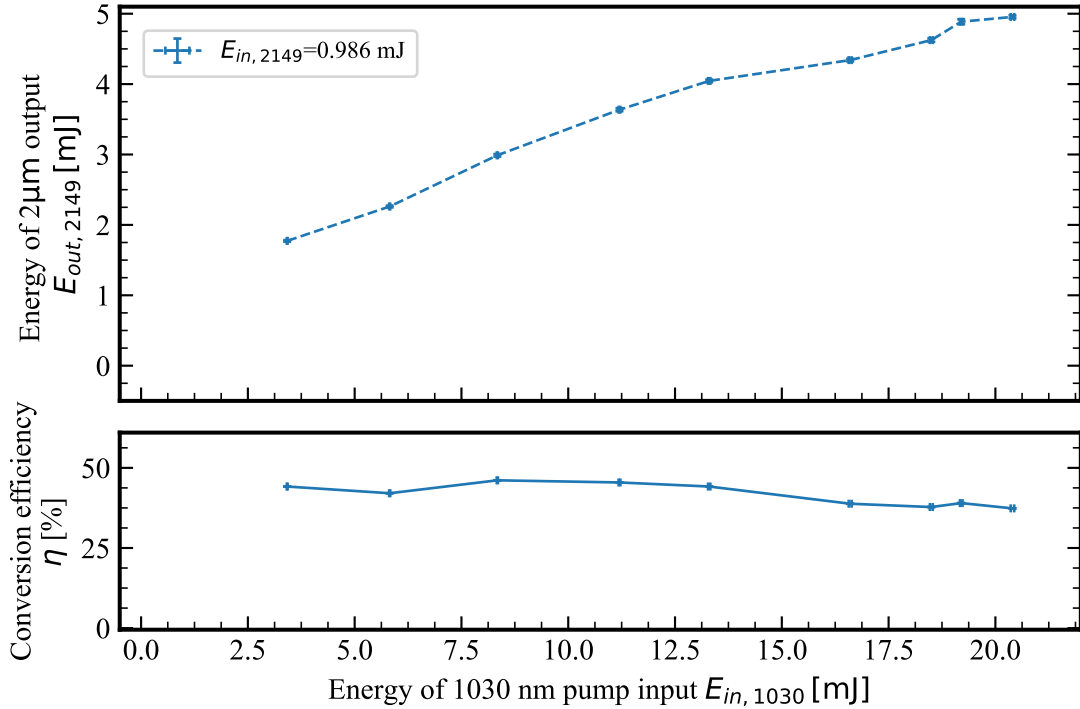


Figure 4.3: (a) Energy of the amplified 2.1 μm pulses (b) conversion efficiency of the non-linear process plotted against the energy of the input 1030 nm pump pulses of the OPA for $E_{in,2149} = 0.986$ mJ of input 2.1 μm pulse energy. The energy of 2.1 μm pulses is measured by energy meter EM2 after filtration by the dichroic mirror DCM7 (see Fig.4.1).

The energy requirement of input 2.1 μm pulse energy into the OPA for fixed energies of 1030 nm pulses is studied in Fig.4.4. The output energy $E_{out,2149}$ is seen to scale parabolically, with rapid increase for low energies of input 2.1 μm pulse energy $E_{in,2149}$ and linear dependence dominating for 300 to 600 μJ energy range. The decrease in the slope of the curve indicates the beginning of a saturation regime for even higher energies.

We characterize the spatial profile of the 2.1 μm pulses after the OPA in a scheme identical to that used in 2.1 μm -OPO (see Chapter 2). The beam is focused with a planoconvex lens, and the spatial profile (Fig.4.5) is measured with a camera (Spiricon PYROCAM IV OPHIR). A second-order polynomial in position is fitted to the square of the measured beam diameter $D4\sigma_M^2$. From this, the M^2_M along the major axis is calculated. A similar procedure is followed to extract the M^2_m along the minor axis. We evaluate the M^2 s to be $M^2_M = 1.73(28)$ and $M^2_m = 1.44(25)$, respectively. Comparing this result with

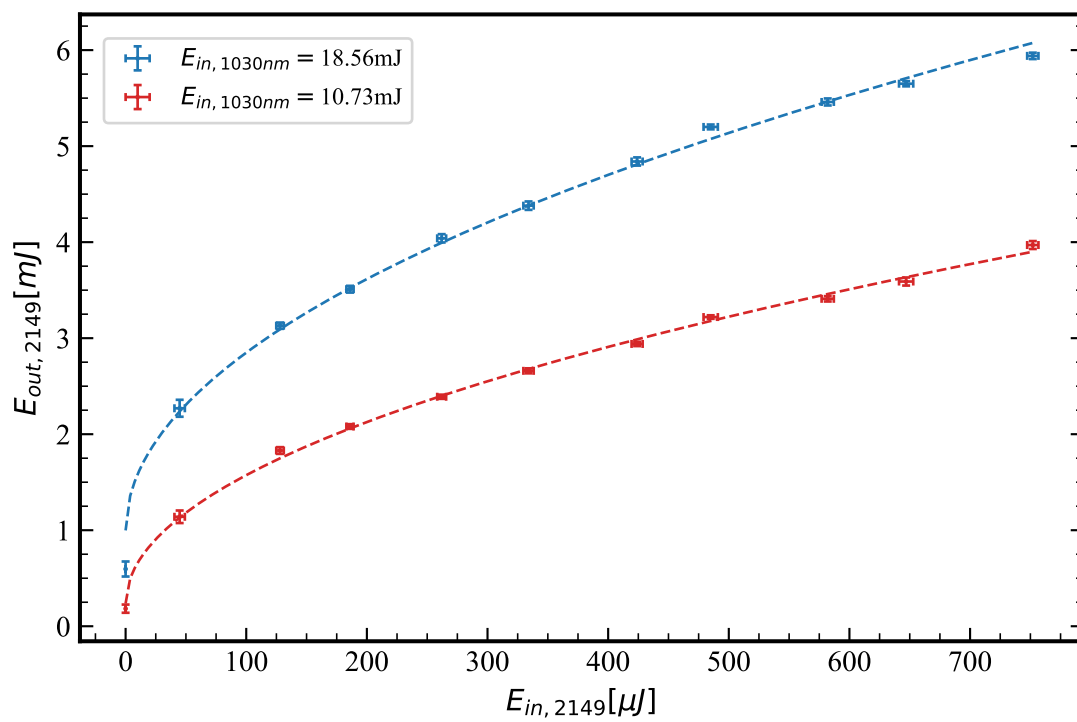


Figure 4.4: Energy of the amplified 2.1 μm pulses measured with respect to the input energy of 2.1 μm pulses from the OPO for fixed energy of 1030 nm. The energy of 2.1 μm pulses is measured by energy meter EM2 after filtration by the dichroic mirror DCM7.

$M_{M,OPO}^2 = 1.26(02)$ and $M_{m,OPO}^2 = 1.13(02)$ for the input $2.1 \mu\text{m}$ beam from the $2.1 \mu\text{m}$ -OPO and $M_{M,TDO}^2 = 1.3$ and $M_{m,TDO}^2 = 1.13$ for the 1030 nm beam from the TDO, the result is not unexpected. However, we believe that there is room for improvement.

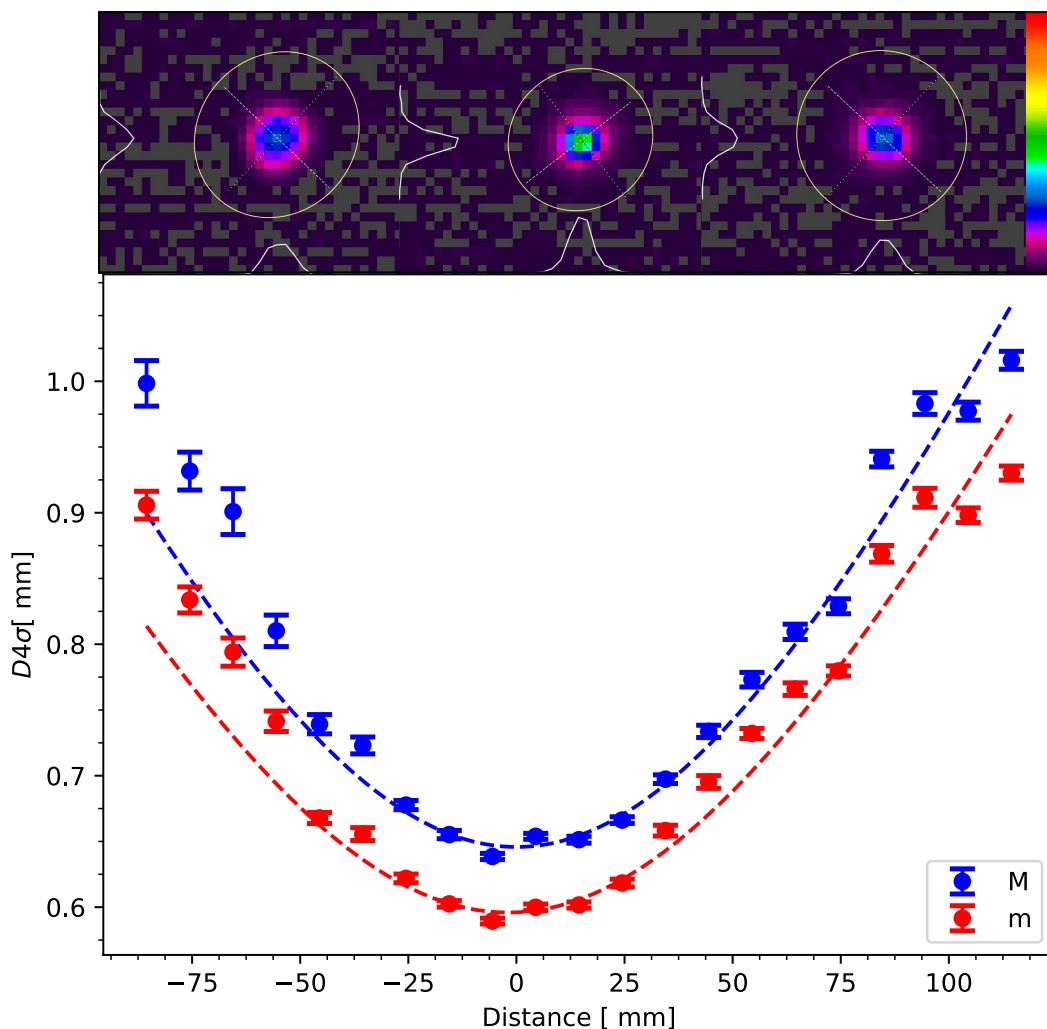


Figure 4.5: Beam quality characterization of OPA output. Variation of the beam diameter $D4\sigma_M$ and $4\sigma_m$ along the major and minor axis of the beam is plotted against the distance from the focus. The top images show the observed beam profile in far-field, near-field and far-field regimes (from left to right) as seen by the camera. The optical layout implemented is similar to that in M^2 characterization of $2.1 \mu\text{m}$ -OPO. The beam diameters $D4\sigma$ along the major and minor axis of the beam were measured, and the M^2 along the axes determined from the fit of a second-order polynomial to the data to be $M_M^2 = 1.88$ and $M_m^2 = 1.56$, respectively.

Preliminary tests with thin-disk amplifier

?? As per the design of the laser scheme, the $2.1 \mu\text{m}$ -OPA has the largest energy budget of 1030 nm pulses and must convert 175 mJ to deliver 25 mJ of $2.1 \mu\text{m}$ pulses to the subsequent $6.8 \mu\text{m}$ -DFG stage (see Sec.2.3). In this scheme (Fig.2.8), the 1030 nm pulses

of energy 30 mJ from the TDO are amplified by the thin disk amplifier (TDA) to energy >200 mJ, which are then distributed to the components of the nonlinear branch, including the 2.1 μm -OPA. Here, we report on the preliminary amplification of 2.1 μm pulses with ~ 95 mJ of 1030 nm pulses generated using the TDA.

As the TDA pulses take a similar path to the 2.1 μm -OPO and 2.1 μm -OPA and the energy budget of 1030 nm input pulses to the 2.1 μm -OPO remains unchanged, the optical layout remains mostly the same. However, to accommodate the pulse of energy 95 mJ, the Gaussian beam waist radius of the 1030 nm pulses is adjusted to be ~ 600 μm . The amplification of the 2.1 μm pulses of energy 1 mJ from the 2.1 μm -OPO by these 1030 nm pulses is reported in Fig.4.6. The plot shows that the output energy of the 2.1 μm pulses after amplification is seen to vary linearly with the input energy of 1030 nm. The conversion efficiency is also seen to remain nearly constant at $\sim 48\%$ for the measurement range. The pulse energy of the 2.1 μm beam is seen to fluctuate by $\sim 5\%$ about its mean value. This low stability is attributed to the pointing fluctuations of the TDA amplifier. While the pointing of the 1030 nm pulses from the TDO is stabilized with a quadrant photodetector before entering the TDO (see Sec.2.3.2, Fig.2.11), these pulses propagate ~ 25 m within the TDA during their amplification. As such, pointing stability deteriorates within the TDA, leading to fluctuations in the spatial overlap of the 2.1 μm pulse and the 1030 nm pulse in the 2.1 μm -OPA. A further stabilization step is necessary to obtain higher stability. However, the expected energy of the 2.1 μm -OPA of 22 mJ energy has been reached with 1030 nm pulses of 95 mJ energy.

4.1 CONCLUSION

The pulses from the 2.1 μm -OPO have been amplified to high energies in the 2.1 μm -OPA. With 1030 nm pulses of 20 mJ energy from the TDO, we amplify input 2.1 μm pulses of ~ 1 mJ energy to ~ 5 mJ energy. The high gain in the OPA allows room for decreasing the energy budget of 5 mJ the 1030 nm pulses for the OPO to ~ 3 mJ. This brings the OPO farther away from the damage threshold regime and allows for much safer operation. As the PPKTP crystal in the 2.1 μm -OPA has a higher damage threshold, the energy budget of the OPA can be increased to compensate for the reduction in energy. This ensures that the laser system can operate with high stability for the expected beam time of 8 weeks in the μH spectroscopy campaign.

Results from the characterization of conversion efficiency of the OPA when pumped with the 1030 nm pulses from the TDO indicates a decrease with increasing energy, i.e, for the current operating point, the conversion efficiency does not attain its maximum value at high pump energies. The operating point of the 2.1 μm -OPA can be fine-tuned to attain maximum conversion efficiency at high energy by increasing the beam waist w_0 of the 1030 nm and 2.1 μm beam (since input intensity $I_{\text{in}} \propto w_0^2$, see Sec.2.2). Such a scheme also has the potential to improve the beam quality and needs further study.

The preliminary tests with 1030 nm pulses of 95 mJ energy from the TDA provides a promising amplification of 2.1 μm pulses of 1 mJ energy to 22 mJ, with a conversion efficiency of 48 %. A crude extrapolation indicates that the target of 25 mJ can be reached with $\approx 25/22 \times 95$ mJ = 108 mJ energy of 1030 nm pulses. Given the design characterization of the TDA [43, 58], this estimated energy budget is easily achievable. Pending are the characterization of the beam quality M^2 of the 2.1 μm -OPA pulses after amplification with 1030 nm pulses from the TDA. The beam quality of the 1030 nm beam after the TDA to be $M^2 < 1.17$ is expected to be [58]. However, deterioration in the average beam quality is to be expected due to pointing instability exaggerated by the 25 m-internal

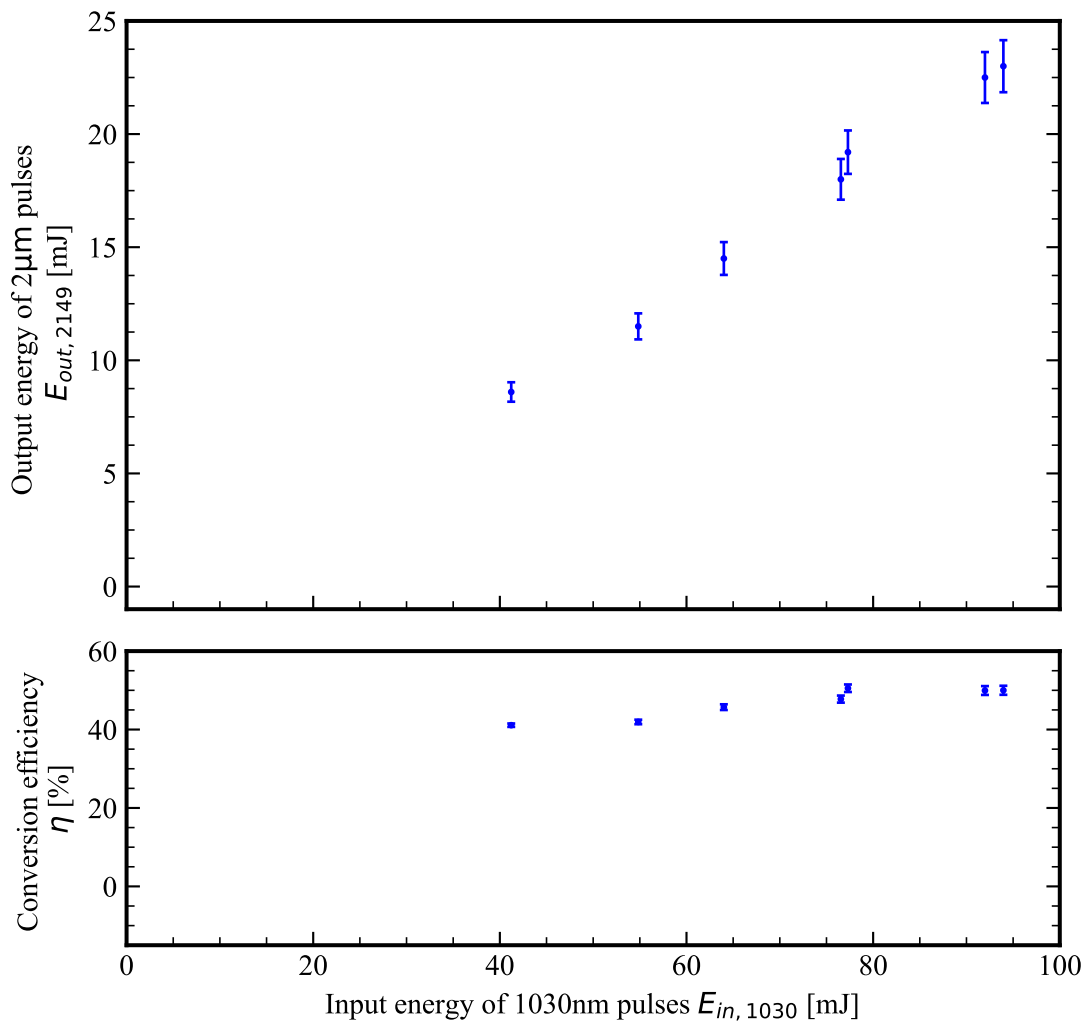


Figure 4.6: Variation of output energy of 2.1 μm pulses with input energy of 1030 nm pulses from the TDA.

propagation length of the 1030 nm within the TDA. Optimization of the TDA is currently underway to improve the pointing stability, the M^2 and the energy of the 1030 nm beam after amplification.

Thus, the 2.1 μm -MOPA branch comprising of the 2.1 μm -OPO that generates the 2.1 μm pulse and the 2.1 μm -OPA that amplifies these 2.1 μm pulses have been successfully concluded. These high energy pulses can now be used for the final step in the laser system - the difference frequency generation of 6.8 μm pulses from the 2.1 μm pulses and the 3.1 μm pulses from the 3.1 μm -OPO.

We recollect from Chapters 1 and 2 that the spectroscopy campaign requires 50 ns pulses of 3 mJ energy that are tunable in the search range of 6798 nm - 6785 nm in wavelength, or equivalently 44.1 THz - 44.4 THz in frequency. The final step in the laser system is the generation of these pulses from the difference frequency generation (DFG) of the 2.1 μm and the 3.1 μm pulses in a ZGP (Zinc Germanium Phosphate) crystal.

In this crystal, the 2.1 μm photons (pump), which have much higher energy, are converted into photons of 3.1 μm photons (signal) and 6.8 μm photons (idler).

Phase matching in ZGP

Zinc Germanium Phosphate is a positive uniaxial crystal ($n_e > n_o$) and hence has one optic axis (conventionally referred to as the c-axis of the crystal). Thus, the refractive index observed by photons of angular frequency ω that propagate with wavevector \vec{k} at angle $\theta = \cos^{-1}(\hat{k} \cdot \hat{c})$ with the c-axis \hat{c} is given by

$$\frac{1}{n_e^2(\omega, \theta, T)} = \frac{\sin^2 \theta}{n_e^2(\omega, T)} + \frac{\cos^2 \theta}{n_o^2(\omega, T)} \quad (5.1)$$

, where $n_e(\omega)$ and $n_o(\omega)$ refer to the extraordinary and ordinary refractive index of the ZGP crystal at the angular frequency ω for the temperature T of the crystal.

To achieve the difference frequency generation of pulses of 6.8 μm wavelength from pulses of 3.1 μm and 2.1 μm wavelength, we must satisfy the phase matching condition for collinear propagation through the crystal

$$\omega_{2.1} n(\omega_{2.1}; \theta, T) = \omega_{3.1} n(\omega_{3.1}; \theta, T) + \omega_{6.8} n(\omega_{6.8}; \theta, T) \quad (5.2)$$

where $\omega_{2.1} = \omega_{3.1} + \omega_{6.8}$, $\omega_{3.1}$, $\omega_{6.8}$ are angular frequencies of the 2.1 μm , 3.1 μm and 6.8 μm pulses, respectively.

The measured coefficients of the Sellmeier equation (see: Eq.2.20) can be obtained from literature values [62] to determine the required angle of propagation θ that satisfies Eq.5.2 for a specific operating temperature.

In this manner, the optimum angle of propagation of the beam for which Eq.5.2 is satisfied is calculated using SNLO at the wavelength region of interest. The obtained result is plotted in Fig.5.1 for crystal temperature of 77 $^\circ\text{C}$ and pump wavelength of 2149 nm. It is seen that two possible solutions are possible - Type I phase matching, for which the polarization of the newly generated 6.8 μm pulse is aligned parallel to that of the 3.1 μm pulse (both along \hat{x}), and Type II phase matching, for which the polarization of the 6.8 μm (\hat{y}) is normal to that of the 3.1 μm pulse (\hat{x}). While the phase matching angle for Type I phase matching is found to be 50.8 deg, that of Type II is much larger and centred around 69.68 deg.

Using the commercial software SNLO, the effective nonlinear coefficient d_{eff} for both Type I and II phase matching is determined to be

$$d_{\text{eff}}^{\text{Type-I}} \approx 81 \text{ pm/V}$$

$$d_{\text{eff}}^{\text{Type-II}} \approx 67 \text{ pm/V}$$

Thus, in regards to the higher gain offered by the larger d_{eff} for Type I, we opt to pursue Type-I phase matching with $\theta = 50.8$ deg at crystal temperature 77°C .

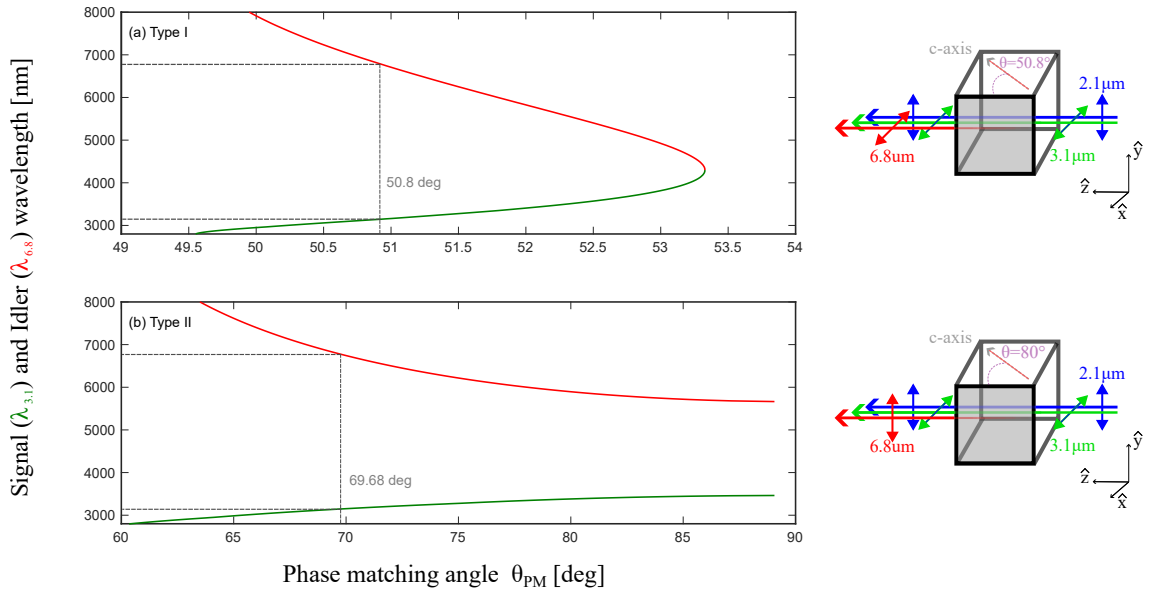


Figure 5.1: Idler and signal wavelength as a function of the phase matching angle simulated with SNLO for fixed pump wavelength of $\lambda_p = 2149 \text{ nm}$ for (a) Type I and (b) Type II phase matching in ZGP at a temperature of 77°C . The corresponding polarization orientation is illustrated to the right of the plot.

5.1 TECHNICAL IMPLEMENTATION

The implemented optical layout is portrayed in Fig.5.2. Like the $2.1 \mu\text{m}$ pulse generated in the $2.1 \mu\text{m}$ OPO, the $3.1 \mu\text{m}$ pulses and $2.1 \mu\text{m}$ pulses from the OPOs are s-polarized (\hat{y}).

To achieve Type-I phase matching, the polarization of the $3.1 \mu\text{m}$ pulses must be rotated to be normal (p-polarization, along \hat{x}) to that of the $2.1 \mu\text{m}$ pulse. To this extent, a periscope is designed. The periscope begins with a mirror PM1 that reflects the beam in vertical direction from 75 mm to 125 mm . The second periscope mirror PM2 sends the beam horizontally again but alters the polarization of the pulse with respect to the $2.1 \mu\text{m}$ pulse as the plane of incidence for this propagation is normal to the plane of incidence of the optical system so far (which was essentially the plane of the optical table). The mirror PM3 reflects these pulses into another periscope (mirrors PM4 and PM5) that brings them back to the required beam height of 75 mm .

The $3.1 \mu\text{m}$ pulses from the $3.1 \mu\text{m}$ -OPO are pre-collimated before passing the lenses $f_4=500 \text{ mm}$ and $f_5=250 \text{ mm}$ focusing the beam onto the crystal with a beam waist of

347 μm . The 2.1 μm pulses from the 2.1 μm -OPA are first collimated with the lens $f_1=500$ mm before the filtering optics for removing 1.9 μm (as described in section). To obtain the correct beam waist, the pulses pass through a telescope of lenses $f_2=200$ mm (LA5714-D, Thorlabs) and $f_3=-75$ mm (LC5401-E1, Thorlabs). Like the 3.1 μm pulses, they go through the lens $f_5=250$ mm such that the focus is at the middle of the ZGP crystal with a waist of 312 μm .

The ZGP crystal ($6\times 6\times 12$ mm³ dimension, $\theta = 50.8$ deg, $\phi = 0$ deg, BAE Systems) is mounted on an oven with a copper holder. The copper holder is temperature-stabilized with a Peltier element, the cold side of which is in contact with a water-cooled brass block.

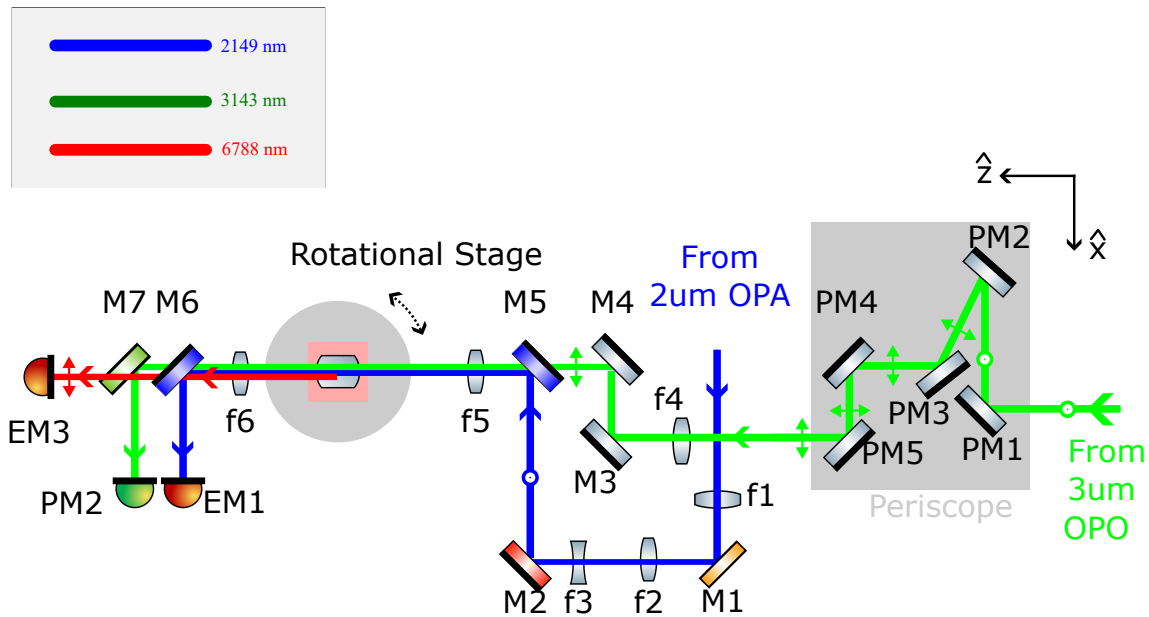


Figure 5.2: Optical Layout for DFG scheme where 2.1 μm (blue) and 3.1 μm (green) pulses generate 6.8 μm pulses (red). A periscope rotates the polarization of the 3.1 μm pulses from s-polarization (\hat{y}) to p-polarization (\hat{x}). The ZGP Crystal is housed in a home-built oven, mounted on a rotational stage, that can be rotated along the \hat{y} axis. The generated 6.8 μm pulses are filtered out using long-pass filter M6 and M7.

5.2 CHARACTERIZATION

The 6.8 μm pulse generated from the DFG and the 3.1 μm pulses is separated from the 2.1 μm pulse by the dichroic mirror M6. The energy of the depleted 2.1 μm pulse is measured by energy meter EM1. The dichroic mirror M7 filters the 6.8 μm pulse while reflecting the 3.1 μm pulses into power meter PM2. The energy of the 3.1 μm pulses is obtained from the measured average power and the repetition rate (20 Hz). Energy meter EM3 measures the energy of the 6.8 μm pulses.

Phase matching bandwidth

The optimum phase matching condition depends on three parameters - frequency ν_{6788} , or equivalently the wavelength $\lambda_{6.8}$ of the 6.8 μm pulses, temperature T of the crystal and the angle of orientation θ of the crystal w.r.t. the incident 2.1 μm and 3.1 μm pulses. For a

given wavelength $\lambda_{6,8}$, deviation from the optimum value of temperature or orientation causes the three pulses to experience refractive indices within the crystal that do not perfectly satisfy Eq.5.2. This causes the energy of the 6.8 μm pulses to fall from the maximum value as approximately described by a Sinc^2 function (See Chapter 2, Sec.2.2).

We recollect here that the frequency ν_{67xx} can be determined using Eq.2.58 by measuring the frequency ν_{15xx} of the 1532 nm-seed laser that injection-seeds the 3.1 μm -OPO and frequency ν_{1979} of the 1979 nm-seed laser that injection-seeds the 2.1 μm -OPO (see Sec.2.3.4) as $\nu_{67xx} = \nu_{15xx} - \nu_{1979}$. Tuning the frequency ν_{67xx} (by controlling ν_{15xx}), changes the optimum value of T and θ for which phase-matching condition is met.

Figure 5.3 shows the variation of the energy of the 6.8 μm pulses with the angle of orientation of the crystal at constant temperature $T=80^\circ\text{C}$ for three different wavelengths. The fit of the function

$$\eta(\theta) = \eta(\theta_0) \text{Sinc}^2 \left(0.886 \frac{\theta - \theta_0}{\Delta\theta} \right) \quad (5.3)$$

to the data yields the phase matching bandwidth at a FWHM of $\Delta\theta=1.72$ deg for all three wavelengths. The optimum value of the phase matching angle θ_0 is plotted against the wavelength in Fig.5.4. A minimal variation of 0.05 deg for every 10 nm increment in wavelength $\lambda_{6,8}$ is observed. On tuning the wavelength from 6784 nm to 6823 nm, the 6.8 μm suffers only <5% energy loss. These results indicate that the phase matching of the DFG process is tolerant within the search range 6798 nm - 6785 nm of the HFS in μH , even without changing the angle at the same crystal temperature, while a much larger range is accessible by tuning θ .

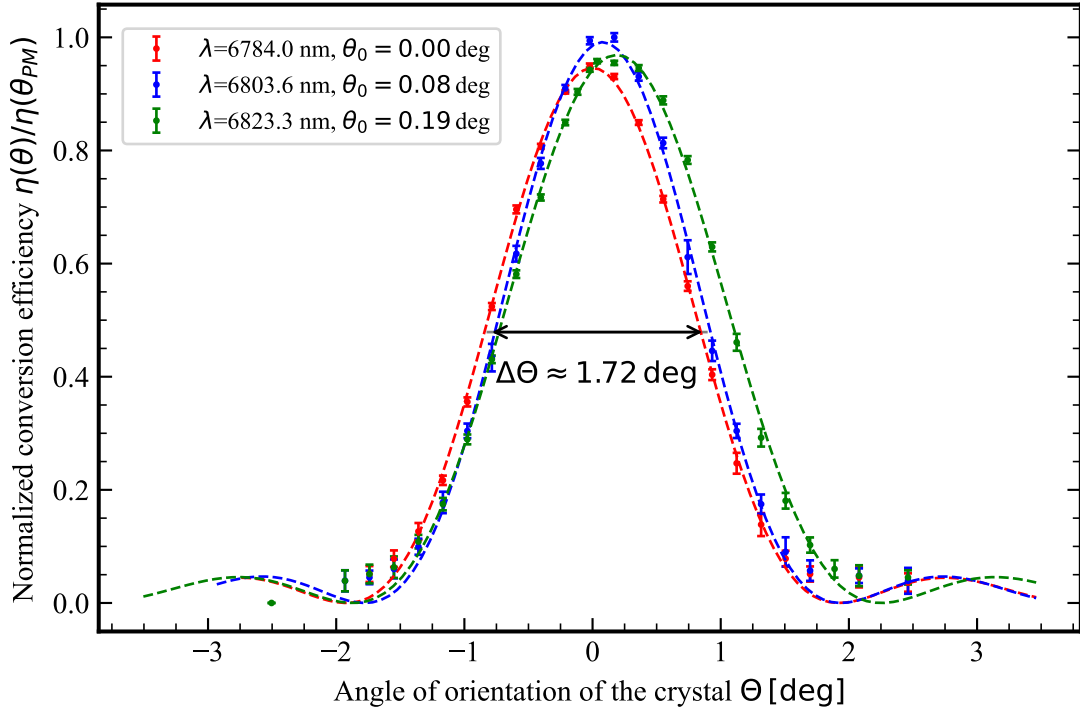


Figure 5.3: Variation of the normalized conversion efficiency of the 6.8 μm -DFG stage with respect to the crystal orientation for various wavelengths. The crystal temperature is stabilized to 80°C .

The energy of the generated idler pulses is measured at fixed wavelength versus the

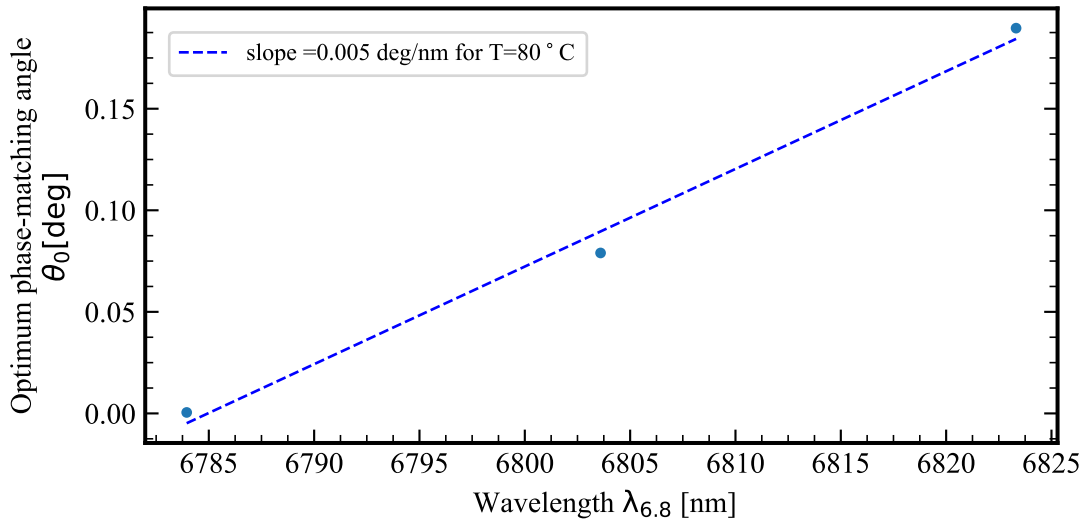


Figure 5.4: Measured optimum phase matching angle versus wavelength obtained from the fit to the data in Fig.5.3 is plotted against the corresponding wavelengths. Linear fit yields a slope 0.005 deg/nm

angle θ for two temperatures $T=60^\circ\text{C}$ and 80°C . Varying the crystal temperature by 20°C is seen to decrease the energy by $<5\%$. This means that the DFG system can be operated much closer to the room temperature, thereby reducing thermal fluctuations and heat gradient in the laser system, with negligible efficiency losses.

Variation of the optimum phase matching angle with temperature is shown in Fig.5.5. The optimum phase matching angle is seen to rise by 0.018 deg for every 1°C increment in temperature from the linear fit. The product of the slopes of the linear fits in Fig.5.3 and Fig.5.5 allow us to approximate the variation of optimum phase matching temperature with wavelength $\frac{\partial T}{\partial \lambda_{6.8}} = \left(\frac{\partial T}{\partial \theta}\right) / \left(\frac{\partial \theta}{\partial \lambda_{6.8}}\right) \approx 0.28^\circ\text{C nm}^{-1}$. Thus, the phase matching for the DFG can be adjusted by minimal adjustment of the crystal temperature for the given wavelength.

These results also indicate that the DFG process can be further optimized by tuning the temperature of the crystal to shift the optimum phase match angle rather than mechanically rotating the crystal to tune its orientation. This provides us with a more precise control of the conversion efficiency at a given wavelength, which significantly simplifies the laser control system.

Energy characterization and conversion efficiency

Figure 5.7 shows the variation of the idler output energy with that of the input pump pulses at the $2.1\ \mu\text{m}$ wavelength for two input energies of signal pulses at the $3.1\ \mu\text{m}$ wavelength. Note that $\sim 10\%$ of the energy of the incident $2.1\ \mu\text{m}$ pulse is lost due to the absorption band of the ZGP crystal near $2.1\ \mu\text{m}$. The energy of the $2.1\ \mu\text{m}$ pulses was limited to 6.1 mJ during the characterization campaign to avoid damaging the crystal. The energy of the idler pulses is seen to saturate after 5 mJ of input pump energy. The saturation region of the nonlinear process has a characteristically lower slope and hence is less prone to fluctuations in the energy of the $2.1\ \mu\text{m}$. This regime is ideal for long-term operations such as our spectroscopy campaign. However, an earlier saturation also

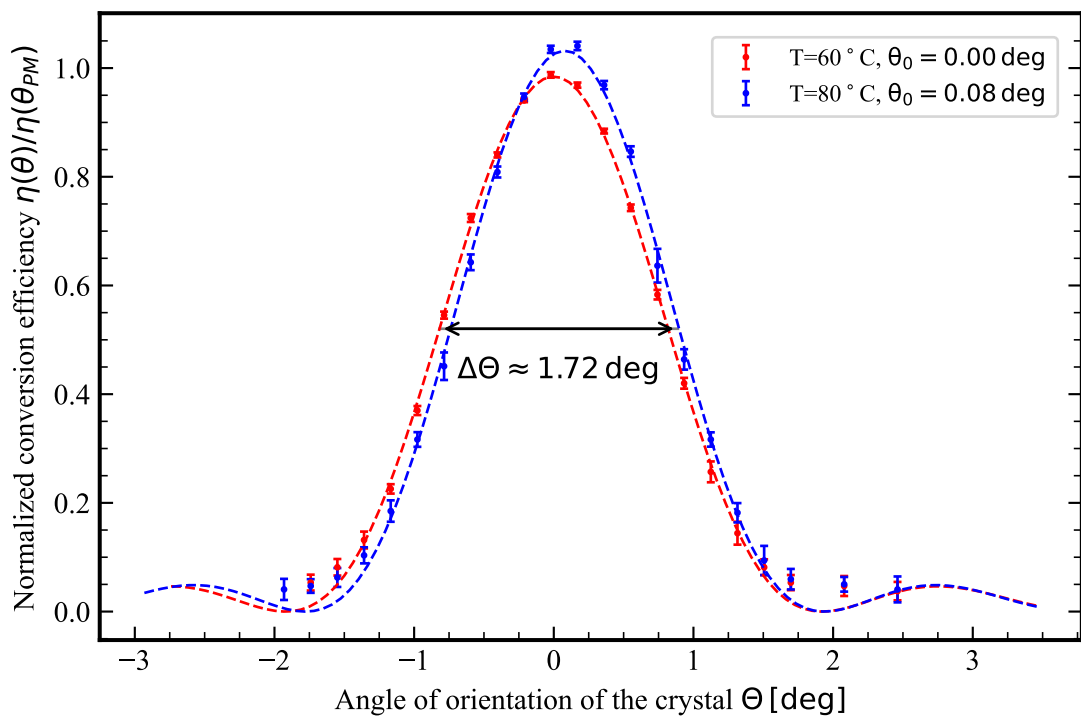


Figure 5.5: Normalized conversion efficiency of the 6.8 μm -DFG stage with respect to the crystal orientation for two crystal temperatures. The idler wavelength is kept fixed at 6782 nm.

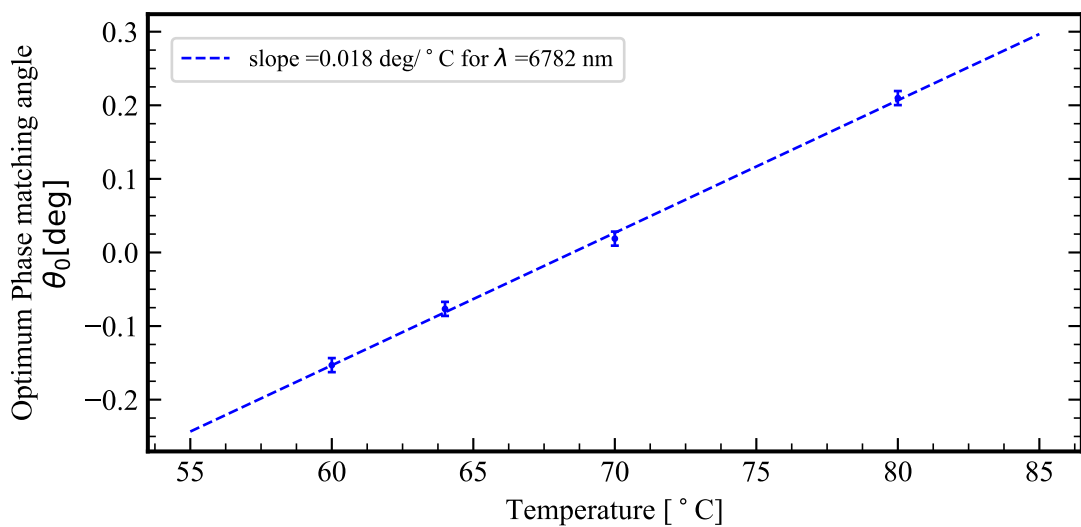


Figure 5.6: Optimal orientation of the ZGP crystal for phase matching at different temperatures.

implies a lower maximum energy. Here, for 297 μJ of 3.1 μm with 6.1 mJ of 2.1 μm pulses, we reach a maximum of $\sim 300 \mu\text{J}$ at 6.8 μm wavelength, roughly one-tenth of the energy requirement for μH spectroscopy. Therefore, further study and optimisation of the DFG process are necessary before the spectroscopy campaign.

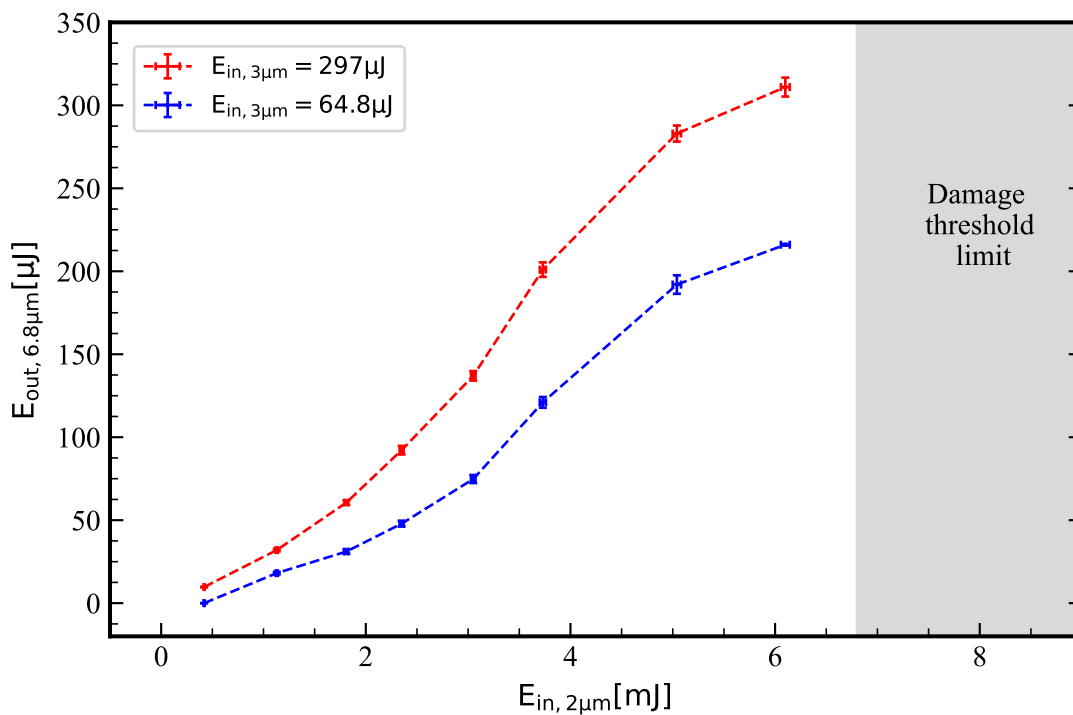


Figure 5.7: 6.8 μm idler pulse energy at 6.8 μm from 10 cm long ZGP crystal at 50 $^{\circ}\text{C}$ versus pump energy at 2.1 μm wavelength for two signal energies at 3.1 μm wavelength. Beam waist 312 μm sets the damage threshold regime to begin at 6.8 mJ of total input energy (See Table.2.1).

Similarly, we study the variation of energy of 6.8 μm with that of the 3.1 μm in Fig.5.8 for two different 2.1 μm input pulse energy. Here, the \tanh^2 -function fits the data well, and saturation of the 6.8 μm is seen to start for 200 μJ of 3.1 μm . Thus, the energy of the 6.8 μm is well-insulated from fluctuations in the energy of the 3.1 μm pulses.

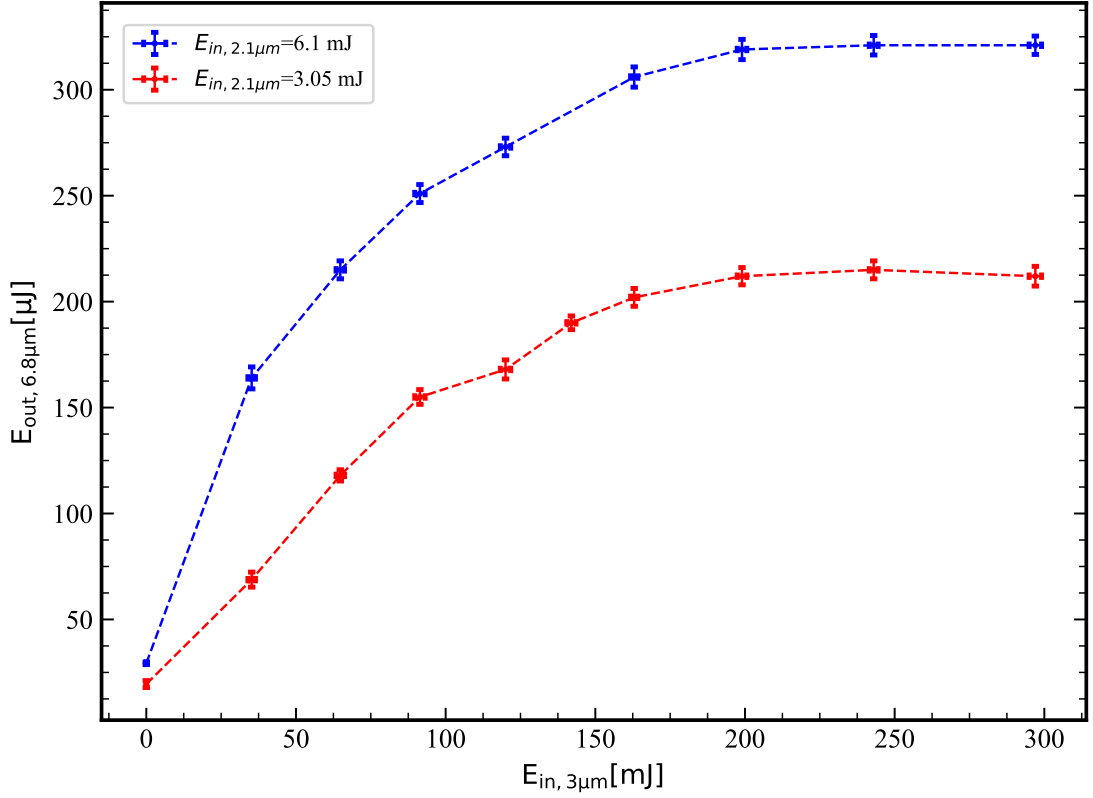


Figure 5.8: 6.8 μm idler pulse energy as a function of the signal pulse energy at 3.1 μm wavelength two pump energies at 2.1 μm wavelength. The 10 mm long ZGP crystal was stabilized to 50 $^{\circ}\text{C}$.

The conversion efficiency η of the process is defined as

$$\eta = \frac{E_{out,6.8\mu m} + E_{out,3\mu m}}{E_{in,2\mu m}} \times 100\% \quad (5.4)$$

and is plotted in Fig.5.9. The conversion efficiency is seen to be $\sim 18\%$ for the maximum input energy at 2.1 μm wavelength of 5 mJ and 3.1 μm wavelength of 297 μJ . This efficiency must be comparable to the maximum efficiency of 38% obtained from SNLO simulations (See Fig.2.10). It is important to note the results here are preliminary and have significant room for improvement. Additionally, the maximum possible energy of 2.1 μm pulses is limited as the laser system uses 1030 nm pulses of energy ~ 30 mJ from the TDO without amplification from the TDA. Higher energies of 2.1 μm pulses are expected to be reached in the scheme of the whole laser system, which expects to use 1030 nm pulses of 200 mJ energy, leading to the target of 3 mJ energy at 6.8 μm wavelength. (See.2.3).

Spatial and temporal profile characterization

Following the same procedure as in Chapters 3 and 4, we measure the beam diameters $D_{4\sigma_M}$ and $4\sigma_m$ at various positions along the beam propagation of the 6.8 μm beam. The measurements are shown in Fig. 5.10. A second-order polynomial is fitted to the data to determine the M^2 of the 6.8 μm pulses. The M^2 along the major axis and minor axis are found to be $M_{M}^2 = 1.60(14)$ and $M_m^2 = 1.39(0.05)$. Observably, these values must be

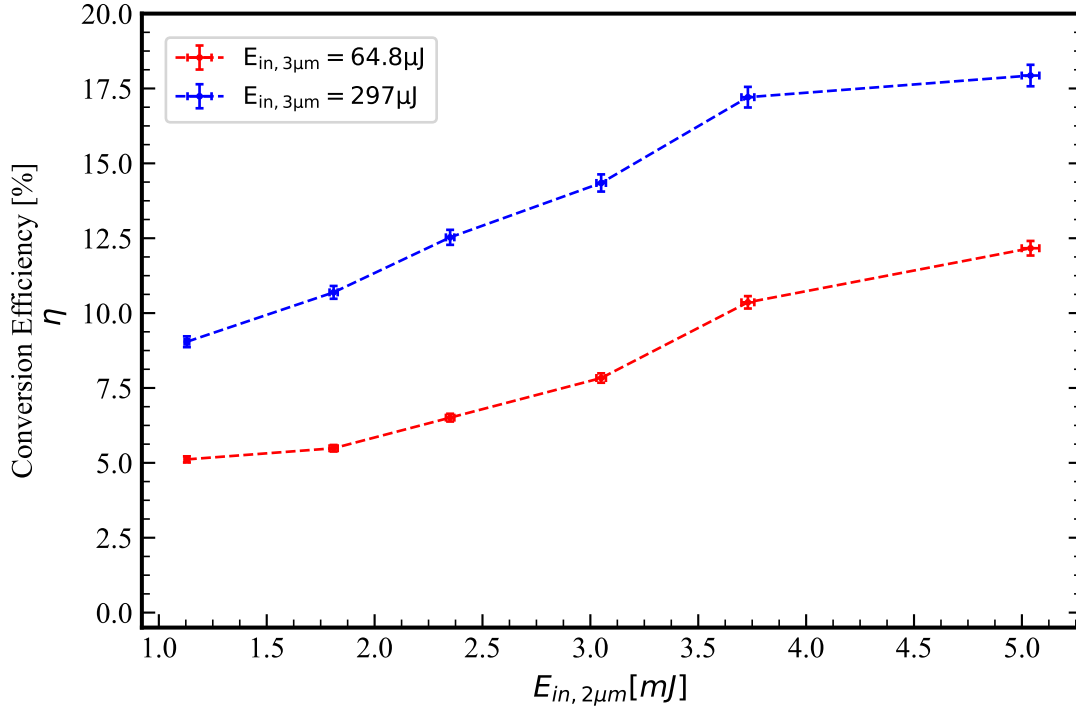


Figure 5.9: Conversion efficiency of the 6.8 μm -DFG stage versus the energy of 2.1 μm pump pulses for two input signal energy at 3.1 μm wavelength.

treated conservatively as the fit is not seen to describe the beam diameters of the major axis of the beam while being adequate to describe the minor axis beam diameter. This indicates that the spatial profile of the 6.8 μm pulse could be effectively complicated by astigmatic effects in the parent 2.1 μm and 3.1 μm pulses or the effect of walk-off of pulses propagating through the crystal.

Figure.5.11 shows the spatial profile of the 6.8 μm pulse observed in the Pyrocam where the cross-hair denotes the centroid of the spatial profile, as determined from the commercial software. To characterize the pointing fluctuations of the 6.8 μm pulses with time, the position of the centroid of the beam is recorded for one hour. The fluctuation of the horizontal and vertical coordinates of the centroid from their respective average values is plotted in Fig.5.12 and the corresponding histogram to the right of the plot. We recollect here that the laser pulses are first generated in the TDO, where their centroid is stabilized with a quadrant photodetector (see Sec.2.3.2, Fig.2.11). From the TDO, the pulses propagate >6 m in the nonlinear downconversion stage, ending with the DFG of 6.8 μm . The measurements indicate that the fluctuations of the centroid are $< 1\%$, despite the long beam path of the pulse. While it is expected that the pulses must travel a further distance of ~ 15 m from the DFG setup to the beamline for μH spectroscopy, it is clear that the current auto-alignment system implemented in the TDO is able to stabilize the position of the pulse. Only an additional auto-alignment on the 6.8 μm pulses is needed to compensate for the 15 m path.

Figure 5.13 shows the temporal profile of the intensity of the 6.8 μm pulse, as measured with a photodetector of 1 GHz bandwidth. Also shown are the pulses from the TDO, 2.1 μm -OPO, 2.1 μm -OPA and 3.1 μm -OPO. Compared to the 1030 nm pulse from the TDO of 48 ns FWHM, each stage of nonlinear downconversion shortens the pulse.

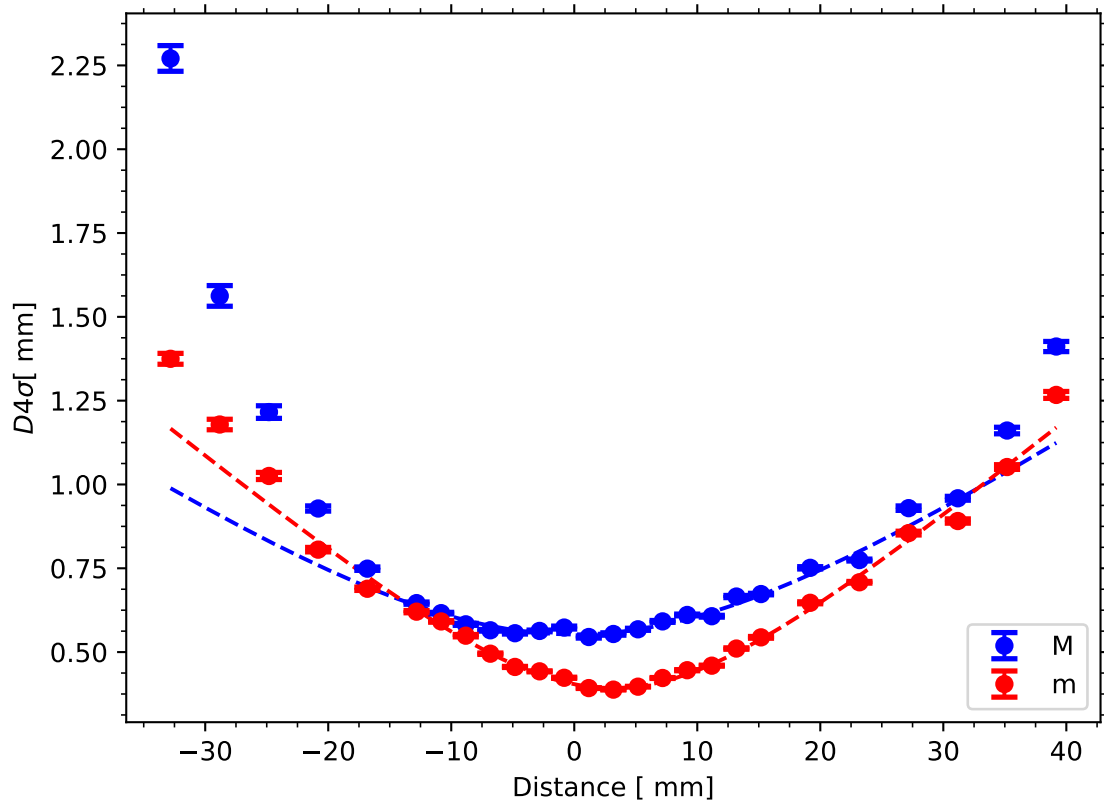


Figure 5.10: M^2 measurement of the $6.8\ \mu\text{m}$ beam from the $6.8\ \mu\text{m}$ -DFG stage. Variation of the beam diameter $D4\sigma_M$ and $4\sigma_m$ along the major and minor axis of the beam is plotted against the distance from the focus. The pulses were measured using Spiricon PYROCAM IV OPHIR, triggered synchronously to the laser pulses.

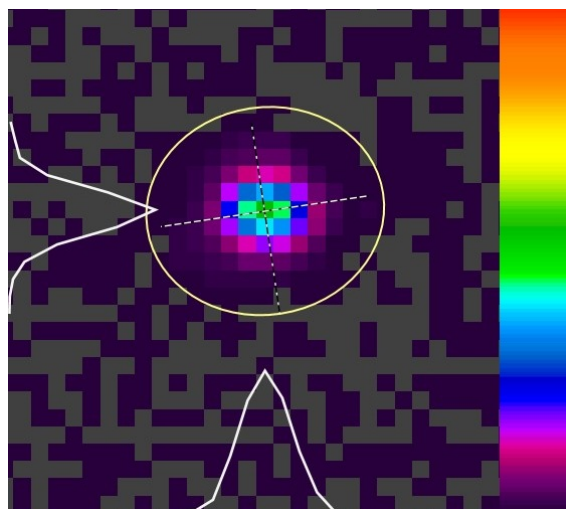


Figure 5.11: Spatial profile of the DFG pulse as taken with Pyrocam. Cross-hair denotes the centroid as determined by the camera

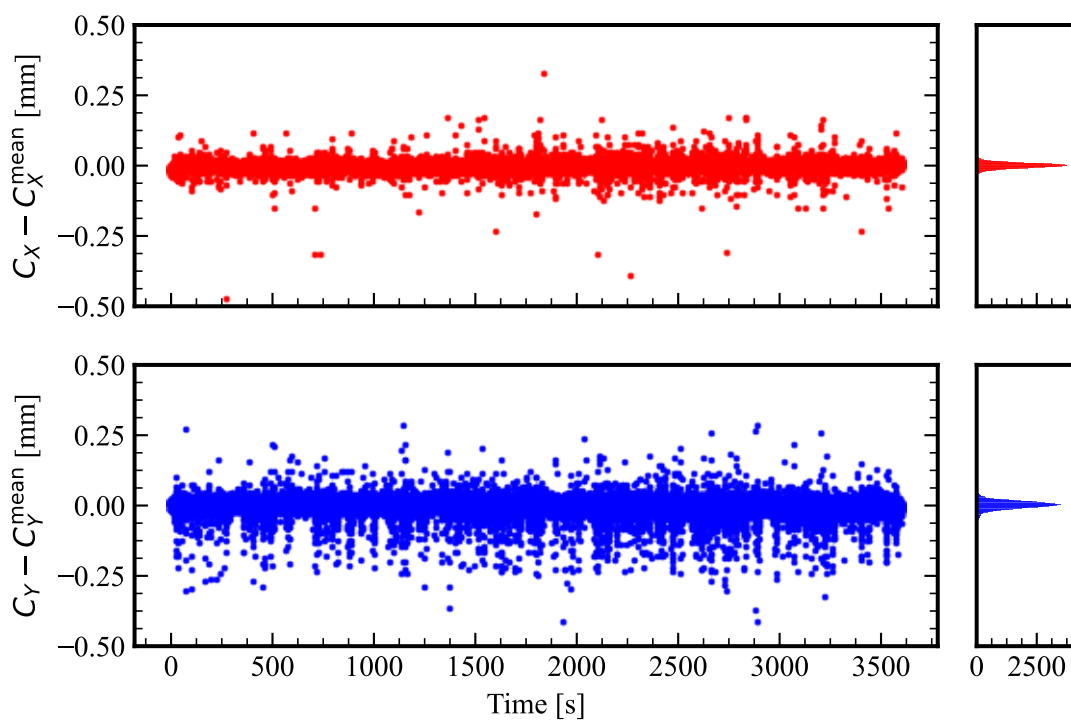


Figure 5.12: Pointing stability measurement of the $6.8\ \mu\text{m}$ pulses over time with Spiricon PYROCAM IV OPHIR. The Centroid in the x and y direction is monitored over the course of 1 h. Relative deviation in percentage is plotted against time in seconds.

While the 6.8 μm pulse is generated from the 2.1 μm pulse and hence is expected to have an FWHM less than the 2.1 μm pulse, it is seen to be 4 ns larger than the latter. The cause of this is likely due to the modulation of time period 12 ns that is present in the parent TDO pulse. This modulation, which comes from the round-trip loss of energy of the intracavity field in the TDO, complicates the extraction of a reliable FWHM.

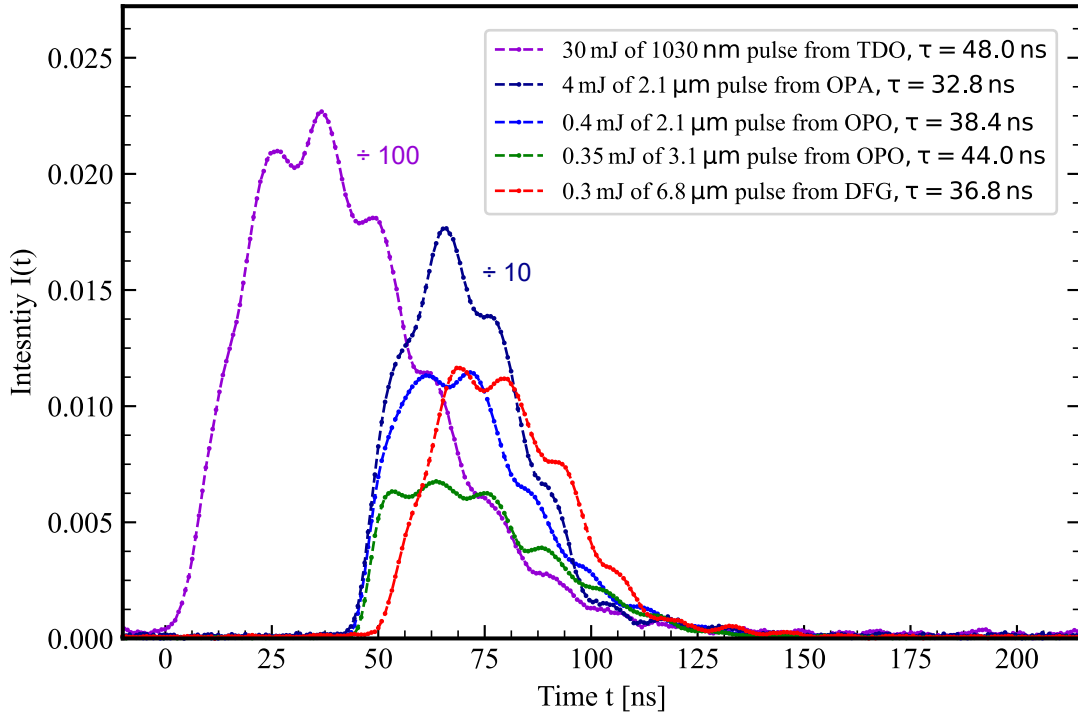


Figure 5.13: Temporal intensity of the pulses from TDO, 2.1 μm -OPO, 2.1 μm -OPA, 3.1 μm -OPO and the 6.8 μm -DFG stage as measured with a VIGO photodetector. Note that the area of the pulses corresponds to their energies. To allow for comparison, the amplitude of the pulse from TDO and 2.1 μm -OPA have been scaled by 100 and 10, respectively.

To better understand the pulse shortening in the nonlinear downconversion process, the FWHM of pulses from 2.1 μm -OPO, 2.1 μm -OPA and 3.1 μm -OPO are measured for TDO pulses of different FWHM but same energy of 30 mJ (see Fig.5.14). Thus, to achieve the required energy of 3 mJ at a longer pulse duration of 50 ns, the pulses from TDO must be longer, and the nonlinear DFG process in each stage must be more efficient.

5.3 CONCLUSION

Since the commencement of the *HyperMu*, the 6.8 μm -DFG stage has been realized, and pulses at 6.8 μm wavelength have been generated. A conversion efficiency of 18% for an input 2.1 μm pump energy of 6.1 mJ was realized in the preliminary operation of the 6.8 μm -DFG stage. We recollect here that the amplification of 2.1 μm pulses to 22 mJ energy was demonstrated (see Sec.??). Assuming this conversion efficiency of the 6.8 μm -DFG stage to be 18% and we expect to convert $22\text{ mJ} \times 18\% = 3.96\text{ mJ}$ of 2.1 μm into 6.8 μm and 3.1 μm pulses. This corresponds to the generation of 6.8 μm pulses of 1.25 mJ en-

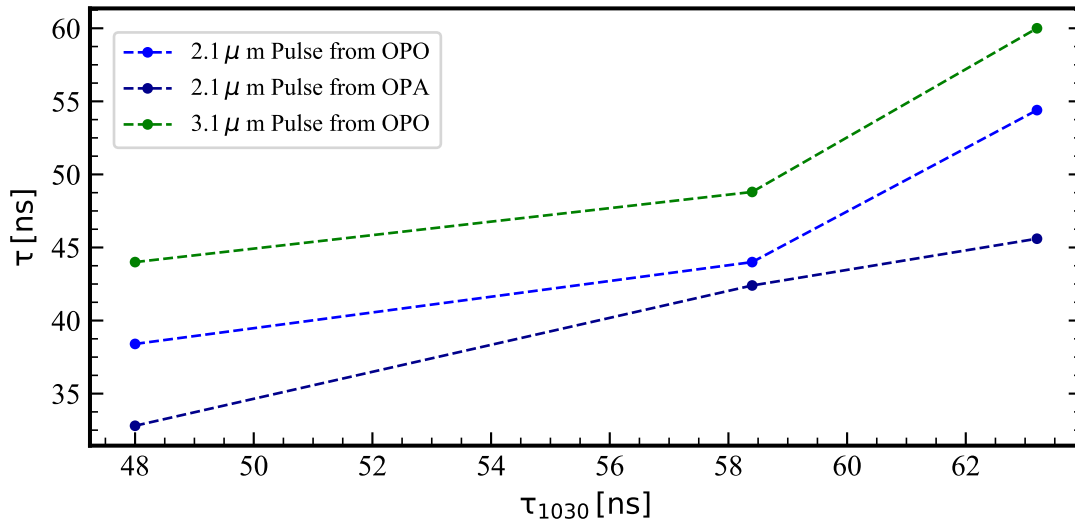


Figure 5.14: FWHM of the waveform of the pulses 2.1 μ m-OPO, 2.1 μ m-OPA, 3.1 μ m-OPO for the variation of the TDO pulse length. Lines are only there to guide the eyes.

ergy¹. Thus, at the current capacity of the laser system, the generation of pulses with >1 mJ energy at 6.8 μ m wavelength is possible, which satisfies the minimum criteria for the Hypermu experiment (see Tab.1.2). The laser system, designed to generate pulses of 3 mJ energy at 6.8 μ m wavelength, will merit from the upcoming improvements in optimization of conversion efficiency of the 6.8 μ m stage and implementation of the TDA that allows for energy scaling.

Currently, the FWHM of the temporal intensity profile is determined to be ≈ 37 ns, around 13 ns shorter than the design pulse duration of 50 ns (see Chapter 1). This result, along with our energy budget, indicates that we must generate pulses of 1030 nm with FWHM greater than 50 ns at energies of 100 mJ to obtain 3 mJ of 6.8 μ m pulses with pulse width 50 ns. Pulse duration and energy scalability of the TDO pulses studied in [43] indicates that this is indeed feasible by controlling the voltage on the Pockel's cell and extracting the pulses for larger build-up times.

Temperature and wavelength dependence of the phase-matching studies indicate that the phase-matching bandwidth is sufficiently broad, similar to other nonlinear processes described in the thesis. Optimization of the DFG process for a given wavelength of 6.8 μ m pulses by shifting the crystal temperature allows us to conveniently maximize the energy of the 6.8 μ m during the future spectroscopy campaign on the μ H. Moreover, even without this fine-optimization, we see little drop in energy within the search range of 6798 nm - 6785 nm.

While the preliminary result on the M^2 of the 6.8 μ m pulse looks promising, further optimization is required. As the next stage in the experimental scheme is the in-coupling of the generated 6.8 μ m pulses into the toroidal multipass enhancement cell, a minimal deviation of M^2 from unity is ideal for the μ H spectroscopy campaign. The deviation of the beam diameter $D4\sigma_M$ of the major axis from the expected $D4\sigma$ of the Gaussian beam can be attributed to higher-order aberrations and walk-off problems within the

¹Since $E = nhc/\lambda$ and the number of converted 2.1 μ m photons equal the number of generated 6.8 μ m photons.

ZGP crystal. This must be further studied by characterizing the energy and the spatial profile of the $6.8\ \mu\text{m}$ for different beam waists of the parent $2.1\ \mu\text{m}$ and $3.1\ \mu\text{m}$ pulses. Further optimization of the current system and scaling of the energy and pulse duration is expected to be concluded prior to the μH spectroscopy campaign.

As described in Chapter 1, a search range of 44.1 THz - 44.4 THz for the resonance of the HFS transition in μH is obtained from theoretical considerations. To determine the resonance frequency of the transition up to a precision of 1 ppm, laser pulses with a well-controllable centre frequency (known to <40 MHz) that are calibrated within the search range of the resonance are necessary. Moreover, simulations on laser excitation probability of the HFS transition have shown that 6.8 μm pulses of lower spectral bandwidth (FWHM) reduce the time it takes to obtain a signal with a significance of 4σ over background for the same pressure of the H_2 (see Chapter 1). For example, reducing the bandwidth of the 6.8 μm pulses from 100 MHz to ~ 10 MHz reduces the time needed by a factor of $\sim 50\%$ for the spectroscopy campaign. A transform-limited Gaussian pulse [63] has a Gaussian spectral profile whose FWHM is given by $\delta\nu_{\text{TL}} = \frac{2}{\pi} \log(2)/\tau$. For pulses of duration 30 ns, this corresponds to a bandwidth of 14.7 MHz. As our pulses are not seen to be Gaussian in the time domain, we expect a much broader bandwidth. Thus, characterisation of the spectral profile of the 6.8 μm pulses is needed prior to spectroscopy in μH .

The frequency ν_{67xx}^1 of the 6.8 μm pulses is set by the frequency ν_{15xx} of the 1532 nm-seed laser and the frequency ν_{1979} of the 1979 nm-seed laser (see Chapter 2, Sec.2.3.4) as $\nu_{67xx} = \nu_{15xx} - \nu_{1979}$ (Eq.2.58). We recollect from Chapter 2 here that the frequencies ν_{15xx} and ν_{1979} are measured with a statistical uncertainty of 1 MHz and a systematic uncertainty of 10 MHz by the wavelength meter. This implies that the systematic uncertainty on the frequency ν_{67xx} of the 6.8 μm pulses is $\sqrt{10^2 + 10^2} \sim 14$ MHz. Thus, calibrating the centre frequency ν_{67xx} of the 6.8 μm pulses against a well-known reference frequency in the search range is necessary to constrain the systematic uncertainty.

A simple method for determining the laser bandwidth is through absorption spectroscopy of atoms or molecules. Absorption spectra of atoms and molecules appear broader when measured with laser pulses of finite bandwidth. The laser bandwidth can then be extracted by comparing the measured linewidth of the spectrum with the expected width of the transition and accounting for other line-broadening effects.

Laser bandwidth characterization schemes

While there are multiple methods to determine the bandwidth of laser pulses, notable ones involve optical heterodyne measurement [64], or a Fabry-Perot cavity [65, 66], or with atomic or molecular spectroscopy. Fig.6.1 presents a simplified layout of these three bandwidth characterization methods.

Optical heterodyne measurement (Fig.6.1-a) involves analyzing the beat note between the output from a reference laser and the 'laser-under-test'. The reference laser must have a well-characterised spectral profile bandwidth. Moreover, its centre frequency must be

¹'xx' in the index indicates that the wavelength can be tuned

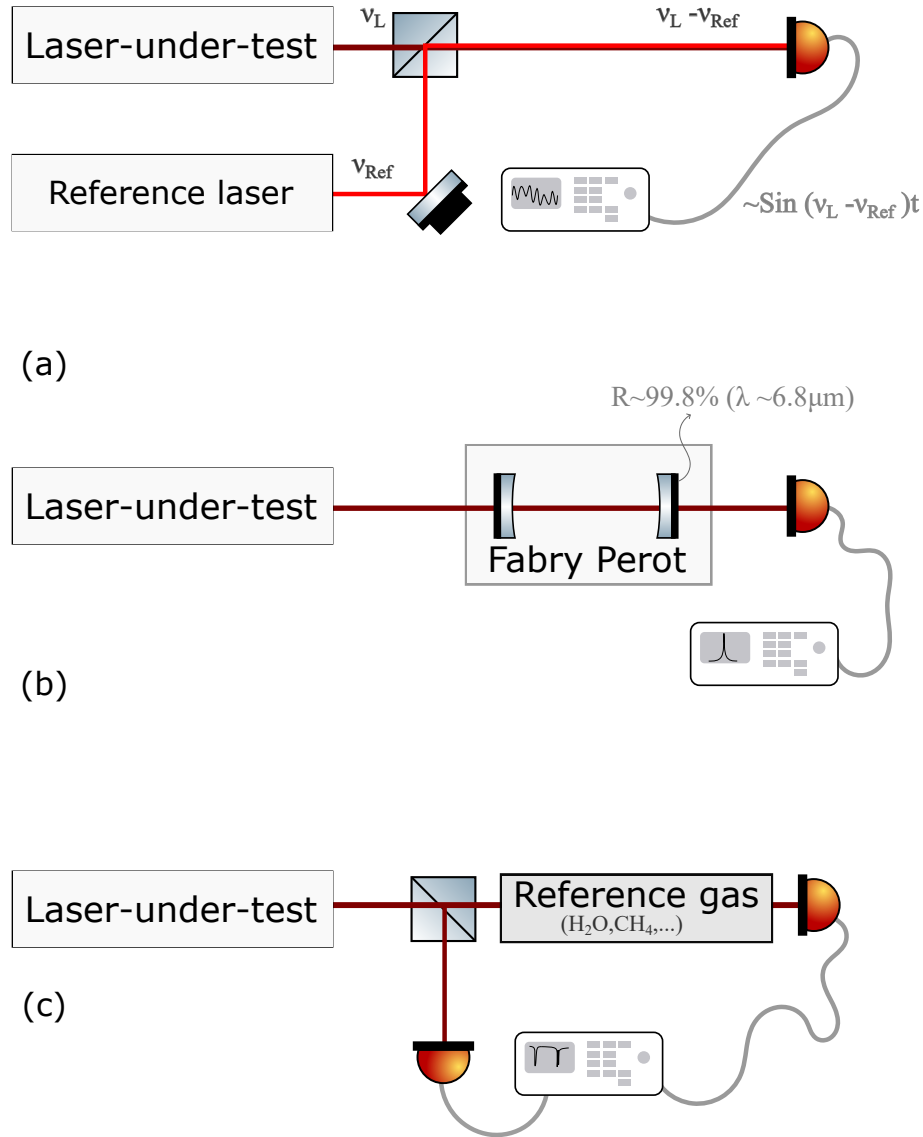


Figure 6.1: Schematic of three frequency calibration methods for pulsed lasers. (a) Optical heterodyne detection: laser bandwidth is obtained by analysing the beat note between the laser-under-test (dark red) and a reference laser (light red) with an RF spectrum analyser or an oscilloscope. (b) Fabry-Perot cavity: pulses from the laser-under-test are sent to a calibrated narrow linewidth Fabry-Perot cavity. The cavity transmission profile is measured for different cavity lengths and analysed to determine the bandwidth. (c) Reference gas absorption spectroscopy: The absorption spectrum of a reference gas is measured using the laser-under-test. Laser bandwidth is determined by comparing the measured laser-broadened spectrum and the expected spectrum.

close, by say ~ 1 GHz, to the frequency of the 'laser-under-test' to generate a beat note which is detectable by a commercial photodiode. The light from the reference laser is superimposed with the light from the laser-under-test onto a photodetector of sufficient bandwidth, and the power spectrum of the photodiode is measured. The contribution from the spectral profile of the reference laser is deconvoluted from the measured spectrum to determine the spectral profile of the 'laser-under-test'. Since the pulses we are interested in characterising are in the mid-infrared with a wavelength around $6.8 \mu\text{m}$, a narrow-bandwidth laser such as a quantum cascade laser (QCL) would be a candidate. However, this only reorients the problem, as one would have to precisely determine the frequency of the reference laser to calibrate the 'laser-under-test'.

To determine the bandwidth of nanosecond pulses using a Fabry-Perot cavity, pulses from the laser-under-test are coupled into the narrow-linewidth cavity. To construct such a cavity, say of 1 MHz linewidth and length $L \sim 10$ cm (and hence Free-Spectral-Range of $c/2L \sim 1.5$ GHz), total optical losses must be limited to 0.4% . This implies the mirrors must have reflectivity $\geq 99.8\%$ at a wavelength of $6.8 \mu\text{m}$. Highly reflective mirrors that are commercially available off-the-shelf in this wavelength range are metallic mirrors with reflectivity between 95% and 98% while being absorptive and hence non-transmissive for the incident light. Substrates that are transmissive for $6.8 \mu\text{m}$, such as ZnSe or CaF_2 , can be coated to obtain high reflectivity. However, such optical components are not readily available off the shelf and are financially demanding.

Thus, by far, the simplest method is to scan over a well-known atomic or molecular transition. This has the advantage of not requiring special optical components, with the choice of atom or molecule and the properties of the transition limiting the precision of the measurement and its technical implementation. In contrast to the other two methods, it allows for characterising both the centre frequency and the bandwidth of the $6.8 \mu\text{m}$ pulses. Thus, as a preliminary test, we choose to characterise the bandwidth of the generated $6.8 \mu\text{m}$ laser pulses with well-known transitions.

This chapter describes the spectroscopy of water (H_2O) molecules of pressure < 1 mbar in a vapour cell with an optical path length of ≈ 30 cm kept at room temperature. Transitions in the ν_2 band between 1471 cm^{-1} and 1474 cm^{-1} are measured and compared with literature values where a consistent offset of 50 MHz in the resonance frequency of is observed. On correcting for known line-broadening effects, the upper-bound on the laser bandwidth is determined to be 80 MHz.

6.1 FREQUENCY CALIBRATION USING KNOWN MOLECULAR TRANSITIONS IN MID-INFRARED REGIME

Molecular spectrum in the MIR

The absorption spectrum is a unique fingerprint of an atom or molecule as it is largely governed by its energy level structure. Apart from that, the measured absorption spectrum of a gas also depends on its temperature and pressure, partial pressure of other gaseous species, natural lifetime of the transition of the initial and final states of the molecule, the presence of external electromagnetic fields, intensity and spectral profile of the incident light field and a number of other factors (Appendix:A).

A proper choice of reference transition and molecular species must be made to calibrate the frequency of the spectroscopy pulses. Fig.6.2 shows the simulated absorption spectrum of molecules that have well-known transitions in the mid-infrared spectrum - ethane (C_2H_6), chloromethane (CH_3Cl), water (H_2O) and ethylene (C_2H_4) taken from the HITRAN database [67]. The simulation is shown for the spectral range between 44.1 THz

and 44.4 THz for the pressure of 1 mbar, temperature 295 K and propagation length of 10 cm. Table 6.1 shows the FWHM linewidth due to Doppler broadening to the absorption spectrum given by

$$\Gamma_D = \frac{1}{c} \sqrt{\frac{8k_B T \log 2}{M}} \approx \frac{540}{\sqrt{M}} \text{ MHz} \quad , \quad (6.1)$$

where T is the temperature of the gas, M the mass of the molecule in atomic units, $k_B = 1.380649 \times 10^{-23} \text{ J K}^{-1}$ the Boltzmann constant and $c=299\,792\,458 \text{ m s}^{-1}$.

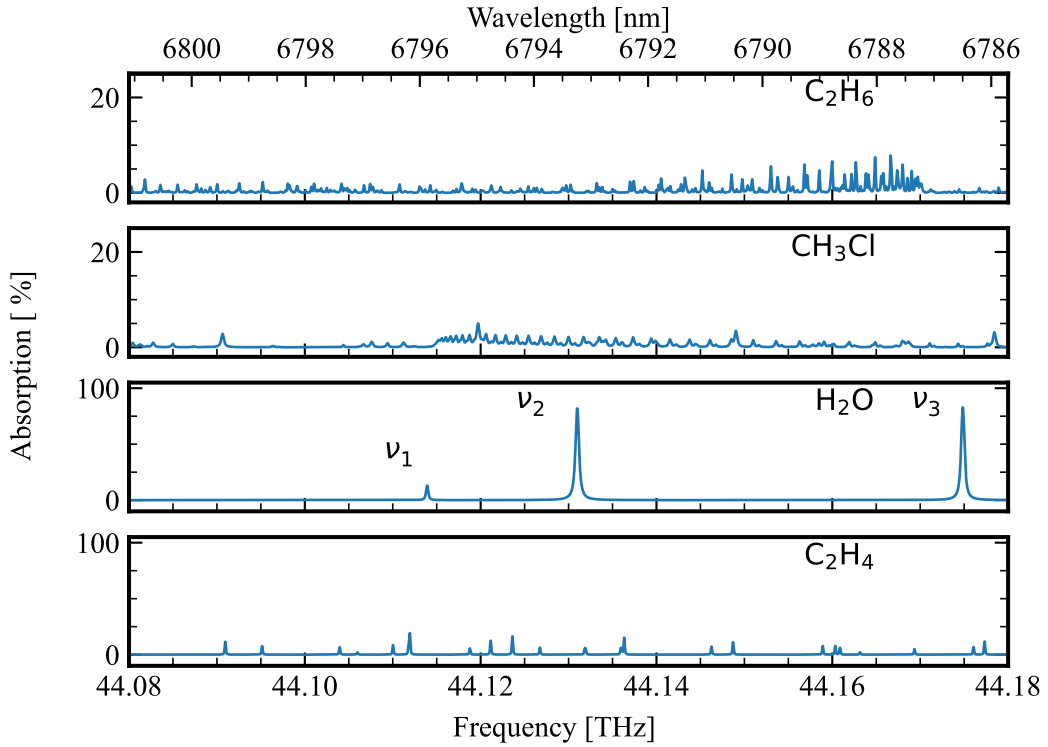


Figure 6.2: Absorption spectra from HITRAN database various gases. We assume a propagation length of 10 cm , 295 K temperature, and 1 mbar pressure .

Molecule	Doppler broadening (FWHM)
CH ₃ Cl	77 MHz
C ₂ H ₄	103 MHz
C ₂ H ₆	99 MHz
H ₂ O	128 MHz

Table 6.1: Doppler linewidths of selected molecules at 295 K. While other molecules have lower Doppler linewidths, H₂O is the most absorptive. (See Fig.6.2)

The simulations show that CH₃Cl, C₂H₄ and C₂H₆ have the largest number of transitions, albeit with weak absorption strengths. To obtain a good signal over background, the absorption spectra in these gases must be measured at much higher pressure or long propagation lengths. High gas pressures can lead to a shift of the resonance frequency of the transition due to pressure. This pressure shift, along with pressure broadening,

can make the analysis more prone to uncontrollable systematics. A multipass absorption cell, such as a Herriot cell, can be used to propagate the spectroscopy pulses repeatedly through the sample gas to increase absorption. The longer propagation length compensates for the low absorption per pass, requiring comparatively low gas pressure. In contrast, H₂O has three strong transitions with resonance frequencies suggested by HITRAN at $\nu_1^{\text{HITRAN}}=44.113\,911$ THz, $\nu_2^{\text{HITRAN}}=44.130\,985$ THz and $\nu_3^{\text{HITRAN}}=44.174\,845$ THz (we omit the digits below 1 MHz as they are below our measurement resolution). These transitions are well-known [68, 69] with the resonance frequencies determined up to 10 kHz. The strength of these resonances makes them easily detectable at 1 mbar for 10 cm propagation length, implying that the spectroscopy in H₂O can be carried out in a simple single-pass vapour cell.

A narrow Doppler broadening increases the relative contribution of the finite laser bandwidth more dominant in the observed spectrum. This makes a heavy molecule such as CH₃Cl a very good candidate. From the Table:6.1, we see that the Doppler broadening in CH₃Cl is lowest due to its higher mass. However, the Doppler broadening in H₂O is only ~ 66% larger than in CH₃Cl.

Thus, our options boil down to multipass absorption spectroscopy in CH₃Cl with a relatively lower Doppler broadening or single-pass absorption spectroscopy in H₂O. We opt to avoid the use of a multipass cell in favour of a simple preliminary measurement. Instead, choose to do a preliminary single-pass absorption spectroscopy in H₂O.

6.2 ABSORPTION SPECTROSCOPY OF H₂O

Preliminary measurement on atmospheric H₂O

Prior to the spectroscopy on H₂O in a low-pressure cell, we assess the performance of the laser system performing spectroscopy in air. We narrow our attention to the first two resonances of interest: $\nu_1^{\text{HITRAN}} \approx 44.11$ THz, $\nu_2^{\text{HITRAN}} \approx 44.13$ THz. The layout of the scheme is shown in Fig: 6.3 -a). The 6.8 μm pulses from the DFG stage are separated from the 3.1 μm and 2.1 μm pulses with a ZnSe separator and a long pass filter. After collimation by a lens of focal length $f_1=250$ mm, the pulses propagate over a distance of 1 m to the energy meter EM1.

The control system for the spectroscopy is implemented as described in Sec:2.3.4 (Fig.2.13). The frequency of 2.1 μm pulses is fixed as the frequency ν_{1979} of 1979 nm-seed laser is set. The frequency of 3.1 μm pulses is tuned by scanning the frequency ν_{15xx} of the 1532 nm-seed laser. This scans the frequency ν_{67xx} of the 6.8 μm pulses from 44.05 THz to 44.15 THz in a step-size of ~20 MHz. These frequencies ν_{1979} and ν_{15xx} are recorded by a wavelength meter for each scan point to determine the frequency ν_{67xx} of the 6.8 μm pulses as $\nu_{67xx} = \nu_{15xx} - \nu_{1979}$ (2.58). The mean energy of 10 pulses of 2.1 μm pulses $E_{2.1}$ and their standard deviation are measured with the energy meter EM2 for each scan point. Similarly, the mean energy of 10 pulses of 6.8 μm measured in EM1 $E_{6.8}$ along with the standard deviation is recorded.

Away from the resonance, the 6.8 μm pulses are not absorbed, and the measured mean energies have their maximum value $E_{6.8}^{\text{max}}$. From these measurements, the transmission at frequency ν is determined as the ratio of the measured mean energy to the off-resonance value, i.e,

$$T(\nu) = \frac{E_{6.8}(\nu)}{E_{6.8}^{\text{max}}} \quad (6.2)$$

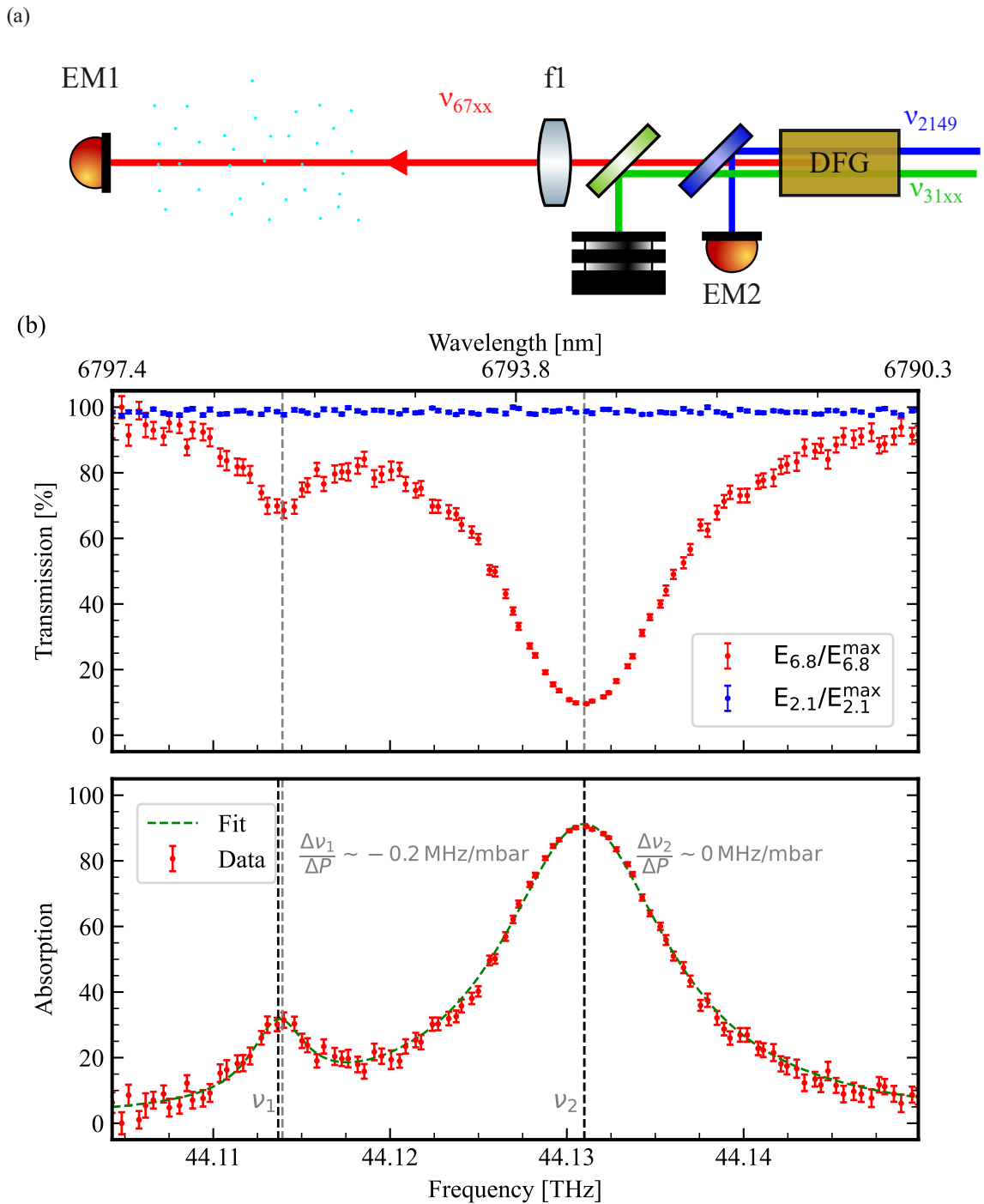


Figure 6.3: (a) Measurement scheme to determine transmission of ν_{67xx} pulses through atmospheric H_2O (b) Transmission spectrum of ν_{67xx} photons by H_2O molecules in the path of propagation of length 1 m in the optical table. The energy of ν_{67xx} pulses is compared to its value away from the resonance of water molecules. Energy measurements of ν_{2149} pulses indicate that scanning the laser frequency does not have an effect on the generated energy of 6.8 μm pulses. The observed energy loss of ν_{67xx} pulses is due to atmospheric absorption.

and the absorption at frequency ν given by

$$A(\nu) = 1 - T(\nu) = 1 - \frac{E_{6.8}(\nu)}{E_{6.8}^{\max}} \quad (6.3)$$

A similar ratio calculated for the 2.1 μm pulse energies conveys the energy stability during the scan. This data is plotted in Fig.6.3-b) as a percentage. From the plot, the energy of 2.1 μm is constant over the entire scan range of >40 GHz. This indicates that the DFG process has a broad bandwidth and hence the energy of 6.8 μm pulses must also not fluctuate. The observed variation in energy of 6.8 μm pulses over the scan range is solely from absorption by H_2O molecules in air. As expected from the reference absorption spectrum of H_2O (Fig.6.2), we observe two broad resonances of H_2O within the scan range. The transitions have broad resonances (with an FWHM of the order of ~ 10 GHz) due to pressure broadening from the air at the atmospheric pressure of $\sim 10^3$ mbar. At $\nu_{67xx} \approx 44.13$ THz, only 20% of the initial energy of 6.8 μm pulses remains. If our spectroscopy scheme were to use only the remaining 20%, a desired signal-to-background ratio would not be obtained using pyroelectric energy meters.

This measurement can be used to estimate the expected pressure-shift of the resonance by comparing the transition frequency at atmospheric pressure to that at zero pressure, obtained from literature values. While the two resonances overlap near $\nu \sim 44.12$ THz, we expect the individual lineshapes to follow a Voigt profile. To account for their overlap, we fit a function equal the sum of two Voigt profiles, $A_{\text{atm}}(\nu) = \alpha_1 V(\nu - \nu_1^{\text{atm}}, \Gamma_1) + \alpha_2 V(\nu - \nu_2^{\text{atm}}, \Gamma_2)$, which has 6 degrees of freedom, to the determined absorption spectrum at atmospheric pressure of ~ 1013.25 mbar. The fit provides a transition frequency of $\nu_1^{\text{atm}} = 44.113\,673(127)$ THz and $\nu_2^{\text{atm}} = 44.130\,988(6)$ THz for the respective transitions. In comparison to the literature values, $\nu_1^{\text{HITRAN}} = 44.113\,911$ THz and $\nu_2^{\text{HITRAN}} = 44.130\,985$ THz, we calculate the pressure shift from zero pressure to atmospheric pressure as

$$\frac{\Delta\nu_i}{\Delta P} = \frac{\nu_i^{\text{atm}} - \nu_i^{\text{HITRAN}}}{1013.25 \text{ mbar}} \quad (6.4)$$

giving $\frac{\Delta\nu_1}{\Delta P} \sim 0.2(1)$ MHz/mbar and $\frac{\Delta\nu_2}{\Delta P} \sim 0$ MHz/mbar. We note that the pressure-shift of resonance is dependent on the interacting molecules in the mixture, and the above estimation is due to the collisions of H_2O molecules with other molecules in the air ($\text{N}_2, \text{O}_2, \text{H}_2\text{O}$, etc.). Nonetheless, from the above estimation and considering literature values [70], for pressures <10 mbar, we expect the pressure-shift to be <1 MHz, i.e, below the resolution of the wavelength meter.

From this measurement on atmospheric H_2O , we learn that for low-pressure single-pass spectroscopy of H_2O in a vapour cell, we require a measurement scheme that reduces the strong atmospheric background, i.e., eliminating the H_2O molecules in the propagation path of the pulse. Additionally, a vapour cell of H_2O must be maintained at the desired pressure, free of background gases, for the duration of the spectroscopy campaign.

Absorption spectroscopy in a H_2O -vapor cell

The layout of the implemented spectroscopy system is displayed in Fig.6.4. The optical setup is covered with a PLA enclosure and constantly flushed with N_2 gas. This eliminates the majority of the atmospheric- H_2O background. As before, pulses of 6.8 μm of energy 300 μJ were separated from the 2.1 μm pump and 3.1 μm signal using a long-pass

filter . The 6.8 μm pulses were split into two parts of equal energy with a 50:50 CaF_2 beam splitter (BSW505, Thorlabs). One part of this pulse goes through the H_2O -absorption cell, and the energy E_T of the transmitted pulses is measured with an energy meter EM1. The remaining part does not enter the vapour cell, and its energy E_{BG} provides a measure of absorption due to residual atmospheric H_2O (present even after flushing with N_2 gas).

The vapor cell has a length of 30 cm and consists of uncoated CaF_2 viewports (VC225, Thorlabs). Each part of the CF window is connected to a DN40 cross piece. One part of the crosspiece is connected to a gas-type independent pressure gauge (CTR101N, Leybold) through a reducer. The final part of the crosspiece is connected to an array of 3 valves with a T-piece. The diaphragm valve V1 and needle valve NV1 are connected to the turbopump (HiCube, Pfeiffer), and the needle valve NV2 is connected to the water reservoir. The water reservoir is essentially a blind flange into which < 1 ml of water is stored before connecting it to the vacuum system.

Initially, the valves V1 and NV1 are kept open when the turbopump is switched on, while NV2 is ensured to be partially open. This removes the air from the spectroscopy cell and the H_2O -reservoir. Once a vacuum of $< 10^{-4}$ mbar is reached, valve V1 is closed. At this point, the air within the system has been pumped out, and the remaining pressure above the reservoir is from saturated H_2O vapour pressure. Since H_2O molecules can now diffuse into the spectroscopy cell through valve NV2 from the reservoir, the pressure in the cell increases. The needle valves NV1 and NV2 are adjusted to attain the required stable pressure within the spectroscopy cell while having continuous flow.

In steady-state, a constant flow of molecules is maintained from the H_2O reservoir to the turbopump. Any impurity, such as molecules such as N_2 , O_2 , etc..., that are commonly present in air is flushed away due to the presence of the continuous flow. The needle valves NV1 and NV2 offer resistance that regulates this flow. The consistent loss of H_2O molecules from the reservoir ($\lesssim 10^{14}$ molecules/s) is negligible compared to population in the reservoir ². Hence, a steady flow of H_2O , free of background gases, with well-controllable pressure, is maintained in the vapour cell for spectroscopy

The same frequency control scheme was used as in the previous measurement (Fig.2.13) to vary the frequency ν_{67xx} over the target range with a step size of ~ 15 MHz. A ~ 5 s of wait-time was provided to ensure proper stabilisation of the laser after the frequency is tuned. At each scan point, the mean energy and standard deviation of 10 pulses of 6.8 μm were measured with energy meters EM1 and EM2. The PDH locking error signal was monitored to ensure that the OPOs or TDO cavity remained stabilised to the injection-seeded light during the scan.

Three transitions of H_2O at $\nu \approx 44.11$ THz, 44.13 THz and 44.17 THz were measured for various pressures. As an example, Fig.6.5 shows the measured raw data for a scan of resonance centred at 44.17 THz at 0.835 mbar pressure, along with statistical uncertainty ³ at each scan point. A frequency-dependent background is visible from measurements of the energy meter EM2. This arises from absorption from H_2O molecules that remain in the propagation path of the pulses even after flushing with N_2 gas. However, the background is significantly reduced, with $>60\%$ of the energy being transmitted, compared to the 10% transmission shown in Fig: 6.3.

² 1 g of H_2O has $\approx 10^{25}$ molecules

³ statistical uncertainty = $\frac{\text{standard deviation}}{\sqrt{\text{No. of measurements}}}$

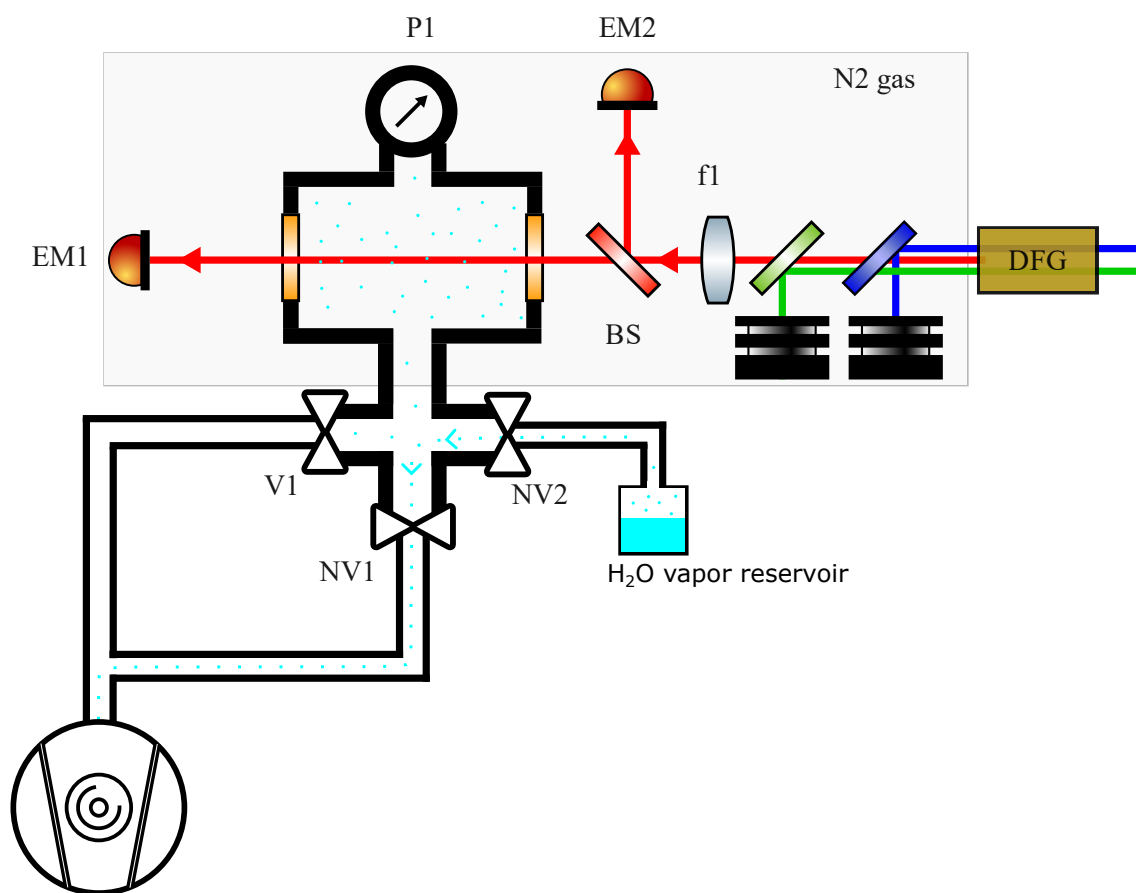


Figure 6.4: Layout of the scheme used for spectroscopy of H₂O

Analysis

One merit of this approach to the spectral characterisation of pulses is the rather straightforward analysis. When pulses of energy E_0 are incident on the beamsplitter, assume that they split in the ratio $b:1-b$, where pulses of energy bE_0 are reflected into the branch with EM2 and is recorded as E_{BG} . Energy meter EM1 measures the fraction of energy $(1-b)E_0$ transmitted through the vapour cell as E_T . The measured energies for frequency ν are given by

$$\begin{aligned} E_T(\nu) &= B_{T,atm}(\nu) (1-b) E_0(\nu) T_{H_2O}(\nu) \\ E_{BG}(\nu) &= B_{BG,atm}(\nu) b E_0(\nu) \end{aligned} \quad (6.5)$$

where $B_{T,atm}(\nu)$ and $B_{BG,atm}(\nu)$ are the additional losses from optical elements and absorption by residual moisture (present even after flushing with N_2) in the beam path leading to EM1 and EM2, respectively. The path length in the atmosphere traversed by the pulses to EM1 is kept equal to that traversed by pulses to EM2 so that $B_{T,atm}(\nu) = B_{BG,atm}(\nu)$. Solving for $T_{H_2O}(\nu)$, we obtain

$$T_{H_2O}(\nu) = \frac{E_T(\nu)}{E_{BG}(\nu)} \frac{b}{1-b} \quad (6.6)$$

When the frequency of laser pulses is away from the resonance of H_2O , the transmission should achieve the maximum value of 1. At this point, the measured energies E_T and E_{BG} are at their maximum possible values. To determine only the transmission of H_2O in the vapour cell, we normalise the determined transmission at ν with the maximum value of transmission, i.e, the value determined when the frequency is off-resonance. This gives absorption at frequency ν of the laser pulses as

$$A_{H_2O}(\nu) = 1 - T_{H_2O}(\nu) = 1 - \frac{E_T(\nu)}{E_{BG}(\nu)} \frac{E_{BG}^{Max}(\nu)}{E_T^{Max}(\nu)} \quad (6.7)$$

Using the above equation, the absorption is calculated for the raw data plotted in Fig.6.5. Typically, atomic and molecular lineshapes have a Voigt profile⁴. Thus, a Voigt function is fitted to the data with standard uncertainties as fitting weights using the Python module LMFIT [71]. We note from [72] that the Voigt function is described by three degrees of freedom - the maximum value or the amplitude, the centre frequency of the resonance ν_{Fit} and the FWHM of the lineshape Γ_V . The standard deviations, determined from the covariance matrix of the fit, are considered the standard uncertainty of the resonance frequency and the FWHM. The systematic uncertainty on the frequency of the resonance is the same as that on the frequency of the $6.8 \mu m$ pulses due to the wavelength meter, i.e., $\sigma_{sys} = 14$ MHz. Fig.6.6 shows the fit along with the residuals. However, the resonance frequency extracted from the fit is 49 MHz more than the resonance frequency expected by HITRAN.

Similar procedure of spectroscopy was carried out for the three resonances of interest (with resonances at $\nu_1^{HITRAN} \approx 44.11$ THz, $\nu_2^{HITRAN} \approx 44.13$ THz and $\nu_3^{HITRAN} \approx 44.17$ THz) at various pressures. In each case, a Voigt function was fitted to the data. The calculated absorption and the fit are shown in 6.7, with the origin of the plot set to the expected resonance frequency from HITRAN. The resonance frequency ν_{Fit} and FWHM (Γ_V) of the Voigt-fit are extracted from the fit. For all the measurements, we observed an offset of \sim

⁴A Voigt lineshape is a convolution of a Gaussian lineshape (from Doppler broadening and laser bandwidth) and a Lorentz lineshape (from pressure broadening). See Appendix: A

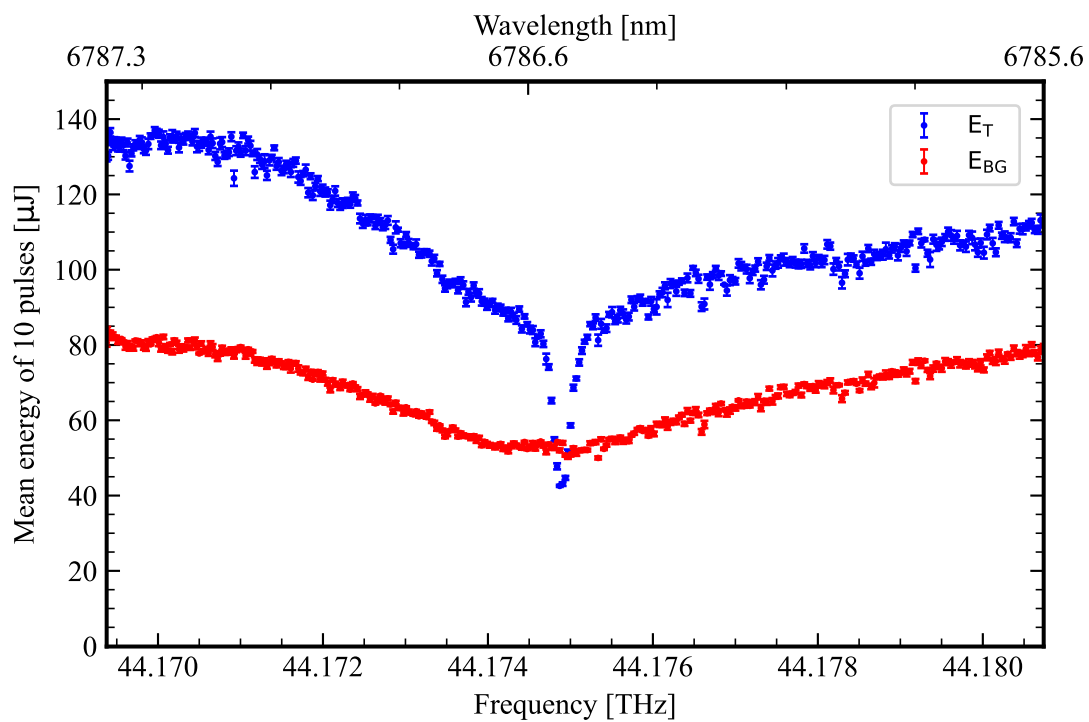


Figure 6.5: Measured energy by EM1 (the transmitted energy E_T) and EM2 (the residual atmospheric background E_{BG}) plotted against the frequency of the laser for transition centred at 44.17 THz and 0.835 mbar of pressure using scheme Fig.6.4. The error bars denote the standard uncertainty σ/\sqrt{n} , where σ is the standard deviation of the n pulses ($n=10$) at each scan point.

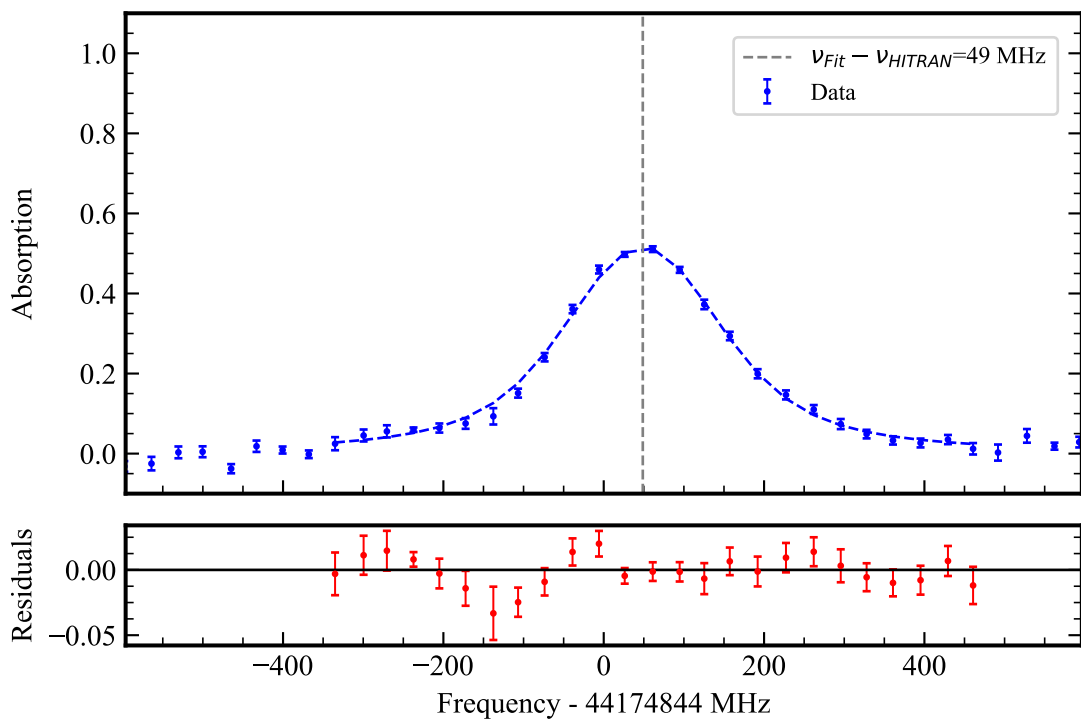


Figure 6.6: Absorption spectrum determined using Eq:6.7 for the data shown in Fig.6.5, compared to simulated absorption from HITRAN for 30 cm propagation length. The origin of the x-axis is set to the reference value set by HITRAN at 44.174 844 THz. The data is fitted against a Voigt profile, and the residuals are shown. The error bars denote the standard uncertainty σ/\sqrt{n} , where σ is the standard deviation of the n pulses ($n=10$) at each scan point.

50 MHz for the determined resonance frequency from the expected resonance frequency from HITRAN. Given that the expected systematic shift should be within $\sigma_{sys}=14$ MHz and this deviation nearly $3.5\sigma_{sys}$, we observe that the calibration of the wavelength meter or other sources of systematic uncertainties (time-dependent background,..) must be considered. The FWHM depends on the difference between frequencies of two points, so it is immune to the systematic uncertainty due to the wavelength meter.

Fig.6.8 shows the variation of the resonance frequency determined by the fit with the pressure in the vapour cell. The average offset of the resonance frequency from the recommended value by HITRAN is also shown. The error bars denote the statistical uncertainty determined by the fit. We recollect here that the analysis of the absorption by atmospheric H₂O indicated that the expected pressure shift for the range of 0.1-10 mbar must be lower than 1 MHz. Thus, instead of fitting a first-order polynomial to the variation of resonance frequency with pressure, we average the determined resonance frequency to obtain the mean resonance frequency ν_i^{mean} for each transition.

The variation of the FWHM of the resonance for different pressures is plotted in Fig.6.9. As expected, reduced absorption and a narrower linewidth are seen at lower pressures for each transition. As suggested from literature [73], at low pressures, a linear relationship of pressure-broadened linewidth Γ_V is to be expected with the vapour pressure:

$$\Gamma_V(p) = \Gamma_{V,p \rightarrow 0} + p \frac{\partial \Gamma_V}{\partial p} \quad (6.8)$$

An appropriate linear fit of the FWHM values to the pressure for each resonance is made to determine the expected linewidth of the transition at zero pressure, i.e, the intercept of the fit $\Gamma_{V,p \rightarrow 0}$. The slope of the transition seems to be sensitive to the resonance frequency. The linewidth at zero pressure is purely due to Doppler broadening Γ_D , the finite bandwidth of the 6.8 μm spectroscopy pulses Γ_L^0 and other systematic effects Γ_O . The linewidth due to Doppler broadening in H₂O at 295 K, $\Gamma_D = 128$ MHz (calculated from Eq.6.1), is expected to be the largest contributor to $\Gamma_{V,p \rightarrow 0}$. Within the scope of this preliminary measurement, other systematic effects, such as power broadening, transit-time broadening, etc... are ignored and will be investigated in later studies. We focus on determining an upper-bound Γ_L for the laser bandwidth. The spectral profile of the 6.8 μm pulses is assumed to be Gaussian so that the upper-bound on the laser bandwidth can be related to the Doppler linewidth by

$$\Gamma_L = \sqrt{\Gamma_{V,p \rightarrow 0}^2 - \Gamma_D^2} \quad (6.9)$$

This way, each transition offers a value for the upper bound of the laser linewidth, collectively giving us an average of 110(19) MHz. The relevant details are presented in Table 6.2.

Conclusion on the laser bandwidth

The temporal profile of intensity of the 6.8 μm pulses was measured Fig.5.14. The Fourier transform calculated from the instantaneous profiles is shown in Fig. 6.10. If the 6.8 μm pulses are transform-limited, then the Fourier transform of the intensity is proportional to the power spectral density (See Eq.2.7). Thus the determined FWHM of this profile of 23 MHz serves as the minimum possible laser bandwidth Γ_L^{FFT} for the measured temporal intensity profile. Deviations from this limit occur due to the variation in the instantaneous frequency of the pulses with time, i.e., the chirp of the pulses. Note that the side-bands at 77 MHz appear due to the round-trip energy loss of the 1030 nm pulses

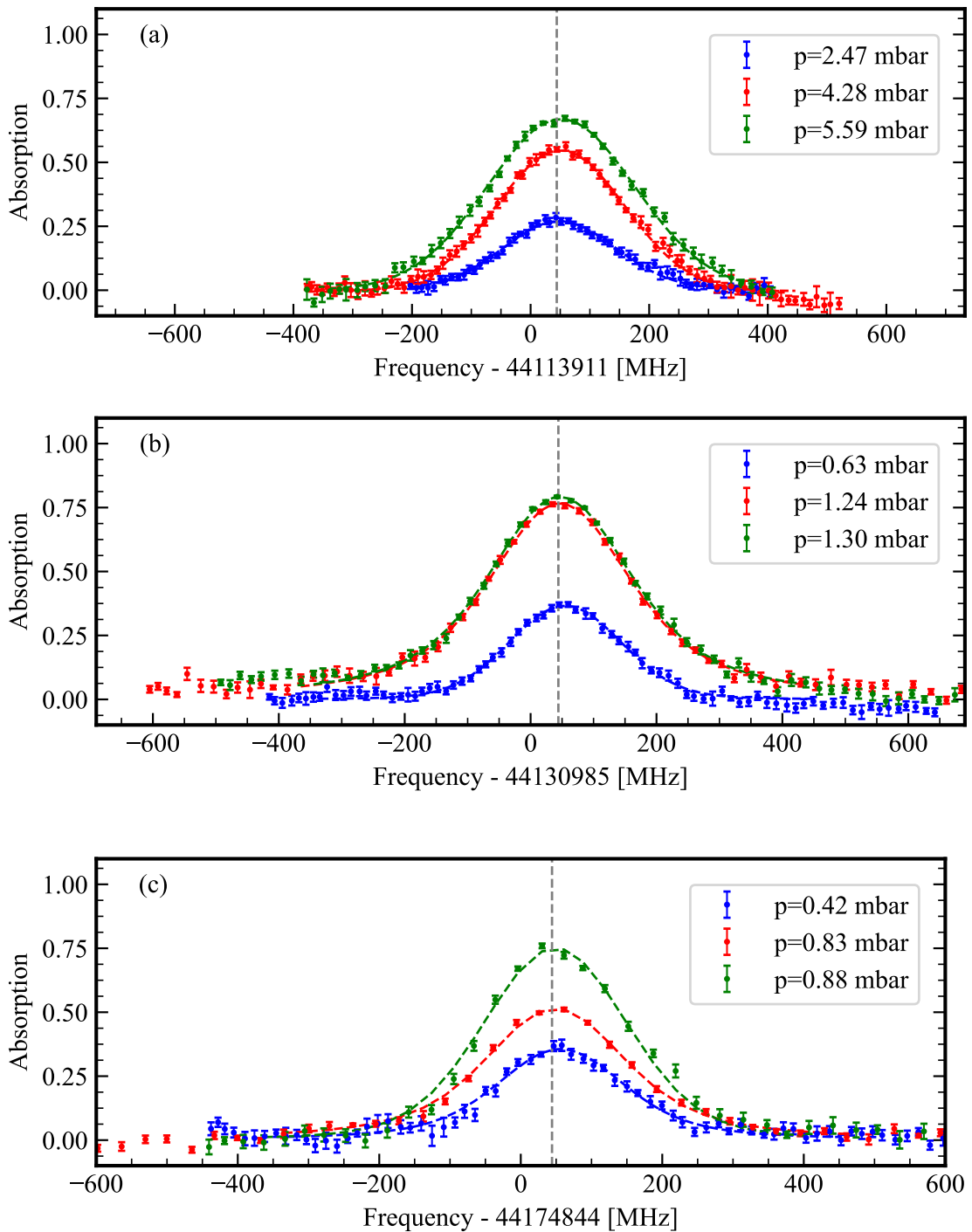


Figure 6.7: Measured absorption profile of H₂O molecules for the 6.8 μm pulses at various pressures for resonances at (a) 44.11 THz (b) 44.13 THz and (c) 44.17 THz. A Voigt function is fitted to the data (dashed line). The resonance frequency and FWHM are extracted from the fit.

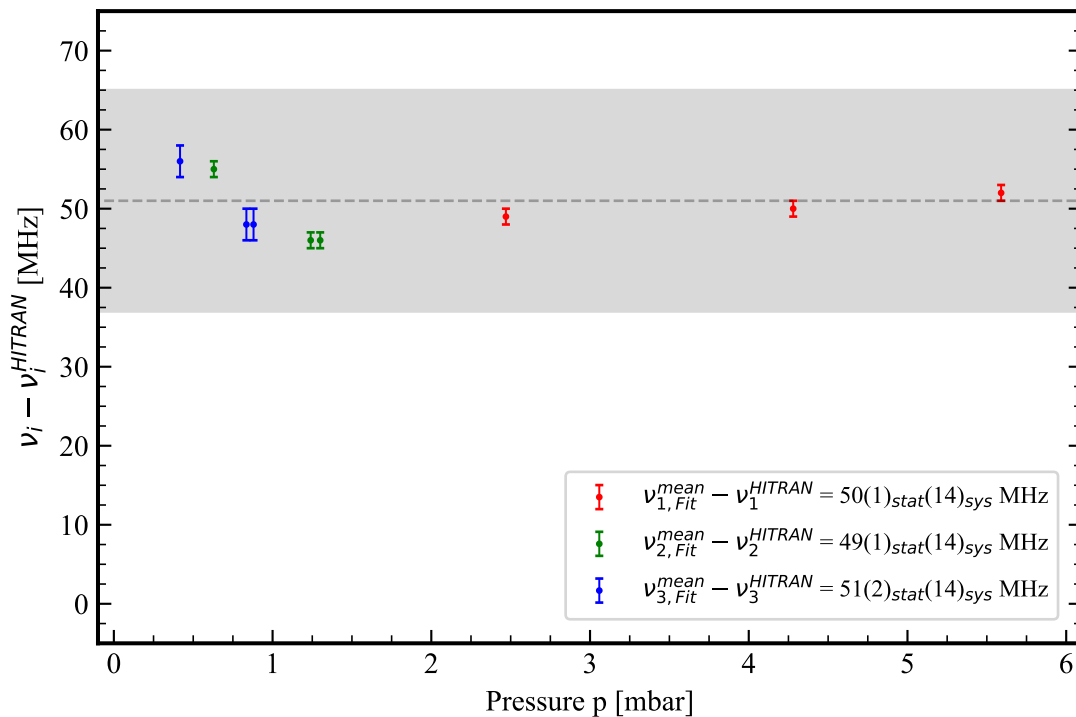


Figure 6.8: Resonance frequencies determined from fit for observed transitions in H_2O at various pressures. The mean of the resonance frequency determined from the fit is compared against the literature value from HITRAN for each of the three studied transitions. Inner error bars depict the statistical uncertainty. Each frequency measurement has a systematic uncertainty of $\sigma_{\text{sys}} = 14$ MHz. The mean deviation of the measured transition frequencies from their respective reference values provided by HITRAN is calculated to be 50 MHz (black line). The grey region depicts the $1\sigma_{\text{sys}}$ about the mean deviation.

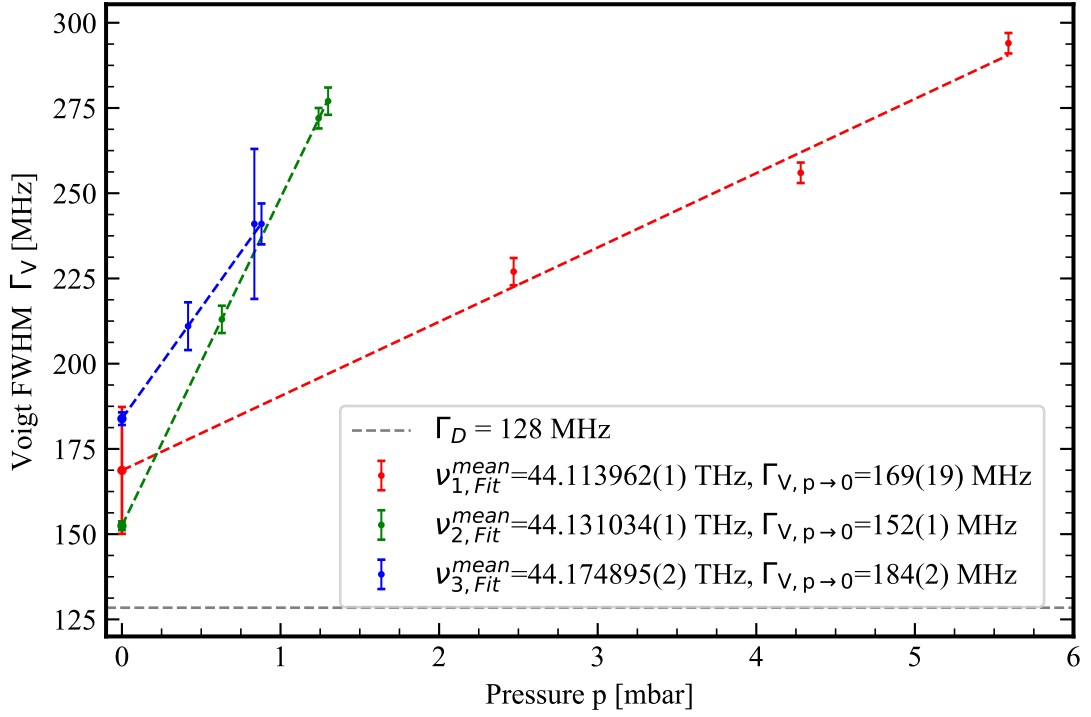


Figure 6.9: FWHM determined from fit to the Voigt function (Fig.6.7) for transitions in H_2O plotted against pressure. A linear fit of the determined FWHM for each transition determines the intercept at zero pressure $\Gamma_{V,p \rightarrow 0}$. FWHM due to Doppler broadening $\Gamma_D = 128$ MHz is plotted for reference.

Index	ν_{HITRAN}	p	ν_{Fit}	Γ_V	$\chi^2_{\text{red,Fit}}$	$\nu_{\text{Fit}}^{\text{mean}}$	$\nu_{\text{Fit}}^{\text{mean}} - \nu_{\text{HITRAN}}$	$\Gamma_{V,p \rightarrow 0}$	Γ_L
i	[THz]	[mbar]	[THz]	[MHz]		[THz]	[MHz]	[MHz]	[MHz]
1	44.113911	2.47	44.113960(1) _{stat}	226(4)	0.55	44.113962(1) _{stat}	50(1) _{stat}	169(19)	115(19)
		4.28	44.113961(1) _{stat}	254(2)	0.67				
		5.59	44.113963(1) _{stat}	293(3)	1.00				
2	44.130985	0.63	44.131040(1) _{stat}	211(3)	0.85	44.131034(1) _{stat}	49(1) _{stat}	152(1)	84(1)
		1.24	44.131031(1) _{stat}	272(3)	1.12				
		1.30	44.131031(1) _{stat}	276(3)	1.64				
3	44.174845	0.417	44.174901(2) _{stat}	216(7)	1.01	44.174895(2) _{stat}	51(2) _{stat}	184(2)	131(2)
		0.835	44.174893(1) _{stat}	239(5)	1.21				
		0.88	44.174893(2) _{stat}	240(7)	3.22				

Table 6.2: Summary of fit results and analysis of spectroscopy of selected transitions in H_2O . As pressure shift is not observed nor expected, the mean of observed transition frequencies is compared with the literature value provided by HITRAN ν_{HITRAN} . The expected Full-Width-at-Half-Maximum at zero pressure for each transition $\Gamma_V|_{p=0}$ is obtained from the Fit 6.9. Assuming a Gaussian spectral profile of the laser, the FWHM of Doppler broadening $\Gamma_D = 128$ MHz is used to determine the upper bound on the FWHM of the laser Γ_L .

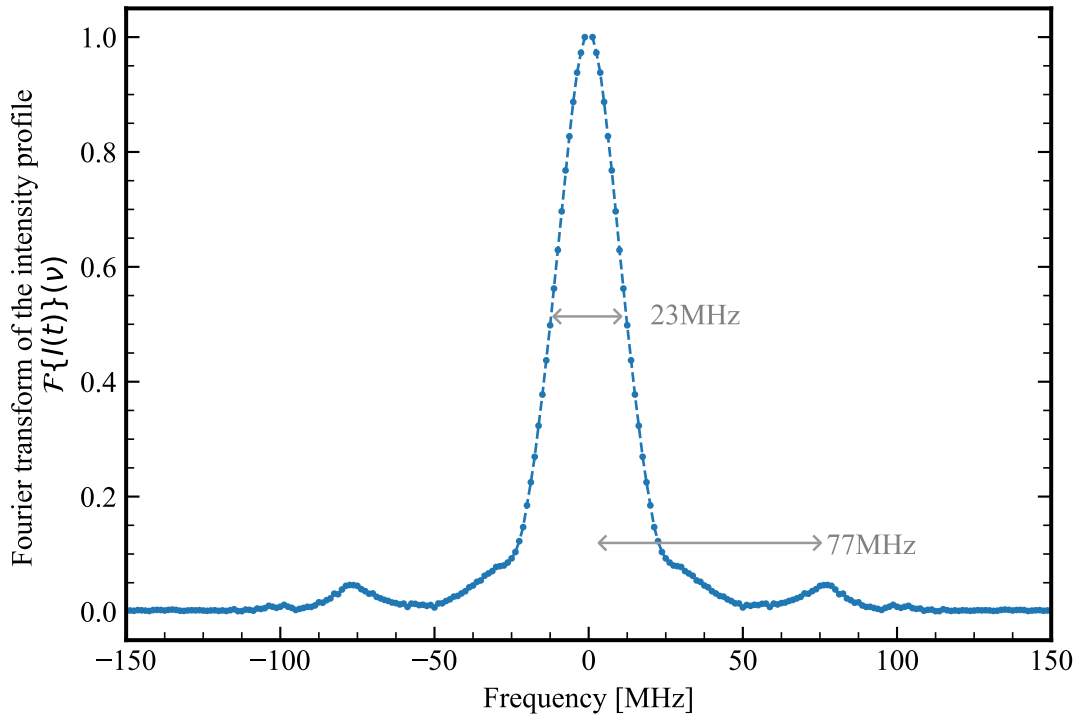


Figure 6.10: Fourier transform of the temporal profile of the measured intensity profile. The FWHM is determined to be 23 MHz. Side-bands at 77 MHz denote the modulation due to roundtrip energy loss within the TDO.

within the TDO cavity during their formation, which appears as a modulation in the temporal profile.

Fig.6.11 compares the estimated upper-bound of the laser bandwidth for each measured transition in H_2O with the FWHM of the Doppler profile and the intercept at zero-pressure $\Gamma_{V,p \rightarrow 0}$. Plotted is also the FWHM of the minimum possible laser bandwidth Γ_L^{FFT} . The difference from the Γ_L^{FFT} to the upper-bound is ~ 86 MHz can be attributed to broadening effects that are not accounted for such as power-broadening or transit-time broadening. Such broadening effects reduce the upper bound, bringing it closer to the target value of 100 MHz of the μH -spectroscopy experiment.

Moreover, the systematic offset of $50(1)_{\text{stat}}(14)_{\text{sys}}$ MHz ($3.5\sigma_{\text{sys}}$) of the determined resonances from the literature value requires further considerations. Primarily, the calibration of the wavelength meter needs to be re-evaluated. The pressure shift of H_2O needs to be studied for the range 0.1-10 mbar as opposed to the current evaluation based on atmospheric pressure measurement. In principle, the asymmetric background (see Fig.6.5) can cause a shift in the frequency as the scanning of the laser system across the resonance was carried out from high-frequency to low-frequency. Thus, this preliminary result is promising, while further study is needed to account for the ignored systematics prior to the spectroscopy in μH .

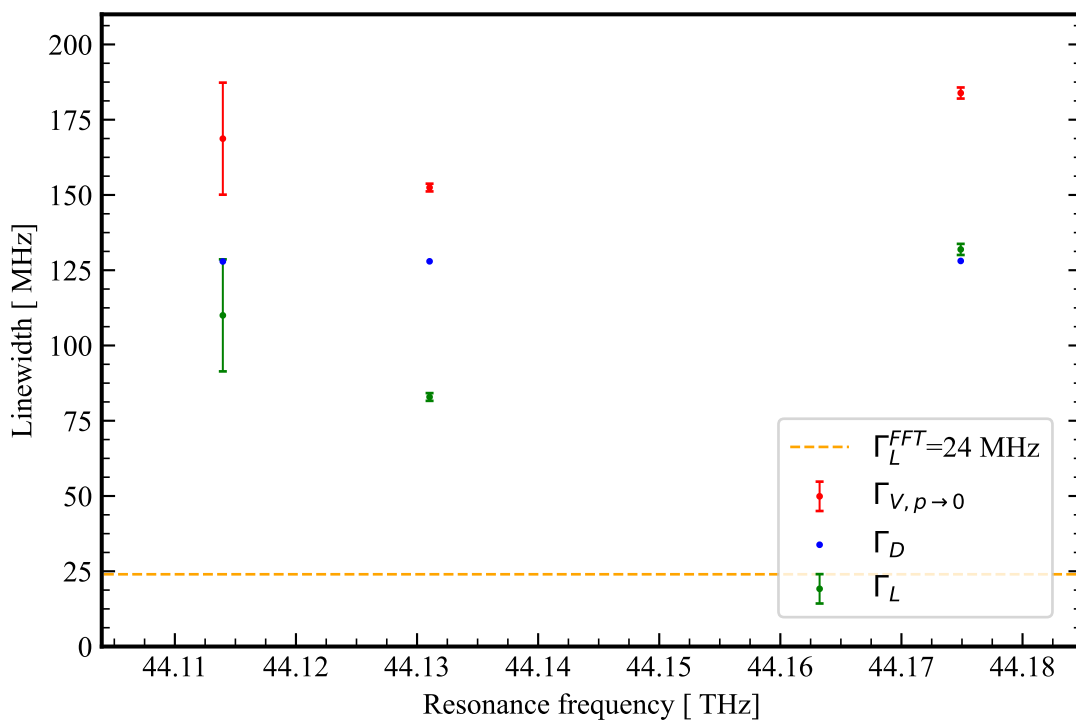


Figure 6.11: Comparison of extracted FWHM of the lineshape $\Gamma_{V,p \rightarrow 0}$ of the transition at zero pressure from the fit to the Voigt, expected FWHM Doppler-broadening Γ_D of H_2O at 295 K and FWHM of the laser spectrum. The yellow line denotes the FWHM of the FFT of the intensity profile of the 6.8 μm pulse (See Fig.6.10).

LINE-BROADENING EFFECTS

Natural linewidth of transitions

Atomic or molecular transitions involve the population transfer from the initial state to the final state of much higher energy. Excited atoms decay exponentially to the state of lower energy, meaning that all states have a finite lifetime. Since an exponential decay in the time domain implies a Lorentz distribution in the frequency domain, the de-excitation probability density function follows a Lorentz distribution, centered around the resonance frequency ν_0 of the transition. In essence, for a transition to an excited state with a natural lifetime τ_N , the energy-time uncertainty relation implies that the transition has a natural line-width given by $\Gamma_N = 1/4\pi\tau_N$ [72], the FWHM of the de-excitation probability density function. For rovibrational transitions, this broadening of lines is very narrow, being of the order of Hz. Thus it is ignored as all the other broadening effects have relatively larger contribution (of order 10^7 Hz).

Consider pulses of energy E_{In} at frequency ν passes through a gas of absorption coefficient $\alpha(\nu)$. Provided there is no saturation of the absorption, the transmitted energy of light at frequency ν is given by

$$E_{Tran}(\nu) = E_{In}(\nu) \sum_i \exp(-\alpha(\sigma_{abs}^i(\nu), L)) \quad , \quad (A.1)$$

where L is the length of the gas column through which the light passes, and i takes values 0,1,2,3... to refer to different transitions of the molecule in the rovibrational band. The contribution of the i^{th} transition to the coefficient of absorption at frequency ν is dependent largely on the absorption cross-section of the transition $\sigma_{abs}^i(\nu)$. The absorption $A(\nu)$ at frequency ν is defined as the relative fraction of absorbed light to the incident light.

$$A(\nu, L) = 1 - \frac{E_{Tran}(\nu)}{E_{In}(\nu, L)} \quad (A.2)$$

Doppler broadening

The molecules in a gas of temperature T are constantly in random motion with a kinetic-energy (or velocity) distribution given by the Boltzmann distribution. Consider a photon incident from \hat{e}_1 on a molecule moving with velocity $\nu \hat{e}_2$. The frequency of light ν seen by the moving molecule is shifted from the frequency ν_0 it sees at rest. This shifts the resonance frequency of the molecule by a factor depending on its velocity ν such that $\nu = \nu_0 + k_B\nu/2\pi \hat{e}_1 \cdot \hat{e}_2$. Effectively, this means that the absorption profile at frequency ν is broadened with the effect of this Doppler-broadening described by the following

Gaussian distribution

$$g_D(\nu) = \frac{c}{2\nu_{mp}\pi^{3/2}} \exp\left(-\frac{(\nu - \nu_0)^2}{\sigma_D^2}\right) \quad (\text{A.3})$$

where $\nu_{mp} = \sqrt{2k_B T/M}$ is the most-probable velocity of molecules, M the mass of molecules, k_B the Boltzmann constant. Note that the standard deviation σ_D and FWHM Γ_D of the above distribution are

$$\sigma_D = \frac{1}{c} \sqrt{\frac{2k_B T}{M}} \quad \text{and} \quad \Gamma_D = 2\sqrt{\log 2} \sigma_D \quad (\text{A.4})$$

, respectively, where c is the speed of light in vacuum. Thus by choosing a molecule of larger mass, one can perform spectroscopy to observe transitions for which the line-width of the transition is smaller due to the lower Doppler line-width $\sigma_D \propto \frac{1}{\sqrt{M}}$ for the same temperature.

Pressure broadening

Another line-broadening effect of interest arises from the collisions between different molecules. As the molecules in a gas collide with each other constantly, the laser-excited molecules can also de-excite by colliding with other molecules, with the excitation energy being converted into the kinetic energy of these molecules. This implies that the excited state decays faster and lives shorter, depending on the rate of molecular collisions. Additionally, when molecular collisions are more frequent, the molecules can absorb incident photons during collisions. The collision of two molecules alters their energy level structure, allowing the absorption of photons of frequency far from their resonance frequency at zero pressure. . As these effects depend on the collisional rate and hence the pressure of the gas, this broadening is called pressure broadening or collisional broadening. The line shape of the resonance is broadened, with the broadening being described by a Lorentz distribution of FWHM Γ_P . Typically, the frequently colliding molecules require different energy than non-interacting molecules to undergo excitation . Thus the resonance frequency of a molecules in a gas of pressure P is also shifted from the resonance frequency of an isolated molecule by δ_P in addition to being broadened [73]. The total effect is then described by

$$g_P(\nu) = \frac{1}{2\pi} \frac{\Gamma_P}{(\nu - \nu_0 - \delta_P)^2 + \frac{\Gamma_P^2}{4}} \quad (\text{A.5})$$

Bandwidth of spectroscopy pulses

In our case, the absorption spectrum is being measured with pulses. Hence the observed line-shape is broader depending on the spectral bandwidth of the pulse. The spectral profile of the 1030 nm pulses from the TDO has been characterized and found to be nearly that of a transform limited Gaussian pulse [43, 55]. As the nonlinear downconversion stage maintains the pulse profile (albeit makes the pulses shorter in the time-domain), the profile of the 6.8 μm spectroscopy pulses is likely to be similar to that of the 1030 nm pulses. Thus a Gaussian spectral profile of standard deviation σ_L (and FWHM $\Gamma_L = 2\sqrt{\log 2}\sigma_L$) with centre frequency ν_{67xx} is assumed to describe the spectroscopy pulses.

$$g_L(\nu) = \frac{1}{\sigma_L \sqrt{2\pi}} \exp\left(-\frac{(\nu - \nu_{67xx})^2}{\sigma_L^2}\right) \quad , \quad (\text{A.6})$$

Total contribution

The combined contribution of these independent effects is given by the convolution of the individual broadening mechanism. The line shape of the absorption spectrum is described by

$$A(\nu) = \int g_D(\nu - \nu') g_P(\nu' - \nu'') g_L(\nu'' - \nu''') d\nu' d\nu'' d\nu''' \quad (\text{A.7})$$

The observed spectral broadening due to the finite bandwidth of the laser and the Doppler broadening also follows a Gaussian profile as the convolution of two Gaussian functions with the same mean is also a Gaussian function, whose standard deviation is given by $\sigma_{L,D}^2 = \sigma_L^2 + \sigma_D^2$ [74]. This effective Gaussian profile convolutes with the Lorentz profile (of FWHM Γ_P) due to pressure broadening to give a Voigt profile. The latter does not have a simple analytic form but has a width that is dependent on the Γ_P and $\sigma_{L,D}$. Since the FWHM of the measured spectrum is dependent on pressure, one can determine $\sigma_{L,D}$ by performing absorption spectroscopy at different pressures and extrapolating to obtain the FWHM at zero-pressure $\Gamma_{V|P=0}$. When other broadening effects are neglected, $\Gamma_{V|P=0} = \sigma_{L,D}$. The Doppler broadening is well understood and easily calculated using Eq:A.4, allowing the bandwidth of the laser pulses can be determined.

REFERENCES

- [1] Helmut Hellwig et al. "Measurement of the Unperturbed Hydrogen Hyperfine Transition Frequency". In: *IEEE Transactions on Instrumentation and Measurement* 19.4 (1970), pp. 200–209.
- [2] Paolo Panci. "21-cm line Anomaly: A brief Status". In: *Nuovo Cim. C* 42.6 (2020), p. 243.
- [3] Michael I. Eides, Howard Grotch, and Valery A. Shelyuto. *Theory of Light Hydrogenic Bound States*. Vol. 222. Berlin: Springer-Verlag, 2007. ISBN: 978-3-540-45269-0, 978-3-540-45270-6.
- [4] Seth H. Neddermeyer and Carl D. Anderson. "Note on the Nature of Cosmic-Ray Particles". In: *Phys. Rev.* 51 (10 May 1937), pp. 884–886.
- [5] G. W. Bennett et al. "Measurement of the Negative Muon Anomalous Magnetic Moment to 0.7 ppm". In: *Phys. Rev. Lett.* 92 (16 Apr. 2004), p. 161802.
- [6] Yoshitaka Kuno and Yasuhiro Okada. "Muon decay and physics beyond the standard model". In: *Rev. Mod. Phys.* 73 (1 Jan. 2001), pp. 151–202.
- [7] D. P. Aguillard et al. "Measurement of the Positive Muon Anomalous Magnetic Moment to 0.20 ppm". In: *Phys. Rev. Lett.* 131 (16 Oct. 2023), p. 161802.
- [8] P. Crivelli. "The Mu-MASS (muonium laser spectroscopy) experiment". In: *Hyperfine Interactions* 239.1 (2018), p. 49. ISSN: 1572-9540.
- [9] Toshiyuki Iwamoto. "LFV: mu-e gamma experiment". In: *Nuclear and Particle Physics Proceedings* 265-266 (2015). Proceedings of the Neutrino Oscillation Workshop, pp. 320–322. ISSN: 2405-6014.
- [10] Niklaus Berger. "The Mu3e Experiment". In: *Nuclear Physics B - Proceedings Supplements* 248-250 (2014). 1st Conference on Charged Lepton Flavor Violation, pp. 35–40. ISSN: 0920-5632.
- [11] Stefano Di Falco and Mu2e Collaboration. "The Mu2e Experiment". In: *Moscow University Physics Bulletin* 77.2 (2022), pp. 108–111. ISSN: 1934-8460.
- [12] Lukas A Schaller and Claude Petitjean. "Muonic atoms and molecules". In: (1993).
- [13] A. Adamczak et al. "Muonic atom spectroscopy with microgram target material". In: *The European Physical Journal A* 59.2 (Feb. 2023), p. 15. ISSN: 1434-601X.
- [14] Randolf Pohl and. "Laser Spectroscopy of Muonic Atoms and Ions". In: *Frontiers in Optics 2015*. Optica Publishing Group, 2015, LTu5G.2.
- [15] Stephen J. Blundell et al. *Muon Spectroscopy: An Introduction*. Oxford University Press, Nov. 2021. ISBN: 9780198858959.
- [16] Dr. Claude Petitjean (eds.) J. Deutsch (auth.) Prof. Lukas A. Schaller. *Muonic Atoms and Molecules*. Monte Verita. Birkhäuser, 1993. ISBN: 9783034872737; 3034872739; 9783034872713; 3034872712.

- [17] David J. Griffiths and Darrell F. Schroeter. *Introduction to quantum mechanics*. Third edition. Cambridge ; New York, NY: Cambridge University Press, 2018. ISBN: 978-1-107-18963-8.
- [18] Peter J. Mohr et al. *Codata Internationally Recommended 2022 Values of the Fundamental Physical Constants*. en. 2024-05-08 04:05:00 2024.
- [19] Aldo Antognini, Franziska Hagelstein, and Vladimir Pascalutsa. “The proton structure in and out of muonic hydrogen”. In: *Ann. Rev. Nucl. Part. Sci.* 72 (2022), p. 389.
- [20] A. C. Zemach. “Proton Structure and the Hyperfine Shift in Hydrogen”. In: *Physical Review* 104.6 (Dec. 1956), pp. 1771–1781.
- [21] Carl E. Carlson, Vahagn Nazaryan, and Keith Griffioen. “Proton-structure corrections to hyperfine splitting in muonic hydrogen”. In: *Phys. Rev. A* 83 (4 Apr. 2011), p. 042509.
- [22] Oleksandr Tomalak. “Two-photon exchange correction to the Lamb shift and hyperfine splitting of S levels”. In: *The European Physical Journal A* 55.5 (2019), p. 64. ISSN: 1434-601X.
- [23] Carl E. Carlson, Vahagn Nazaryan, and Keith Griffioen. “Proton structure corrections to electronic and muonic hydrogen hyperfine splitting”. In: *Phys. Rev. A* 78 (2 Aug. 2008), p. 022517.
- [24] D. Ruth et al. “Proton spin structure and generalized polarizabilities in the strong quantum chromodynamics regime”. In: *Nature Physics* 18.12 (2022), pp. 1441–1446. ISSN: 1745-2481.
- [25] E.V. Cherednikova, R.N. Faustov, and A.P. Martynenko. “Proton polarizability contribution to the hyperfine splitting in muonic hydrogen”. In: *Nuclear Physics A* 703.1 (2002), pp. 365–377. ISSN: 0375-9474.
- [26] K. Abe et al. “Measurements of the proton and deuteron spin structure functions g_1 and g_2 ”. In: *Phys. Rev. D* 58 (11 Oct. 1998), p. 112003.
- [27] K. Abe et al. “Measurement of Leading Particle Effects in Decays of Z^0 Bosons into Light Flavors [Phys. Rev. Lett. 78, 3442 (1997)]”. In: *Phys. Rev. Lett.* 79 (5 Aug. 1997), pp. 959–959.
- [28] P.L. Anthony et al. “Measurement of the proton and deuteron spin structure functions g_2 and asymmetry A_{21} ”. In: *Physics Letters B* 458.4 (1999), pp. 529–535. ISSN: 0370-2693.
- [29] D. Adams et al. “Spin structure of the proton from polarized inclusive deep-inelastic muon-proton scattering”. In: *Phys. Rev. D* 56 (9 Nov. 1997), pp. 5330–5358.
- [30] R. Zielinski. “PhD Thesis”. PhD thesis. University of New Hampshire, 2017.
- [31] Seonho Choi and Jefferson Lab SANE Collaboration. “Spin Asymmetries on Nucleon Experiment at Jefferson Lab”. In: *AIP Conference Proceedings* 1388.1 (Oct. 2011), pp. 480–483. ISSN: 0094-243X.
- [32] X. Zheng and JLab CLAS/EG4 Collaboration. “The EG4 Experiment at Jefferson Lab”. In: *AIP Conference Proceedings* 1155.1 (July 2009), pp. 135–144. ISSN: 0094-243X.
- [33] X. Zheng et al. “Measurement of the proton spin structure at long distances”. In: *Nature Physics* 17.6 (2021), pp. 736–741. ISSN: 1745-2481.
- [34] Franziska Hagelstein, Vadim Lensky, and Vladimir Pascalutsa. “Chiral perturbation theory of the hyperfine splitting in (muonic) hydrogen”. In: *The European Physical Journal C* 83.8 (2023), p. 762. ISSN: 1434-6052.

- [35] J. J. Kelly. "Simple parametrization of nucleon form factors". In: *Phys. Rev. C* 70 (6 Dec. 2004), p. 068202.
- [36] Michael O. Distler, Jan C. Bernauer, and Thomas Walcher. "The RMS charge radius of the proton and Zemach moments". In: *Physics Letters B* 696.4 (2011), pp. 343–347. ISSN: 0370-2693.
- [37] John Arrington and Ingo Sick. "Precise determination of low-Q nucleon electromagnetic form factors and their impact on parity-violating e-p elastic scattering". In: *Phys. Rev. C* 76 (3 Sept. 2007), p. 035201.
- [38] Marc Vanderhaeghen and Thomas Walcher. "Long Range Structure of the Nucleon". In: *Nuclear Physics News* 21.1 (2011), pp. 14–22.
- [39] J. C. Bernauer et al. "High-Precision Determination of the Electric and Magnetic Form Factors of the Proton". In: *Phys. Rev. Lett.* 105 (24 Dec. 2010), p. 242001.
- [40] Dalibor Djukanovic et al. "Zemach and Friar radii of the proton and neutron from lattice QCD". In: *Phys. Rev. D* 110 (1 July 2024), p. L011503.
- [41] Yong-Hui Lin, Hans-Werner Hammer, and Ulf-G. Meißner. "New Insights into the Nucleon's Electromagnetic Structure". In: *Phys. Rev. Lett.* 128 (5 Feb. 2022), p. 052002.
- [42] Jonas Nuber et al. "Diffusion of muonic hydrogen in hydrogen gas and the measurement of the 1s hyperfine splitting of muonic hydrogen". In: *SciPost Phys. Core* 6 (2023), p. 057.
- [43] Manuel Zeyen. "The Thin-Disk Laser System for the Measurement of the Ground-State Hyperfine Splitting in Muonic Hydrogen". en. Doctoral Thesis. Zurich: SNF and SNF, 2021.
- [44] Mirosław Marszałek. "Multipass Cell for Laser Spectroscopy of Muonic Hydrogen". PhD thesis. Jan. 2022.
- [45] Laura Paulina Sinkunaite. "Detection System for Measuring the Hyperfine Splitting in Muonic Hydrogen". en. Doctoral Thesis. Zurich: ETH Zurich, 2022.
- [46] P. Amaro et al. "Laser excitation of the 1s-hyperfine transition in muonic hydrogen". In: *SciPost Phys.* 13 (2022), p. 020.
- [47] R. Pohl, A. Antognini, F. Nez, et al. "The size of the proton". In: *Nature* 466 (2010), pp. 213–216.
- [48] W. Sellmeier. "Ueber die durch die Aetherschwingungen erregten Mitschwingungen der Koerpertheilchen und deren Rueckwirkung auf die ersteren, besonders zur Erklaerung der Dispersion und ihrer Anomalien". In: *Annalen der Physik* 223.12 (1872), pp. 525–554.
- [49] W. Brunner and H. Paul. "I Theory of Optical Parametric Amplification and Oscillation". In: ed. by E. Wolf. Vol. 15. *Progress in Optics*. Elsevier, 1977, pp. 1–75.
- [50] Robert W Boyd. *Nonlinear Optics*. Fourth edition. Academic Press, 2020. ISBN: 0128110023; 9780128110027.
- [51] Richard L. Sutherland. *Handbook of Nonlinear Optics*. 2nd ed., rev. and expanded. Optical engineering 82. Marcel Dekker, 2003. ISBN: 9780824742430; 0824742435; 9780824748593; 082474859X.
- [52] Valentin Petrov. "Frequency down-conversion of solid-state laser sources to the mid-infrared spectral range using non-oxide nonlinear crystals". In: *Progress in Quantum Electronics* 42 (2015), pp. 1–106. ISSN: 0079-6727.

- [53] Peter G. Schunemann et al. "Advances in nonlinear optical crystals for mid-infrared coherent sources". In: *J. Opt. Soc. Am. B* 33.11 (Nov. 2016), pp. D36–D43.
- [54] Ahmed Ouf. "The Down-Conversion System for the Muonic Hydrogen Hyperfine Splitting Experiment at PSI". PhD thesis. Johannes Gutenberg University Mainz, 2025.
- [55] Manuel Zeyen et al. "Injection-seeded high-power Yb:YAG thin-disk laser stabilized by the Pound-Drever-Hall method". In: *Opt. Express* 31.18 (Aug. 2023), pp. 29558–29572.
- [56] Eric D. Black. "An introduction to Pound–Drever–Hall laser frequency stabilization". In: *American Journal of Physics* 69.1 (Jan. 2001), pp. 79–87. ISSN: 0002-9505.
- [57] Manuel Zeyen et al. "Injection-seeded high-power Yb:YAG thin-disk laser stabilized by the Pound-Drever-Hall method". In: *Opt. Express* 31.18 (Aug. 2023), pp. 29558–29572.
- [58] Manuel Zeyen et al. "Compact 20-pass thin-disk multipass amplifier stable against thermal lensing effects and delivering 330 mJ pulses with M2 ≤ 1.17". In: *Opt. Express* 32.2 (Jan. 2024), pp. 1218–1230.
- [59] Eugene Hecht. *Optics, Global Edition*. 5ed. Pearson Higher Education, 2017. ISBN: 9781292096933; 1292096934.
- [60] R. W. P. Drever et al. "Laser phase and frequency stabilization using an optical resonator". In: *Applied Physics B* 31.2 (June 1983), pp. 97–105. ISSN: 1432-0649.
- [61] International Organization for Standardization. *ISO 80000-3:2022 — Quantities and units — Part 3: Space and time*. <https://www.iso.org/standard/77769.html>. 2022.
- [62] Hai Wang et al. "ZnGeP₂ optical parametric oscillator with wide temperature tuning". In: *Optics Communications* 542 (2023), p. 129584. ISSN: 0030-4018.
- [63] Rüdiger Paschotta. *Field Guide to Laser Pulse Generation*. SPIE, 2008.
- [64] Michale S. Fee, K. Danzmann, and Steven Chu. "Optical heterodyne measurement of pulsed lasers: Toward high-precision pulsed spectroscopy". In: *Phys. Rev. A* 45 (7 Apr. 1992), pp. 4911–4924.
- [65] Xuanning Hun et al. "Fabry–Pérot based short pulsed laser linewidth measurement with enhanced spectral resolution". In: *Results in Physics* 37 (2022), p. 105510. ISSN: 2211-3797.
- [66] Jae Wan Kim et al. "Measurement of the linewidth of a continuous-wave laser with a cavity-length modulation technique". In: *Appl. Opt.* 38.9 (Mar. 1999), pp. 1742–1745.
- [67] I.E. Gordon et al. "The HITRAN2020 molecular spectroscopic database". In: *Journal of Quantitative Spectroscopy and Radiative Transfer* 277 (2022), p. 107949. ISSN: 0022-4073.
- [68] Robert A. Toth. " ν_2 band of H₂16O: line strengths and transition frequencies". In: *J. Opt. Soc. Am. B* 8.11 (Nov. 1991), pp. 2236–2255.
- [69] Peter F. Bernath. "The spectroscopy of water vapour: Experiment, theory and applications". In: *Phys. Chem. Chem. Phys.* 4 (9 2002), pp. 1501–1509.
- [70] Jens Bosenberg. "Measurements of the pressure shift of water vapor absorption lines by simultaneous photoacoustic spectroscopy". In: *Appl. Opt.* 24.21 (Nov. 1985), pp. 3531–3534.

- [71] M. Newville et al. *LMFIT: Non-Linear Least-Square Minimization and Curve-Fitting for Python (0.8.0)*. 2014.
- [72] Christopher J Foot. *Atomic physics*. Oxford master series in atomic, optical, and laser physics. Oxford: Oxford University Press, 2007.
- [73] G. Peach and. "Theory of the pressure broadening and shift of spectral lines". In: *Advances in Physics* 30.3 (1981), pp. 367–474.
- [74] Paul Bromiley. "Products and convolutions of Gaussian probability density functions". In: *Tina-Vision Memo* 3.4 (2003), p. 1.

SIDDHARTH RAJAMOCHANAN

Nationality : Indian

PhD Student, AG Pohl , Staudingerweg 7,55128

Mainz, Germany

srajamoh@uni-mainz.de

sid.siddharthr@gmail.com

+49-15737828750



Research Interests

Atomic, Molecular and Optical Physics, Precision laser spectroscopy, Muon Physics, Nonlinear optics, Low-energy tests of the Standard model

Education

☐ January 2021 – Present

PhD student, JGU Mainz, Germany

☐ July 2015 – 2020

BS-MS Physics, University of Hyderabad, Hyderabad, India

☐ **Deutsche A2 Goethe Zertifikat** (2024)

☐ **IELTS Academic** (2019) **Score 8.0/9.0**

☐ **Graduate Record Examination Physics** (2019) **Score 820/990**

Experience

☐ 2023 - Present

Visiting researcher at Paul Scherrer Institute, Switzerland

2021 - Present

Employee/PhD student at AG Pohl, Johannes Gutenberg-Universität Mainz, Germany

Project: Laser system for Muonic Hydrogen spectroscopy

- Designed and implemented a down-conversion scheme for high-energy NIR laser pulses into the MIR for spectroscopy of 1S hyperfine splitting in muonic hydrogen
- Implemented absorption spectroscopy for wavelength calibration of MIR pulses
- Teaching assistant for 3 semesters in experimental physics courses

☐ 2016 - 2020

Project student at the University of Hyderabad, India

Project: A Lagrangian and Hamiltonian Description of Thermodynamics

- Focused on variational principle formulation for thermodynamics
- Research focused on black hole thermodynamics

☐ May 2019 - July 2019

Intern at Indian Institute of Technology Bombay, Mumbai, India

Project: A Review of Left-Right Symmetric Model and Neutrinos

- Reviewed contemporary gauge theory models for electroweak interactions, focusing on $SU(2)_L \times SU(2)_R$ model
- Reviewed neutrino oscillations and experiments on the fermionic nature of the neutrino

☐ May 2018 - July 2018

Intern at Saha Institute of Nuclear Physics, India

Project: A Review of the Principles of General Theory of Relativity

- Reviewed general relativity
- Focused study on gravitational lensing and black holes

☐ May 2017 - July 2017

Intern at Indian Institute of Technology Kanpur, India

Project: General Treatment of Reflection of Spherical Waves from Spherical Surface for ANITA Experiment

- Developed formalism for reflection of spherical electromagnetic waves from a spherical surface
- Work related to the ANITA Experiment to detect atmospheric neutrinos by measuring electromagnetic radiation produced through weak interaction cascades

Skills

- ☐ Proficient in C++, Python, Matlab, COMSOL
 - ☐ CAD Design and 3d-printing
 - ☐ Nonlinear optical simulations with SNLO
-

Accolades

- ❑ Recipient of Smt. Rani Dev & Sri. Chandra Sen Pathak Memorial Medal (2020)
 - ❑ Recipient of INSPIRE-Scholarship for Higher Education (2015)
-

Publications

- ❑ *Compact 20-pass thin-disk multipass amplifier stable against thermal lensing effects and delivering 330 mJ pulses with $M^2 < 1.17$* , Manuel Zeyen, Lukas Affolter, Marwan Abdou Ahmed, ... Aldo Antognini, Opt. Express 32, 1218-1230 (2024)
 - ❑ *Diffusion of muonic hydrogen in hydrogen gas and the measurement of the 1s hyperfine splitting of muonic hydrogen*, J. Nuber, A. Adamczak, M. Abdou Ahmed, ... J. Zhang, SciPost Phys. Core 6, 057 (2023)
 - ❑ *Injection-seeded high-power Yb: YAG thin-disk laser stabilized by the Pound-Drever-Hall method*, Manuel Zeyen, Lukas Affolter, Marwan Abdou Ahmed,... Aldo Antognini, Opt. Express 31, 29558-29572 (2023)
 - ❑ *Pound-Drever-Hall locking scheme free from Trojan operating points*, Manuel Zeyen, Lukas Affolter, Marwan Abdou Ahmed, ... Karsten Schuhmann, Rev. Sci. Instrum. (2023); 94 (1): 013001.
 - ❑ *Laser excitation of the 1s-hyperfine transition in muonic hydrogen*, P. Amaro, A. Adamczak, M. Abdou Ahmed, ... A. Antognini, SciPost Phys. 13, 020 (2022)
-

Highlighted presentations in Conferences

- ❑ Talk at DPG Sektion Atome, Moleküle, Quantenoptik und Photonik (SAMOP23), Hannover (2023)
 - ❑ Poster at Proton Radius European Network" (PREN 2023) and the "Muonic Atom Spectroscopy Theory Initiative" (μ ASTI) (2023)
 - ❑ Talk at DPG Sektion Atome, Moleküle, Quantenoptik und Photonik (SAMOP21), Virtual Meeting, (2021)
-